TÉCNICO
LISBOA

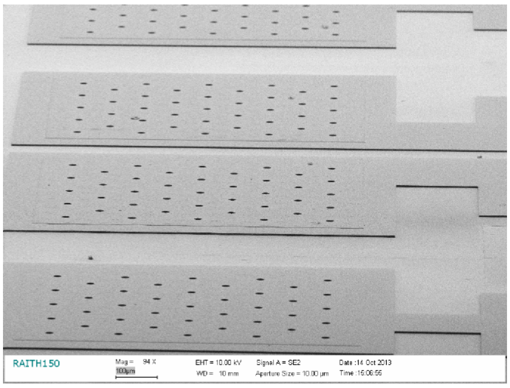

MicroElectroMechanical Systems (MEMS) for applications in acoustics

Rui Manuel Ferreira Sampaio

Thesis to obtain the Master of Science Degree in

Bioengineering and Nanosystems

Examination Committee

Chairperson: Prof. Dr. Luis Joaquim Pina da Fonseca
Supervisor: Prof. Dr. João Pedro Estrela Rodrigues Conde
Member of the Committee: Prof^{a} Dr^{a} Susana Isabel Pinheiro Cardoso de Freitas
Prof. Dr. Marcelino Bicho dos Santos

December 2013

To my parents...

This page was intentionally left blank.

Acknowledgments

First and foremost I'll like to acknowledge my advisor Prof. João Pedro Conde for all its support and trust deposited in me. His overall optimism, enthusiasm and sheer confidante were a great motivational factor, specially during times of increasing frustration. I'm certainly pleased for this partnership and hope that we may keep exchanging ideas on new and exciting projects for many years to come. Also, to Dr. Virginia Chu, for being a force for progress at INESC-MN, always ready with a solution and the will to see it through.

A special acknowledge goes to João Mouro for all his patience and availability for the amorphous silicon depositions, for all his help during the fabrication and experimental characterization and several fruitful discussions on MEMS, Physics and Chess. To Alexandra Gualdino for her initial help in the project and many discussions and helpful suggestions in the fabrication process. Finally to Pedro Sousa which accompanied me in the beginning and lend a big help in the optimization of the quasi-DC setup.

I acknowledge Dr. João Gaspar and his collaborators at INL for their availability and help in the fabrication process without whom it wouldn't be possible. Also, to Prof. Marcelino Santos, Tiago Domingues and Bruno Santos for their on-going interest and general discussions on the project.

To Prof. Susana Freitas and Dr. Diana Leitão for their help and availability on the use of the Nordiko equipment without which the fabrication process would have forcibly stopped.

Also, I'll like to acknowledge all the staff at INESC-MN for their support and assistance during the fabrication.

To my colleagues at INESC-MN and from class for all the good moments, lunches, dinners, coffee or random encounters in the corridors, making the laboratory drama and insane quest for results a little bit more enjoyable.

And, of course, I acknowledge my parents for their unconditional support during all these years.

Resumo

Sistemas microelectromecânicos (MEMS) estão no centro de muitas tecnologias de sucesso e recentemente começaram a dominar o mercado de pequenos microfones para aplicações em dispositivos móveis devido à sua performance superior face aos microfones de condensador comuns. É esperado que tal sucesso se traduza para altifalantes MEMS.
O objetivo deste trabalho foi apresentar um novo processo de microfabricação baseado em silício amorfo depositado por PECVD para um altifalante de ultra-baixo consumo atuado electrostaticamente juntamente com uma descrição teórica geral e uma caracterização experimental inicial. Baixas voltagens, grandes áreas e ultra-baixo consumo são características de relevo para o desenvolvimento de um produto competitivo. Este trabalho é desenvolvido em colaboração com o INESC-ID / Silicon Gate.
A primeira abordagem passou pela extensão do processo para pontes MEMS usado no INESC-MN. A simplicidade do processo, baixas temperaturas de processamentos e grande flexibilidade de substratos são importantes características a destacar. Contudo, as geometrias permitidas não são compatíveis com um altifalante e um processo de segunda geração foi desenvolvido em consequência. A simplicidade do processo é perdida mas importantes aspetos como baixas temperaturas de processamento, compatibilidade com dies CMOS e uso de materiais típicos em processamento MEMS são mantidas.
Um protótipo do segundo processo é apresentado. Dados experimentais sobre frequências de ressonância e deflecção absoluta no espectro audível são apresentados para estruturas adaptadas do primeiro processo. Finalmente é feita uma discussão geral estabelecendo linhas de guia para o desenho e futuro desenvolvimento destes dispositivos.

Palavras-chave: MEMS, Electroestático, Altifalante, Silício amorfo, PECVD

Abstract

Microelectromechanical systems (MEMS) are in the centre of very successful technologies and recently started dominating the market of small microphones for mobile application due to their superior performance over their electret counterpart. Such success is also expected for MEMS loudspeakers.

The aim of this work was to present a new fabrication process based on PECVD amorphous silicon for ultra-low power electrostatic MEM loudspeakers together with a general theoretical description and initial experimental characterization. Low actuation voltages, large actuation area and ultra-low power consumption are compelling attributes for the development of a market competitive product. This work is developed in collaboration with INESC-ID / Silicon Gate.

The first approach was carried by extending the well-developed process for thin bridges and cantilevers at INESC-MN. Its simplicity, low temperatures and wide flexibility in the choice of substrates are strong features of this process. Unfortunately the geometries allowed proved to be incompatible for a loudspeaker application leading to the development of a second generation process. The simplicity of the process is lost but important aspects such as low temperature, CMOS compatibility and the use of typical materials in MEMS processing are retained.

A working prototype for the second generation is presented and the first generation process is revisited for a first study on the mechanical properties of the structures. Resonance frequency measurements in a pressure controlled environment are provided together with absolute deflection measurements in the audible-rage. Finally a general discussion is provided setting design rules for further development.

Keywords: MEMS, Electrostatic, Loudspeaker, Amorphous Silicon, PECVD

This page was intentionally left blank.

Contents

Acknowledgments . . . v

Resumo . . . vii

Abstract . . . ix

List of Tables . . . xv

List of Figures . . . xvii

List of Abbreviations . . . xxi

1 Introduction 1

1.1 State-of-the-art . . . 1

1.1.1 MEMS Microphones . . . 1

1.1.2 MEMS Loudspeakers . . . 3

1.2 Motivation . . . 7

1.3 Thesis outline . . . 7

2 Microfabrication 9

2.1 Basic principles and concepts . . . 9

2.1.1 Layers . . . 9

2.1.2 Deposition and Etching techniques . . . 10

2.1.3 Basic MEMS processing . . . 12

2.2 The loudspeaker . . . 13

2.2.1 First generation . . . 14

2.2.2 Second generation . . . 16

3 Theoretical description 27

3.1 Thin Beams . . . 27

3.1.1 Governing equation . . . 30

3.1.2 Natural frequencies and mode shapes . . . 31

3.1.3 Static load . . . 34

3.1.4 Harmonic driving . . . 34

3.2 Thin Rectangular Plates . . . 36

3.2.1 Governing equation . . . 38

3.2.2 Natural frequencies and mode shapes . . . 39

3.2.3 Harmonic driving . . . 41
3.2.4 Static loading . . . 42
3.3 Thin Circular plates . . . 42
3.3.1 Governing equation . . . 43
3.3.2 Natural frequencies and mode shapes . . . 43
3.3.3 Harmonic driving . . . 45
3.3.4 Uniform static loading . . . 45
3.4 The One-Degree-of-Freedom approximation . . . 45
3.4.1 The equation of motion . . . 46
3.4.2 Solution to the equation of motion . . . 51
3.5 Conclusion . . . 53

4 Experimental Characterization 57
4.1 Quasi-DC and audible range setup . . . 57
4.1.1 Introduction . . . 57
4.1.2 Absolute deflection characterizations . . . 58
4.2 High frequency detection setup . . . 59
4.2.1 Introduction . . . 59
4.2.2 Resonance frequencies characterization . . . 60
4.3 Conclusion . . . 64

5 Discussion 65
5.1 First generation vs Second generation . . . 65
5.2 Design considerations . . . 66
5.2.1 Membrane dimensions . . . 66
5.2.2 Pull-in Voltage, Air gap height and Bias Voltage . . . 69
5.2.3 Perforation cell density . . . 72
5.3 Squeeze-film damping . . . 74
5.4 Circuit analogy . . . 76
5.5 Conclusion . . . 77

6 Conclusions 79
6.1 Achievements . . . 79
6.2 Future Work . . . 79

A Runsheet example 81

B Extended Hamiltonian principle 91
B.1 Governing equation for a two dimensional system with one dependent variable . . . 91

C Deformation of linear isotropic elastic solids 93
C.1 Introduction . . . 93

D Thin plates **97**
D.1 Coefficient appearing in equation (3.78) 97

Bibliography **104**

List of Tables

1.1 Summary of MEMS loudspeakers presented in the literature 6

2.1 Amorphous silicon deposition conditions 23

3.1 Summary of the governing equation, boundary conditions, characteristic equation, natural frequencies and mode shapes for a clamped-clamped thin beam. All equation are presented in their non-dimensional form. 53

3.2 General boundary conditions for a thin rectangular plate. These conditions assume the following boundary attachments — at $x = 0$ there is a translational spring $k_{xL}[\mathrm{N/m}]$, and a torsion spring $k_{txL}[\mathrm{N.m/rad}]$; at $x = a$ there is a translational spring k_{xR}, and a torsion spring k_{txR}; at $y = 0$ there is a translational spring k_{yL}, and a torsion spring k_{tyL}; at $y = b$ there is a translational spring k_{yR}, and a torsion spring k_{tyR}. 54

3.3 General boundary conditions for a thin solid circular plate. These conditions assume the following boundary attachments — at $r = a$ there is a translational spring $k_a[\mathrm{N/m}]$, and a torsion spring $k_{ta}[\mathrm{N.m/rad}]$. At $r = 0$ the conditions of finite displacement is used. 54

3.4 General boundary conditions for a thin rectangular plate. These conditions assume the following boundary attachments — at $x = 0$ there is a mass $M_L[\mathrm{Kg}]$ with rotational inertia $J_L[\mathrm{kg.m^2}]$, a translation spring with elastic constant $k_L[\mathrm{N/m}]$ and a torsion spring $k_{tL}[N.m/rad]$; at $x = L$, there is a mass M_R with rotational inertia J_R, a translation spring with elastic constant k_R and a torsion spring k_{tR}. 55

3.5 Resonance frequency, elastic constant and effective mass for the square and circular membranes and for the suspended square without axial stress. For circular membranes, R is the radius of the membrane. 55

3.6 Summary of the governing equation, boundary conditions, characteristic equation, natural frequencies and mode shapes for a clamped thin square and circular plate. All equation are presented in their non-dimensional form. 56

This page was intentionally left blank.

List of Figures

1.1 Two examples of current implementations of a MEMS microphones — (a) Knowles S2.14 MEMS die cross section. (from chipworks) and (b) SEM micrograph of the microphone diaphragm of Akustica's AKU2000 (from chipworks) 3

1.2 Different mechanisms of actuation for MEMS loudspeakers — (a) Piezoelectric, (b) Electrodynamic and (c) Electrostatic. 3

2.1 The three unitary steps composing a layer in a microfabrication process - (a) ”Deposition - Photolithography - etch” sequence and (b) ”Photolithography - Deposition - lift-off” sequence 9

2.2 Reaction chamber of the PECVD system used in this work for the deposition of a-Si:H/n^+. 11

2.3 (a) Shadow effect for lift-off processes and (b) isotropic vs anisotropic etch. 12

2.4 Etching mechanism of (a) ion milling, (b) hight-pressure plasma and (b) RIE. From Bhushan [2004] 12

2.5 Surface micromachining vs Bulk micromachining 13

2.6 3D models of the first generation loudspeakers for the (a) *perpendicular* geometry and (b) *parallel* geometry. 14

2.7 Process overview of the first generation loudspeakers. 14

2.8 3D models of the rectangular clamped geometry and the suspended-square geometry. Not to scale. 17

2.9 Loudspeaker process summary. 18

2.10 Substrate alignment with mask aligner 19

2.11 Design detail for DRIE control site 20

2.12 SiO_2 passivation layer detail at perforation site. 20

2.13 Cracks on a a-Si:H film from the residual stress as deposited using recipe in Table 2.1. . . 21

2.14 a-Si:H deposition test process summary. 22

2.15 Test sample used to first verify the feasibility of the DRIE process. 23

2.16 SEM micrographs of the DRIE cross-section on the first test sample with perforations' diameter of 40 μm and 80 μm from centre to centre. 24

2.17 Opical inspection of the second DRIE test with perforation's diameter of 80 μm and 160 μm from centre to centre. 25

2.18 HF VPE undercut rate 26

2.19 Detail on release structure right after the HF VPE in the a-Si:H deposition test process (see Figure 2.14) highlighting the residues left. 26

3.1 Thin beam example 28
3.2 Non-dimensional natural frequencies Ω_n and the corresponding mode shapes. 33
3.3 Effect of the applied axial stress on the resonance frequency of clamped thin beams. . . . 33
3.4 Frequency spectrum of the normalized displacement of the central position of a thin beam under a concentrated load at its center. 36
3.5 Thin rectangular plate example. 36
3.6 First resonance modes for a square clamped plate without in-plane forces or concentrated masses. 41
3.7 Normalized frequency spectrum for the normalized central deflection of a clamped square plate 42
3.8 Thin circular plate example. 43
3.9 First 4 axial symmetric natural mode shapes for a clamped circular plate with no concentrated mass nor axial stress 44
3.10 Effect of the applied axial stress on the resonance frequency of clamped thin beams. . . . 44
3.11 Normalized frequency spectrum for the normalized central deflection of a clamped circular plate 46
3.12 One-degree-of-freedom (odf) approximation. The membrane with mass m, Young's modulus E and area S is converted into a mass-spring system with effective mass m_0, elastic constant k_e and an effective area S_0. The electrostatic and damping force geometry dependency is included on the elastic constant and damping coefficient, respectively. 46
3.13 Geometry nomenclature. 48
3.14 (a) Concept of a perforation cell and (b) 2-dimensional flow model. 50

4.1 Quasi-DC experimental setup 58
4.2 (a) Frequency spectrum in the audible range of a 300 μm by 300 μm membrane held by 200 μm long tethers and (b) amplitude of deflection at 20 Hz of a 500 μm by 500 μm membrane held by 100 μm long tethers at constant DC bias as a function of the input excitation signal. 59
4.3 High-frequency experimental setup. 60
4.4 Frequency spectrum overview for the suspended squares for different membrane dimensions. 61
4.5 First resonance frequency as a function of the side of the membrane for the suspended square geometry with in-plane tensile stress. 61
4.6 Effect of the bias voltage on the (a) resonance peak shape and (b) resonance frequency for a suspended square with 210 μm side. 62
4.7 Frequency spectrum of a clamped rectangular membrane with 500 μm radius. 62
4.8 Detail on the two highest resonance peaks in Figure 4.7 63

4.9 First resonance frequency variation across a single die of 500 μm clamped membranes. . 63

4.10 Second generation released clamped membranes fabricated using the amorphous silicon deposition test process. Sub-figure (a) shows 500 μm circular membrane and sub-figure (b) shows an array of released membranes. 64

4.11 Frequency spectrum of a 800 μm clamped membrane for the silicon-silica process. 64

5.1 Changing the area of the suspended square independently of the length of the tethers. The anchor points are are marked as black. 66

5.2 (a) First resonance frequency f_0 as a function of the compressive stress for 2 μm thick circular membranes with different radius and (b) the critical compressive axial stress at which the membrane will buckle as function of membrane's radius for different thicknesses. . . 67

5.3 Effect of radial tensile stress on the first resonance frequency of circular membranes. . . 68

5.4 Effect of radial tensile stress on the first resonance frequency of thin beams. 69

5.5 Elastic constant (a) and resonance frequency (b) as a function of the side and thickness of a rectangular membrane without axial stress. The case for circular plates yields very similar values as can be seen from table (3.5). 70

5.6 Pull-in effect 71

5.7 Sample waveform for the numerical solution of the equation of motion (3.107) and for the small amplitude approximation (3.143). Sub-figure (a) show the case where the small displacement approximation is in good agreement with the complete solution of equation (3.107) and sub-figure (b) show the case where the small displacement approximation starts to fail and the waveform distortion must be taken into account. The plot range is from 0 to $1/3$ of the air gap height. 72

5.8 Feedback technique to eliminate the pull-in effect using (a) a simple capacitor or (b) a MOS capacitor. 72

5.9 Effect of the perforated geometry on the maximum displacement of the membrane. 73

5.10 The effect of perforation density on the frequency spectrum of the oscillator for constant membrane area and thickness, electrostatic pressure and air gap height. 74

5.11 Equivalent circuit of the resonator. 76

5.12 Equivalent circuit for the electric/mechanic domain of a electrostatic loudspeaker. 76

5.13 Possible circuit for mechano-acoustical model of the loudspeaker 77

List of Abbreviations

APCVD	Ambient Pressure Chemical Vapor Deposition
CMOS	Complementary Metal-Oxide-Semiconductor
CVD	Chemical Vapor Deposition
DRIE	Deep Reactive Ion Etching
ECM	Electret Condenser Microphones
IC	Integrated-circuits
LPCVD	Low Pressure Chemical Vapor Deposition
MEMS	MicroElectroMechanical Systems
ODF	One Degree of Freedom
PE	Polarization - Electric field
PECVD	Plasma Enhanced Chemical Vapor Deposition
RIE	Reactive Ion Etching
SPL	Sound Pressure Level
UHVCVD	Ultra High Vacuum Chemical Vapor Deposition

Chapter 1

Introduction

Thin film technology is currently implemented in virtually every modern device. First developed for the integrated-circuit (IC) industry, it has quickly widespread to many other fields of application such as MicroElectroMechanical systems (MEMS) — MEMS use the transduction between electrical and mechanical energy for the realization of sensors or actuators.

In this work it is explored the possibilities for acoustic applications focusing on the mechanical description and microfabrication of electrostatic MEMS loudspeakers. It is not the purpose of this work to develop and characterize a fully functional device but rather to explore novel fabrication processes/designs based on PECVD deposited amorphous silicon and surface micromachining technology. A collaboration with Inesc-ID is setting the guide lines for the development of an ultra-low power, low cost, electrostatic actuated loudspeaker for hearing aids applications.

1.1 State-of-the-art

1.1.1 MEMS Microphones

Several years ago MEMS started to enter the acoustics field through microphones. MEMS microphones are currently being adopted for many portable devices such as smartphones, tablets or laptops with a projected revenue of $493.5 million for 2012 and $667.0 million by 2015 (IHS iSuppli Research, January 2012) and are replacing the conventional electret condenser microphones (ECM) (Bouchaud [2012]). Advantages of MEMS microphones include immunity to electromagnetic interference and radio frequency radiation (for digital microphones), directionality, noise cancellation by using arrays of microphones, on-chip integration, CMOS compatibility and better performance and stability metrics (Dixon [2006]).

The microphone working principle is the transduction of acoustical energy into electrical energy by conversion of mechanical movement to an electrical signal. Transduction mechanisms for silicon MEMS include piezoelectric, piezoresistive and condenser (Scheeper et al. [1994]).

Piezoelectric microphones are comprised of a double layer cantilever made with piezoelectric materials of opposite polarization or a diaphragm provided with a piezoelectric. The deflection of the cantilever due to the incident pressure wave causes stress in the piezoelectric material which is converted to a voltage drop. Different implementation of this principle have been carried out and a comprehensive analysis on high performance piezoelectric MEMS microphones ca be found at Littrell [2010]. In this work the test structure are wide cantilevers with three 100 nm Mo electrodes and two 1.0 μm piezoelectric layers of AlN. Deep Reactive Ion Etching (DRIE) was used for the backside cavity etch. The author shows a sensitivity of 0.588 mV/Pa and a noise floor 8 - 11 times lower (34 dBA and 37 dBA) than the commercially available products at the time using only 62% - 92% of sensing area of previously reported devices.

Piezoresistive microphones work on a Wheatstone bridge configuration with 2 resistors placed on the edge of a membrane and the other 2 resistors placed on the centre of the membrane. Upon deflection of the membrane, the strain at the middle and border of the membrane have opposite sign (Scheeper et al. [1994]). Schellin and Hess [1992] fabricated a 1 μm thick membrane with $\sim 1mm^2$ area. A sensitivity of 25 $\mu V\ Pa^{-1}$ and a flat frequency response of 100 Hz to 5 kHz (± 3 dB) was demonstrated. One advantage of piezoresistive microphone is their low output impedance.

Capacitive microphones are comprised of a parallel plate capacitor with a perforated membrane as one of the plates. When the membrane deflects, the air gap eight between the plates changes and so does the capacitance of the system. The change in capacitance is then converted to a voltage change by an appropriate integrated circuit. This is the most widely implemented mechanism for MEMS microphones nowadays due to their high sensitivity, low noise floor and wide flat response across the audible spectrum (Rombach et al. [2002], Goto et al. [2007], Dehé [2007], Li et al. [2001], Miao et al. [2002], Shu et al. [2008], Bergqvist and Rudolf [1994]). A combination of surface and bulk micromachining is currently employed to achieved single wafer processing although other methods were successfully implemented as proof-of-concept. Typically the back cavity is achieved by bulk micromachining while the air gap between the diaphragm and the gate is achieved by surface micromachining. Different material have been used for the diaphragm including crystalline silicon, polysilicon, silicon nitrate, polymers, metals and heterogeneous layers. The diaphragm sensing area can range from half a millimetre to 2 mm millimetre in most cases with a sub-micron thickness in the case of silicon. The use of silicon is usually preferred due to its high stability and durability when compared to polymers. A cross sectional view of a microphone by Knowles implemented on iPhone4 is depicted in figure 1.1 (a). A monolithic process for CMOS-MEMS integration has also been developed for microphones and speakers (Neumann and Gabriel [2008], Neumann and Gabriel [2002], Huang et al. [2011]) circumventing the need for wirebonding or wafer transfer methods (figure 1.1 (b)). Here a metal layer of the CMOS process is used as the diaphragm.

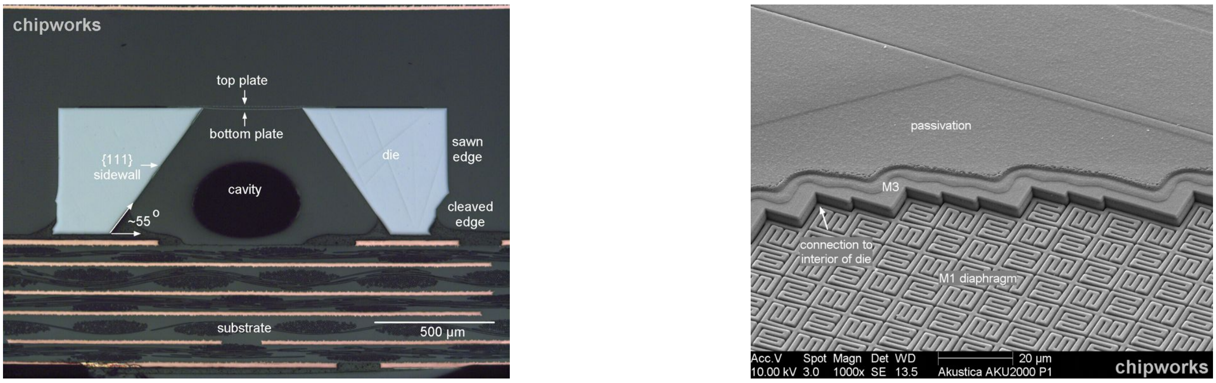

(a) (b)

Figure 1.1: Two examples of current implementations of a MEMS microphones — (a) Knowles S2.14 MEMS die cross section. (from chipworks) and (b) SEM micrograph of the microphone diaphragm of Akustica's AKU2000 (from chipworks)

1.1.2 MEMS Loudspeakers

Contrary to microphones, MEMS loudspeakers are more difficult to implement due to the necessity of large deflections or large areas of actuation to achieve the desired sound pressure level (SPL). Possible applications include mobile devices (Cho et al. [2009], Kim et al. [2005], Kim et al. [2009], Lemarquand et al. [2012a], Cheng et al. [2004]), hearing aids (Je and Chae [2008], Je et al. [2009]) and ultrasonic systems (Rangsten et al. [1996], Kim et al. [2012]) using different mechanisms of actuation such as piezoelectric, electrostatic, electrodynamic and thermoacoustic (Table 1.1).

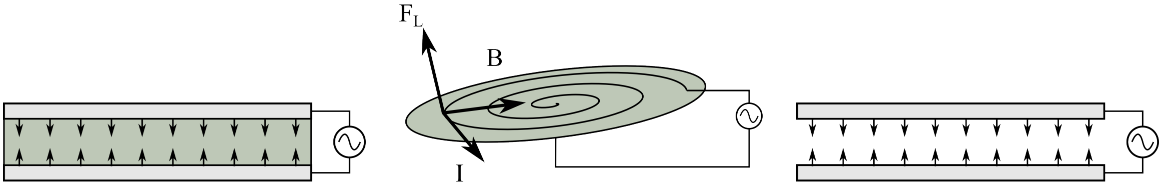

(a) (b) (c)

Figure 1.2: Different mechanisms of actuation for MEMS loudspeakers — (a) Piezoelectric, (b) Electrodynamic and (c) Electrostatic.

Piezoelectric

Piezoelectric actuation is based on the contraction of a piezoelectric block in between two electrodes by applying an external electric field (Figure 1.2 (a)). Typical materials include ZnO and PZT usually deposited on top of a silicon nitride layer for mechanical control and stability. Piezoelectric loudspeakers enjoy of a robust fabrication process and are easily scalable for large areas, as far as hundreds of mm^2. Also they radiate as a monopole, circumventing the need for front-side / back-side isolation. Their disadvantage is the presence of a polarization - electric field (PE) hysteresis curve and a low first resonance frequency leading to a very non-linear response in the audible range. Lee and White [1998] report on a piezoelectric cantilever that operates as a microspeaker or a voltage-to-frequency converter. They use ZnO on a low-stress LPCVD SiN as the deflecting membrane showing a 70 dB SPL at 5 kHz, measured at 50 mm from the device, for a driving voltage of 8 V_{pp}. For the voltage-to-frequency modality, they demonstrate linear behaviour arround 13 kHz with a sensitivity of 200 Hz/V. Ko et al. [2003] report on a ZnO on LPCVD SiN membrane that can work both as a microphone or microspeaker. They show deflection of the order of 1 μm with a maximum SPL of 83.1 dB at 13.3 kHz, measure 1 cm apart, for a driving voltage of 30 V_{pp}. For the microphone they show a sensitivity of 0.51 mV/Pa at 7.3 kHz with a noise level of 18 dB SPL. Yi and Kim [2005] report on a ZnO membrane deposited on a high compressive stress SiN film clamming a performance comparable to those found in electro-dynamic and piezo-ceramic devices for mobile devices. They demonstrate a 92 dB SPL at 3 kHz, measured 2 mm away from the speaker, for a membrane with 25 mm^2 driven at 6 V_{pp}. Kim et al. [2009] present a high performance microspeaker with very large active area (18 mm x 20 mm) using only PZT on a silicone damping layer. They show 90 dB SPL at 2 kHz, measured 1 cm away, for a driving voltage of 16 V_{pp}.

Electrodynamic

Electrodynamic actuation is based on the Lorentz force. In the presence of a magnetic field a current line experiences a force perpendicular to the current line and the magnetic field. The magnetic field is typically generated by a permanent magnet. Metal tracks are incorporated in the membrane and the deflection is controlled by the current's magnitude (Figure 1.2 (b)). Soft magnets are usually present to focus the magnetic field. The electrodynamic transduction mechanism is the most common in the literature with several different proposed devices. It's main advantages are large deflections, low-power and linear deflection with the input current. The chief drawback is a complex microfabrication process and difficulties in the full integration of magnetic materials using present MEMS' technology. Shearwood et al. [1996] presented a poyimide membrane on a GaAs substrate showing a deflection of 8 μm at 1 kHz and a maximum SPL of 106 measured in a 2cc coupler connected to an artificial ear. They use a 1 mm^3 SmCo magnet to create the permanent magnetic field. Rehder et al. [2001] show a balanced configuration where they use two permanent magnets to generate the magnetic field. Here the a soft magnet membrane is used and the planar coils are patterned on the supporting substrate. The system is design for 106 dB in a 2 cc coupler with a esstimated deflection of 12 μm and power consumption of 0.5 mW. Full fabrication is not shown however nor measured results of SPL or deflection. Cheng et al. [2004] report on a polyimide membrane for hearing instruments. They use a single embed coper coil with a rare-earth NdFeB hard magnet directly bellow. A silicon wafer is used as support for the membrane and a glass substrate is used for the permanent magnet. A Ni/Fe soft magnet is also present for focusing of the magnetic field. They show a deflection of 3 μm for a driving voltage of 1.5 V_{pp} and measured 93 dB SPL on a 2cc coupler at 5 kHz. Je et al. [2009] report on a polyimide membrane for hearing aids applications. The membrane has embed copper coils and a NiFe core at its centre with an annular NbFeB hard magnet concentric with the membrane. They measured a maximum deflection of 0.8 μm for an input current of 8 mA, corresponding to a power consumption of 0.13 mW, in a 3 mm diameter membrane. Acoustics measurements are not presented. Chen and Cheng [2011] reports on a PDMS membrane for hearing aids applications. The device is similar to the one presented by Cheng et al. [2004] using a single Cu coil, a NdFeB hard magnet bellow the membrane and a NiFe soft magnet for field focusing. The membrane is fabricatated on a Si substrate while the hard magnet is placed on an acrylic supporting board. They show a displacement of 8.3 μm for a 3.5 diameter membrane and demonstrate 106 dB SPL at 1 kHz in a 2cc coupler for a power consumption of 1.76 mW. Shahosseini et al. [2013] report on an unprecedented membrane displacement of 650 μm using an electromagnetic actuated silicon rigid membrane with 7.5 mm radius. The process employed (Lemarquand et al. [2012a]) is rather complex with special techniques having to be implemented for the deposition of copper tracks that define the current loop. The aim of this structure are mobile devices such as smart phones or laptops and such large displacement are achieved for near 1W power consumption.

Electrostatic

Electrostatic actuation is based on a parallel plate capacitor using one fixed electrode, called the *gate electrode*, a one suspended electrode, called the *membrane* or the *diaphragm*. The deflection is caused by the electrostatic pressure arising from the voltage difference across the electrodes imposed by an external source (Figure 1.2 (c)). Electrostatic actuation is well suited for very low power application and integrability with CMOS dies. The main disadvantages of electrostatic driving is a high voltage cost and low deflection amplitudes. Rangsten et al. [1996] reports on a Si membrane operated in a *rolling* mode. They show 112 dB SPL at 127 kHz at 10 mm for 50 V_{pp} input voltage. Kim et al. [2005] developed a double gate excitation version of this principle to drive Parylene membrane using a wafer bonding method. A deflection of 7.5 μm was reported for a 15 mm^2 active area with a measured 98.8 dB SPL at 13.8 kHz, 10 mm away from the speaker, for an input voltage of 200 V_{pp}. Roberts et al. [2007] report on a touch-mode Poly-SiC microspeaker. They show a deflection of 8 μm (size of the air gap) in a 8 mm diameter membrane corresponding to 73 dB at 16.59 kHz, 10 mm away, for an input voltage of 200 V_{pp}.

Actuation type	Membrane's Material	Maximum deflection	Active area dimensions	Maximum Sound Pressure Level (SPL)	Power	Driving Voltage	Reported by
Piezoelectric	ZnO + SiN	-	2 × 2 mm^2	70 dB at 5 kHz at 50 mm	-	8 V$_{\text{pp}}$	Lee and White [1998]
	ZnO + SiN	1 μm at 7.3 kHz	3 × 3 mm^2	83.1 dB at 13.3 kHz at 1 cm	-	30 V$_{\text{pp}}$	Ko et al. [2003]
	ZnO + SiN	-	5 × 5 mm^2	92 dB at 3 kHz at 2mm	-	6 V$_{\text{pp}}$	Yi and Kim [2005]
	PZT	-	18 × 20 mm^2	90 dB at 2 kHz at 1 cm	-	16 V$_{\text{pp}}$	Kim et al. [2009]
	PZT + Polyimide	-	2 mm diameter	87 dB at 5 kHz in acoustic coupler	-	26 V$_{pp}$	Cho et al. [2009]
Electrostatic	Si	-	2 mm diameter	112 dB at 127 kHz at 10 mm	-	50 V$_{\text{pp}}$	Rangsten et al. [1996]
	Parylene	7.5 μm	3 × 5 mm^2	98.8 dB at 13.8 kHz at 1 cm	-	200 V$_{\text{pp}}$	Kim et al. [2005]
	Poly-SiC	8 μm	0.8 mm diameter	73 dB at 16.59 kHz at 1 cm	-	200 V$_{\text{pp}}$	Roberts et al. [2007]
Electrodynamic	Polyimide	8 μm	8 mm diameter	105 dB at 1 kHz on artificial hear	-	-	Shearwood et al. [1996]
	Soft magnet	12 μm	4.9 mm diameter	106 dB at 1 kHz in 2cc coupler	0.5 mW	-	Rehder et al. [2001]
	Polyimide	3 μm	3.5 mm diameter	93 dB at 5 kHz in 2cc coupler	320 mW	1.5 V$_{\text{pp}}$	Cheng et al. [2004]
	Polyimide	0.8 μm	3 mm diameter	106 dB at 1 kHz in 2cc coupler	0.13 mW	-	Je et al. [2009]
	PDMS	8.3 μm	3.5 mm diameter	106 dB at 1 kHz in 2cc coupler	1.76 mW	-	Chen and Cheng [2011]
	Si	300 μm	15 mm diameter	80 dB at 0.33 kHz at 10 cm	0.5 W	-	Shahosseini et al. [2013]
Thermoacoustic	Carbon nanotubes	NA	3 × 3 cm^2	85 dB at 10 kHz at 5 cm	3 W	50 V$_{\text{rms}}$	Xiao et al. [2008]

Table 1.1: Summary of MEMS loudspeakers presented in the literature

1.2 Motivation

Electrostatic MEMS loudspeakers present some advantages over electrodynamic or piezoelectric driven loudspeakers — they can be integrated in a CMOS dies, using common materials such as silicon, aluminium or silicon dioxide, they have no DC power consumption and require very low alternating current amplitude avoiding local heating and material deterioration. Unfortunately they present strong disadvantages such as high driving voltages and low amplitudes of deflection when compared to electrodynamic actuation, for example. The devices proposed here aim for a very low driving voltage of 3.3 V, with deflection of the order of 1 μm. The design and choice of materials itself also allows arraying of single structures, thus proving lower acoustic waveform deformation over large areas of actuation and better control over the membranes mechanical properties. For the particular application of hearing aids, low driving voltages with ultra-low power consumption and large areas of actuation are required. The purposed devices deliver on all these requirements. Moreover, the novelty of the fabrication process in this field, overcoming the large voltage cost drawback, allows the possibility of entering on the virtually unexplored market of MEMS loudspekers for hearing aids. Finally, large area MEMS have strong applications in other areas such as microfluidics, physical sensors, biosensors or electronic components. While the process development and structural characterization and optimization is acoustic oriented, valuable know-how is to be retained for such other applications.

1.3 Thesis outline

The document is organized in 6 chapters. Chapter 2 introduces basic concepts on microfabrication, describes the processes and equipment used and describes in detail the microfabrication process of the proposed devices. Chapter 3 provides a theoretical background on how the purposed structures are modelled. Chapter 4 introduces the experimental setup used to characterize the fabricated structures and present experimental data for initial mechanical characterization. In Chapter 5 a general discussion over design principles is provided focusing on how each variables affects the overall performed of the system and their limitations. Finally, Chapter 6 presents the major achievements, conclusions and future work.

Chapter 2

Microfabrication

The microfabrication of the proposed structures is presented here. An introduction to basic concepts and principles of relevance on microfabrication are first presented. Description of the different techniques, equipment used and general consideration are covered. The detailed process for the microfabrication of the loudspeaker is then presented. A detailed view on the fundamentals of the techniques present here can be found in any book on microfabrication such as Madou [2002] or Franssila [2004].

2.1 Basic principles and concepts

2.1.1 Layers

In a microfabrication process a *layer* is defined by a set of three *unitary steps* - deposition, photolithography and etch (see figure (2.1)). The first is responsible for depositing or growing the desired material on top of the sample. There are several methods for different material, some of which are described bellow. Several material can be deposited in a row forming a *stack*. Next, in the photolithography step, a mask is patterned by using a photo-sensible material, typically a polymer known as photoresist, that is spin-coated on top of the deposited material(s). The photoresist is then *exposed*, with the intended pattern, and, by the use of a developer, sections of this material are removed and the remaining is hardened. Finally, the etch step consists on removing the deposited material that is unprotected by

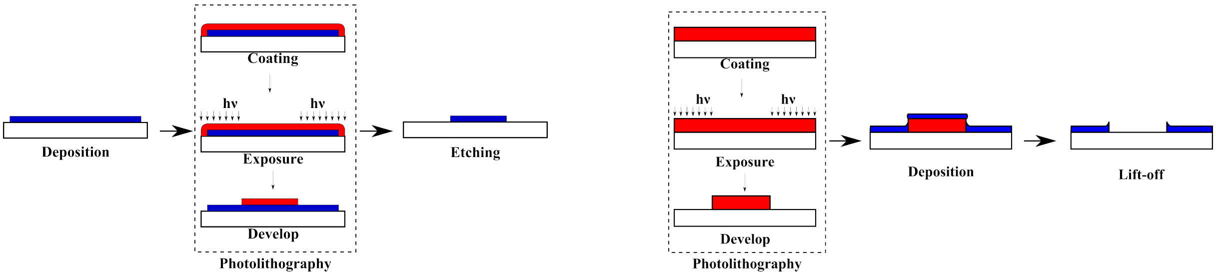

(a)

(b)

Figure 2.1: The three unitary steps composing a layer in a microfabrication process - (a) ”Deposition - Photolithography - etch” sequence and (b) ”Photolithography - Deposition - lift-off” sequence

the mask followed by the removal of the photoresist.

An alternative sequence is the one commonly known as *lift-off*. Here the photolithography is the first step, followed by the deposition (figure 2.1 (b)). This sequence allows that, during the deposition, only parts of the material are deposited on the sample while the rest ”sits” on top of the photoresist. The photoresist is then removed (the lift-off) leaving the patterned material on the sample. The chief advantage is the forfending of the etch step which for complex processes, where poor selectivity exists, may become a problem. The downside is that the pattering of the photoresist must be optimize to produce a *shadow effect* (Figure 2.3) to avoid the ”ears” after the photoresist strip (as exemplified in Figure 2.1 (b)) and increase the yield of the process.

In the next subsections an introduction to the microfabrication methods of relevance is presented.

2.1.2 Deposition and Etching techniques

Sputter deposition

Sputter deposition is one form of *physical vapor deposition* (PVD) where material is ablated from a target and deposited on top of the sample by means of its residual kinetic energy. The ablation process uses a plasma of an inert gas, such as Ar, typically confined by magnetic fields and driven by either a rf of dc high electric field. The ions of the plasma are accelerated toward the target, causing the ablation, and the ejected atoms travel through the plasma and residual gas in the chamber to the sample. Sputter depositions yield mild isotropic deposition profiles.

Plasma Enhanced Chemical Vapor Deposition (PECVD)

PECVD is a type of Chemical Vapor Deposition (CVD) where the material is form in a gas state through a series of chemical reaction and deposited on top the sample. There are several types of CVD such as *Low Pressure CVD* (LPCVD), *Ambient Pressure CVD* (APCVD), *Ultrahigh vacuum CVD* (UHVCVD) and others. In a PECVD process the sample is placed in between two electrodes where the plasma is struck. The activation of the chemical species in the chamber is aided by the energy available in the plasma allowing the temperature of the substrate to be lower than in other forms of CVD. This forms the main advantage of PECVD, making it suitable for a variety of substrates such as processed integrated circuits.

The PECVD system used in this work is composed of a load-lock and two reaction chamber. The first reaction chamber isn’t used here and the sample is transported directly to the second reaction chamber. Here a planar PECVD geometry is used as pictured in Figure 2.2. The sample is placed in contact with one of the electrodes and the plasma is generated by a RF power supply. The temperature of the electrode can be controlled externally as well as the pressure inside the chamber and gas flows. Very conformal deposition can be achieved although not as good as in LPCVD (Madou [2002]).

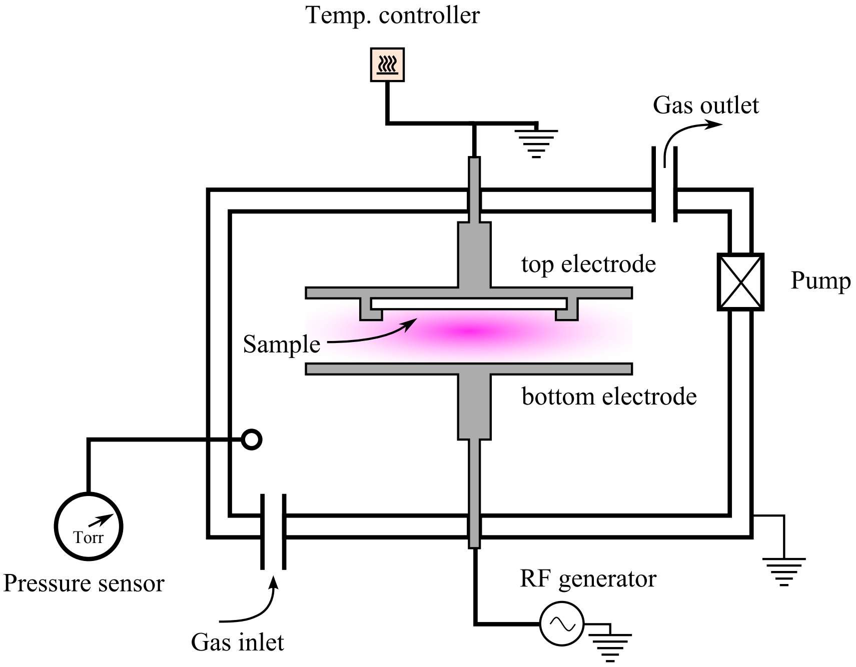

Figure 2.2: Reaction chamber of the PECVD system used in this work for the deposition of a-Si:H/n^+.

Wet etching

Wet etching is a purely chemical etch where the sample is simply submerge in the etching liquid, called the etchant, for a given amount of time. The etchant can be a pure or diluted chemical agent such as hydrofluoric acid (HF), phosphoric acid (H_3PO_4) or potassium hydroxide (KOH) or it can be a combination of reagents such as in the case of the aluminum etchant where a combination of nitric acid (HNO_3 - oxidizes the aluminum surface), H_3PO_4 (dissolves the aluminum oxide (Al_2O_3)), acetic acid (CH_3COOH - for wetting and buffering) and H_2O (for dilution and etch rate control) is present. With the exception of crystalline solids such as silicon wet etching yields a very isotropic etch profile with very high selectivity. The great disadvantage of a wet etch, when compared with other etch processes where more complex a specialized machinery is required, is the lack of control in the etch stop or etch rate. Small variations in the temperature, etchant composition or in the material itself affect the etch rate making this process unreliable when high selectivity doesn't exist.

Vapor phase etching (VPE)

As wet etching, VPE is also a purely chemical, isotropic etch with the difference that the reaction occurs in the vapor phase. The etch is usually performed at controlled temperature and pressure depending on the etching agent. Two common chemical are used in the silicon industry - hydrofluoric acid (HF) for the etch of silicon dioxide (SiO_2) with high selectivity toward Si and xenon difluoride (XeF_2) for the etch of Si with high selectivity toward SiO_2. Here, HF is used to etch the SiO_2 sacrificial layer (see below) which has several benefits over its liquid counterpart such as selectivity towards Al and Al_2O_3 and suppression of the stiction effect during the structure release phase.

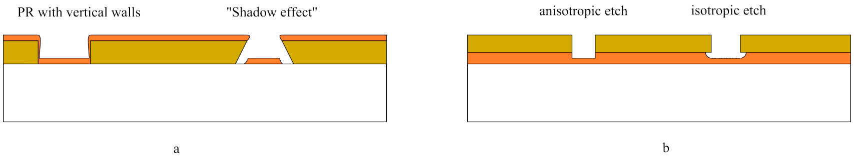

Figure 2.3: (a) Shadow effect for lift-off processes and (b) isotropic vs anisotropic etch.

Reactive Ion Etching (RIE) and Deep Reactive Ion etching (DRIE)

RIE is a combination of chemical and physical etching. Having a geometry similar to the planar PECVD, the sample is bombarded with ions from the plasma, activating the species at the surface. The surface is then chemically etch by the reactive gases present in the chamber. The RIE offers high selectivity and anisotropy since only activated species that reacted with the gases in the chamber will be etch and, due to the incoming angle of the bombarding particles, the horizontal surface will suffer much more incoming than the vertical walls (see figure 2.4 (c)). DRIE uses a two-step cycle to achieve high aspect ratio features —First a RIE etch and second a passivation of the surface by polymerization which further protects the side-walls increasing the anisotropy of the process.

2.1.3 Basic MEMS processing

A basic requirement of MEMS processing is the fabrication of a suspended feature (with a few exceptions such as piezoelectric devices). There are two essential ways of achieving this using thin film technology — *Bulk micromachining* and *Surface micromachining* (Figure 2.5). The former uses the substrate as the sacrificial layer and in, same cases, as the structural layer as well. This works much like a sculpture where parts of the initial substrate are remove to achieve the desired shape. The latter is and additive process where both the structural and sacrificial layer are deposited and patterned on the substrate. A combination of both surface and bulk micromachining is used in this work.

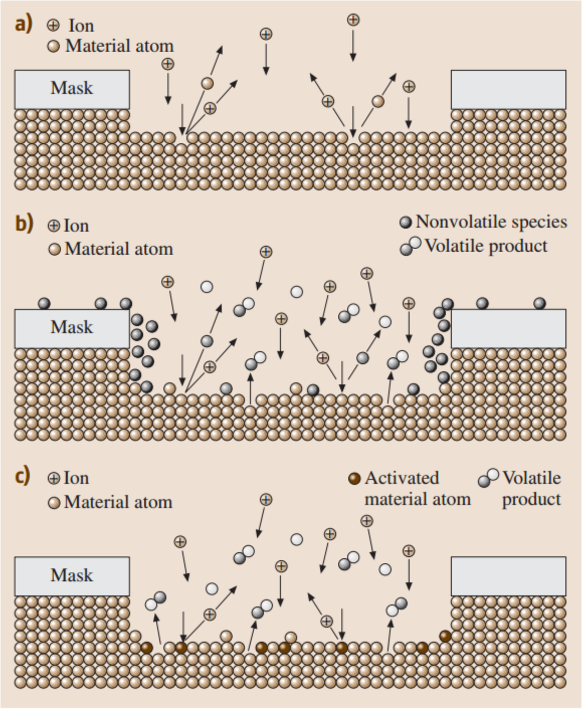

Figure 2.4: Etching mechanism of (a) ion milling, (b) hight-pressure plasma and (b) RIE. From Bhushan [2004]

Bulk micromachining is a particular robust process with several years of optimization and currently present in successful technologies such as digital micro mirrors, MEMS pressure sensors or MEMS microphones. The vast know-how inherited from the IC industry for processing Si/SiO$_2$ devices, the anisotropic etching proper-

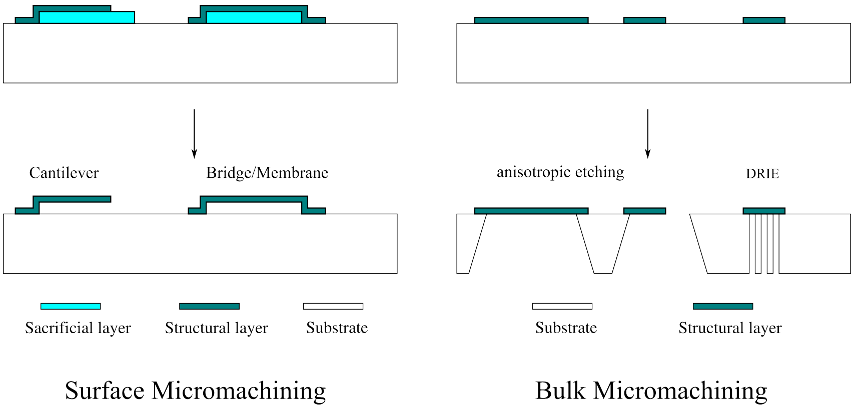

Figure 2.5: Surface micromachining vs Bulk micromachining

ties of crystalline silicon and the development of the DRIE process are in centre of this technology success. Surface micromachining started to show as an appealing alternative to its bulk counterpart due to its high flexibility in the choice of materials (and therefore in the processing technologies used) and new designs usually not possible in bulk micromachining. In particular, the possibility for the choice of substrate allows the development of MEMS on glass or flexible substrates.

Surface micromachining processing is based on three central steps —patterning of a sacrificial layer, patterning of a structural layer and removal of the sacrificial layer. The deposition and etching of the structural layer and the removal of the sacrificial layer — commonly knows as *release* — are the critical steps in this process and essentially determine the intrinsic performance of the device. The deposition of the structural layers will determine its intrinsic properties such as intrinsic stress, electric conductivity or its Young's modulus. The removal of the sacrificial layer is a delicate step which can lead to the complete failure of the process. Two ways exist for the removal of sacrificial layer — wet etching or VPE. A common problem with wet etching is *stiction* (Yapu [2003]) — Stiction is the collapse of the structural layer due to capillary forces arising at the liquid-gas interface after the etch is complete and the liquid is drying (not necessarily the etchant). This is usually avoided by passing the devices through liquids of successively decreasing surface tension or by using a CO_2 critical-point drying method. Although VPE is a cleaner and simpler process it imposes restrictions on the materials choice whereas wet etching allows for a much wider choice of materials.

2.2 The loudspeaker

The microfabrication process for the electrostatic MEMS loudspeaker is now presented. Two processes are described — a first generation process resulting from the extension of a previously well developed process for thin beams and bulk resonators and a second generation process developed in view of the incompatibility of the former for a loudspeaker application (see Chapter 5).

2.2.1 First generation

The first approach to the problem was to extended the well developed standard process for thin beams and bulk resonators at *INECS-MN* to thin plates with large areas, held by four tethers (Figure 2.6). The design includes tethers with 100 μm, 150 μm, 200 μm and 250 μm in combination with membrane sides of 300 μm, 400 μm and 500 μm separated into two designs here designated by *perpendicular* (Figure 2.6 (a)) and *parallel* (Figure 2.6 (b)).

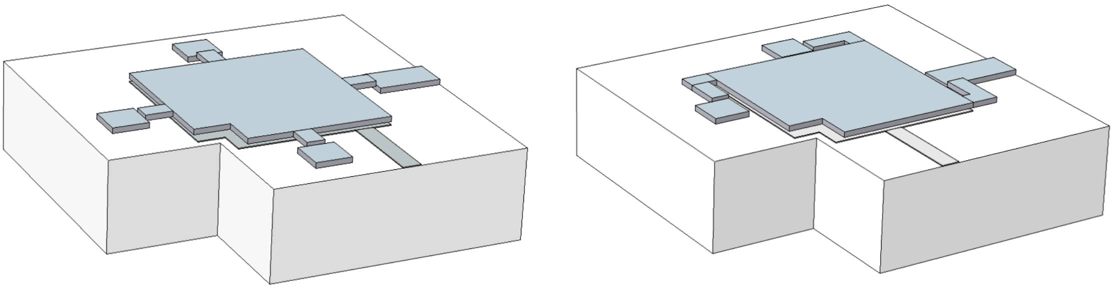
(a) (b)

Figure 2.6: 3D models of the first generation loudspeakers for the (a) *perpendicular* geometry and (b) *parallel* geometry.

Process overview

The process is summarized in Figure 2.7 —(a) The process starts with the cleaning of a two by one inch glass substrate; (b) A sputtered TiW layer is patterned by RIE to define the gate electrode; (c) Sputtered aluminium is used to defined the sacrificial layer by wet etching; (d) the structural double layer a-Si:H/TiW is patterned by a single step of RIE and (e, f) the substrate is diced into individual dies and the sacrificial layer is removed by wet etching, releasing the structure.

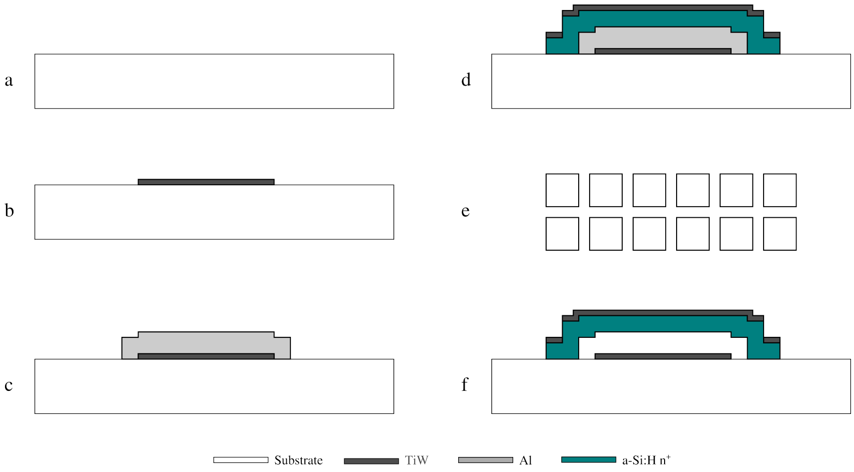

Figure 2.7: Process overview of the first generation loudspeakers. a) 2 inch by 1 inch glass substrate; b)Patterning of the TiW gate; c) Patterning of the Al sacrificial layer; d) Patterning of the a-Si:H/TiW structural layer; e) Dicing and f) structure release. Not to scale.

Process detail

Photolithography There are a total of 3 lithography steps to define the 3 layers. The process is the same for all layers — The sample is subjected to a vapor prime followed by photoresist spin-coating, it is then exposed using a direct write method and finally it's developed.

Vapor Prime Vapor prime promotes the adhesion of the photoresist to the substrate. The sample is exposed to a hexamethyldisilazane HDMS atmosphere at 130 $^\circ$ C and 6 Torr for 5 minutes.

Coating The spin-coating is performed on a *SVG Spin-on-glass planarization track* using photoresist (PFR-7790G27CP, JSR Micro) as the coating material. This is a fully automated process comprised of three steps: 1) The material is spin-coated on top of a 6 inch silicon wafer; 2) the wafer is baked at 85 ^{o}C for 1 minute; 3) The wafer is cooled down for 1 minutes. The process is optimized for a 1.5 μm target thickness.

Exposure The exposure is done on a *Heidelberg Instruments Direct Write Laser Lithography System*. The laser is a HeCd laser (l=442 nm (g-line) / write lens NA= 0.85). The laser follows the pattern provided from a CAD file. The process is optimized for a photo-resist thickness of 1.5 μm so, for the structural layer, the exposure step is repeated to assure that the photo-resist is exposed through all its thickness.

Develop Developing is also performed on the SVG track. The process start with a pre-bake at 110 ^{o}C for 1 minute and subsequent cooling for 30 s and then is subjected to the developer (TMA238WA, JSR Micro) for one minute and washed out in deionized water.

Resist strip Resist strip is the common step after etching for removal of the photoresist. The sample is submerged in *Microstrip 3001* at 65 $^\circ$ C for 30 minutes to 1 hour. It is then rinsed with di-water and IPA and blow dry with compressed air. Longer times of stripping may be required if the photoresist baked during the etch process.

TiW gate TiW is deposited in a *Nordiko 7000 Magnetron Sputtering System*. Deposition rate of 40 A/s are typical. The pattering is performed by RIE using the same recipe used for etching a-Si:H. This layer defines the gate electrodes for electrostatic actuation.

Al sacrificial layer Al is deposited in a *Nordiko 7000 Magnetron Sputtering System* at 2 kW power for a target thickness between 1 μm to 2 μm. Deposition rates of 40 A/s are typical. Patterning is performed by wet etching using *Gravure Aluminium etchant* which as highly selectivity towards aluminium. This layer defines the sacrificial layer. Besides occupying the area where the structure will be suspended the aluminium also protects the underlying layer of TiW because of the RIE to pattern the structural layer.

a-Si:H/Al structural layer The a-Si:H is deposited in a *Plasma Enhanced Chemical Vapor Deposition system*. A target thickness of 3 μm is used with deposition rates around 33 nm/s. The TiW is deposited next, with a target thickness of $0.15 \mu m$ in the Nordiko system. Here a low power recipe is used, at 0.5 kW with cooling steps in between, to avoid overheating of the substrate, reducing the thermal stress between layers. The metallization increases the conductivity of the structural layer assuring a constant potential distributions over the membrane. The layer is pattern in a single step of RIE. Usually a lithography with a 3 μm thick photoresist layer is used because the etch also attacks the photoresist with selectivity around 1:3.

Dicing Before releasing the structures, the substrate is diced into individual 6.5 $\times$ 6.5 mm^2 dies in a *Disco Dicing Saw*. The sample is coated with 1.5 μm photoresist to avoid damages cause by shrapnel coming from the dicing zone.

Structure release Structure release is performed by wet etching at room temperature. Each die is submerged in aluminium etchant for the required amount of time which depends on the geometry of each die. Undercut rates around 80 nm/min are typical. After the etch is complete each die is transferred to DI-water to stop the aluminium etchant. They are then transferred to IPA which has lower surface tension than water and finally to n-Hex which has even lower surface tension than IPA. Each die is then left in open air to evaporate the n-Hex. This is the critical step in this process. Because there isn't any automation, an high degree of variability may exist from die to die. Also, stiction imposes a maximum length on the membranes that can withstand this process without collapsing.

Modified process for clamped geometries

A modified version of this process was also use for the fabrication of fully clamped structures. The process replicates the one described in Figure 2.7 with the addition of an alumina layer between the gate electrode and the sacrificial layer, to provide electric isolation, patterned by lift-off. The deposition conditions are described bellow.

2.2.2 Second generation

The proposed structures for the second generation of loudspeakers are depicted in Figure 2.8 — a clamped a-Si:H plate (a) and a suspended square plate (b) held by four tethers. Each membrane is separated by an *air gap* from a gate electrode for electrostatic actuation and the lateral dimensions, membrane side or diameter, are much larger than the air gap height or the thickness of the membrane. The gate electrode and substrate are perforated from side to side to introduce vent holes in order to decrease the compression of air between the membrane and substrate and allow the back-wave to propagate (see Chapter 5). Also, to assure a constant spatial distribution of the electrical potential through out the membrane, a metal layer is present on top of the membrane, with thickness much smaller than the membrane's. Finally, aluminium oxide (Al_2O_3) layers are introduce between the gate and substrate and between the gate and membrane in the case of the clamped geometries for electrical isolation.

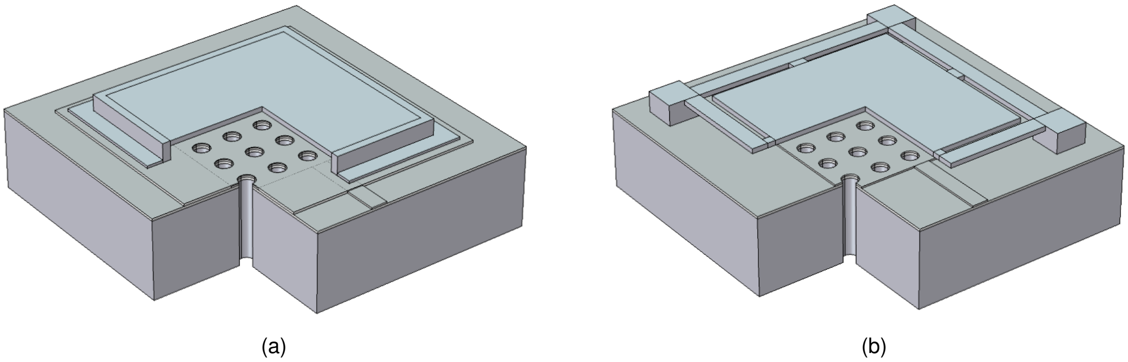
(a) (b)

Figure 2.8: 3D models of the rectangular clamped geometry and the suspended-square geometry. Not to scale.

Process overview

The proposed process is a 7 layer process with one layer on the back-side of the sample plus 6 layers on the front-side of the sample. A summary of the process is depicted in figure 2.9

Alignment marks are first etched on both sides of a double side polished, undoped $< 100 >$ silicon wafer and individual rectangular substrates with 2 inch by 1 inch are diced from the silicon wafer. Sputtered alumina (Al_2O_3) is first patterned with a wet etch on the back-side of the sample. This will be used latter on as the hard mask for the DRIE of the substrate. A similar alumina layer is patterned on the front-side of the sample for electrical isolation of the substrate. The gate contacts are then defined using sputtered aluminium together with a wet etch. A silica layer is introduce for passivation of the underling Al layer. Another alumina layer is patterned on top of the gate layer for electrical isolation between the gate and membrane. The SiO_2 sacrificial layer is then defined using a PECVD step together with a RIE step. The a-Si:H/Al structural layer is deposited using a PECVD step for the a-Si:H and a sputter deposition for the aluminium. The aluminium is first patterned using a wet etch and the a-Si:H using a RIE step. The substrate is then perforated from the back-side using a DRIE step. The sample is diced into individual dies for the release step with HF vapor finishing the microfabrication process. For the suspended square geometry the process is almost exactly the same with the difference that the alumina layer for electrical isolation between gate and membrane and the SiO_2 passivation layer are not present.

Process detail

Photolithography There are a total of 9 lithography steps to define the 7 layers plus the alignment marks for front-side/back-side alignment. The process is the same for all layers — The sample is subjected to a vapor prime followed by photoresist spin-coating, it is then exposed using a direct write method and finally it's developed. The same conditions described above are used.

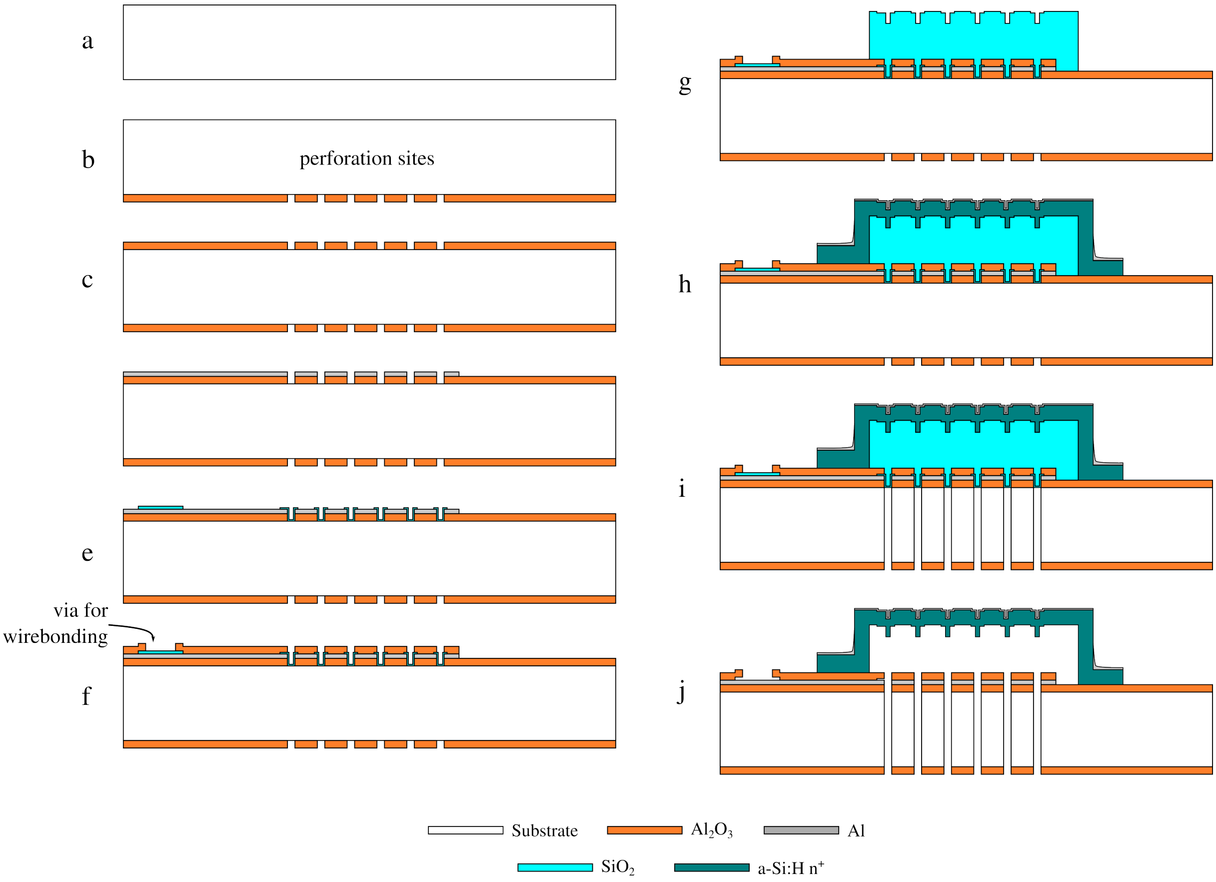

Figure 2.9: Loudspeaker process summary. Each step represent the deposition, lithography and etch of the indicated material (see text for detail). (a) The process starts with a c-Si substrate with front-side/back-side alignment; (b) Alumina hard mask for the DRIE step (i); (c) Alumina layer for gate-substrate electric isolation; (d) Aluminium gate layer for electrostatic actuation; e) Silica layer to protect the underling Al layer; f) Alumina layer for gate-membrane electronic isolation; g) Silica sacrificial layer; h) a-Si:H n^+ / Al structural layer; i) Substrate DRIE; j) Silica VPE (Structure release). Image not to scale.

Front-side/Back-side alignment To be able to process on both sides aligned marks must be present on both sides of the substrate. First, using standard lithography and RIE, specific alignment marks are written on one of sides, say the front-side, of the substrate. Then, using a Mask Aligner (*Karl Suss MA6 BA6*) alignment marks are exposed on the back-side, aligned with the alignment marks written on the front-side (see Figure 2.10). The mask aligner makes use of two alignment microscopes that can lock into a known position — based on the specific alignment marks previously written on the front-side — and expose the back-side.

Because the working substrate must be a rectangular with 2 inch by 1 inch a full wafer is aligned and the rectangular substrates are diced from the wafer.

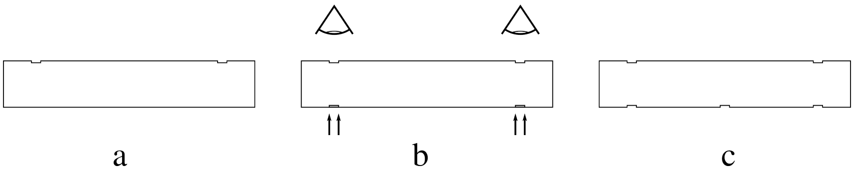

Figure 2.10: Substrate alignment with mask aligner. (a) Initial alignment marks are pattern on the front-side of the wafer; (b) Using these marks, a mask aligner exposes new alignment marks at known positions, relative to the front-side marks, on the back-side. (c) New marks are written on the back-side for further reference.

Al_2O_3 back-side hard mask The alumina deposition is accomplished in a planar magnetron sputtering system for a target thickness of 200 nm. Typical deposition rates are around 0.11 nm/min. The layer is patterned by wet etching using aluminium etchant (*Gravure Aluminium*) at 85 ° C. Because a consistent etch rate is very difficult to obtain the etch is performed until a 1 μm to 2 μm undercut is visible to ensure that the etch is complete. This undercut should be accounted for during the design of the mask for the lithography. Finally, a quick RIE step is performed to ensure that the Si substrate is exposed. Here a mixture of SF_6, O_2 and He is used with typical etch rates of 5 nm/s.

Al_2O_3 layer for substrate-gate electric isolation The deposition is performed in a planar magnetron sputtering system for a target thickness of 200 nm with typical deposition rates around 0.11 nm/min. The mask design is quite similar to the back-side hard mask with a small difference — at one of the structures' sites the alumina is "opened" to be used as a control during the DRIE of the substrate (see Figure 2.11 and the discussion below).

The etch is performed again by wet etching but because the back-side layer is also alumina the sample is placed on an adherent film, with the front-side facing upwards, to protect the back-side. Also the etch is performed until a 1 μm to 2 μm undercut is visible to ensure that the alumina is completely etched.

Aluminium gate electrode Aluminium metallizations are performed on a *Nordiko 7000 Magnetron Sputtering System* for a target thickness of 1500 Å. Typical deposition rates are around 36 Å/s. The layer is pattern by wet etching. The same etchant as the one used for the alumina layers is used but here at roam temperature which has no effect on the alumina for the time scale involved (3 to 5 minutes). Typical etch rates are about 50 nm/min.

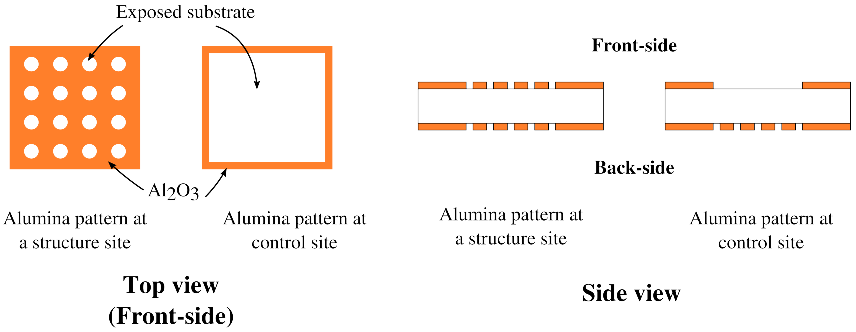

Figure 2.11: Design detail for DRIE control site. At one of the perforation sites the alumina layer is ”opened” for control during the substrate DRIE.

SiO_2 passivation layer A thin silica layer is introduce to protect the underling layer of Al from the wet etch of the following alumina layer (see Figure 2.12). There are two sites that need passivation, one where vias for wirebonding will be opened (see Figure 2.9 (f)) and another for the perforation sites (see Figure 2.12). The deposition is performed by sputtering for a target thickness of 50 nm and patterned by RIE. This passivation layer is then removed during the structure release.

This passivation step can be avoided if the following alumina layer is patterned by lift-off. The lift-off process however requires careful optimization and relies on the ability to create a *shadow effect* (see Figure 2.3). If this shadow effect cannot be created consistently the stripper will not be able to dissolve the photoresist leading to an incomplete process. Because each structure has many perforation sites a very high yield is required.

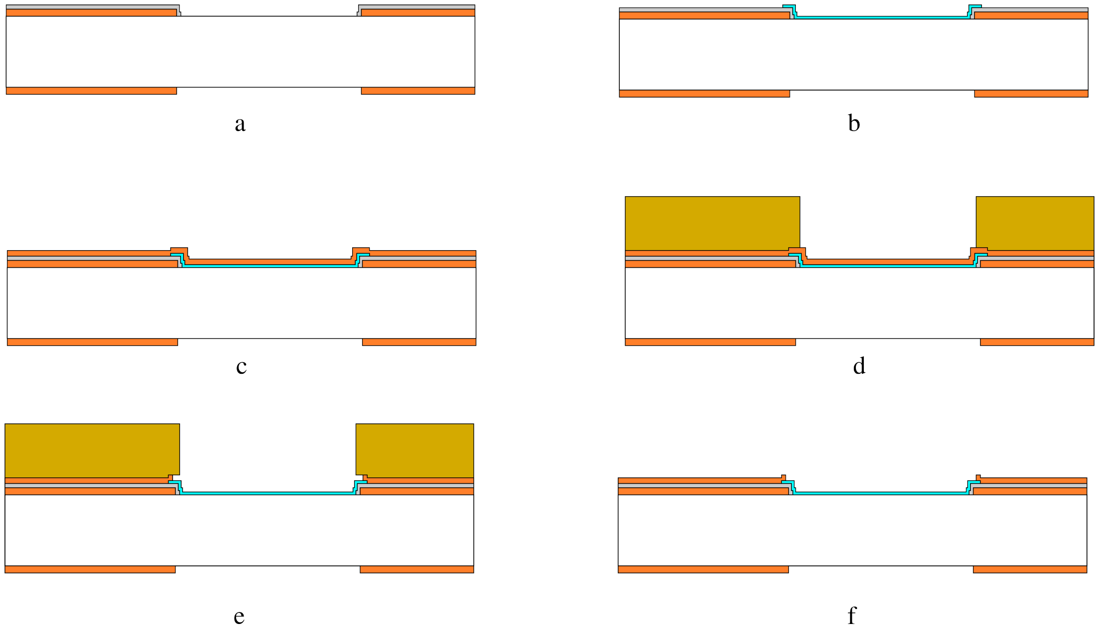

Figure 2.12: SiO_2 passivation layer detail at perforation site. a) After the aluminium gate pattering (Figure 2.9 (d)); b) SiO_2 passivation layer pattering covering 10 μm of the aluminium layer; c) Alumina deposition; d) Lithography for the alumina etch; e) Alumina etch with a 2 μm to 3 μm undercut; f) Resist strip.

Al_2O_3 gate-membrane electric isolation The deposition is performed in a planar magnetron sputtering system for a target thickness of 200 nm with typical deposition rates around 0.11 nm/min. The pattern is equal to the one of the alumina layer for gate-substrate isolation with the addition of vias for wire bonding (Figure 2.9 (f)). The alumina is pattern by wet etching with the same procedure described above for the other alumina layer.

SiO_2 sacrificial layer The SiO_2 is deposited by PECVD in a *Electrotech Delta Chemical Vapor Deposition System*. Deposition rates of the order of 20 nm/s are typical. The patterning is performed by RIE using a CHF_3/CF_4 mixture with typical etch rate of 10 A/s. Because a thick layer is required here, of the order 1 to 3 μm, a long etch time is typical. To avoid baking the photoresist the etch is performed in steps of 200s with cool down intervals of 60s. Finally, an oxygen plasma RIE is performed to clean organic contaminants from the CHF_3/CF_4 etch step.

a-Si:H n+ / Al structural layer The hydrogenated amorphous silicon is deposited by PECVD in a planar PECVD system. Previous work describe the intrinsic mechanic and optic properties of these films and optimization for MEMS on glass with aluminium as sacrificial layer has been extensively performed (Alpuim et al. [1999], Gaspar et al. [2003], Gualdino et al. [2012], Gaspar et al. [2012], Sousa et al. [2012]). Recent work shows that both the substrate and the sacrificial layer have a strong effect on the properties of the film, in particular, in its residual stress. A film that shows zero apparent residual stress in a glass-aluminium device can have very high residual stress in a silicon-silica device as shown in Figure 2.13. Even for a film with no visible fractures, residual stress will be present and upon release of the structures it may be sufficient to buckle or fracture, specially in clamped geometries.

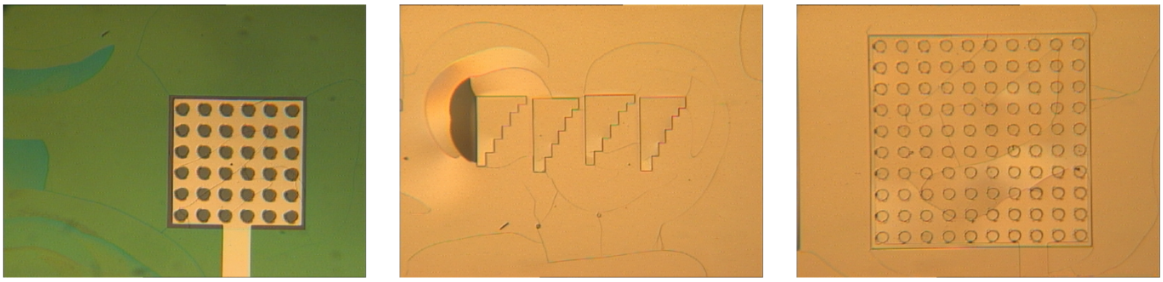
(a) (b) (c)

Figure 2.13: Cracks on a a-Si:H film from the residual stress as deposited using recipe in Table 2.1.

To optimize the deposition conditions a simplified version of this process is used, summarized in figure 2.14, here designed by the *amorphous silicon deposition conditions test* process. By keeping every layer, except for the back-side hard mask for the DRIE, the optimization is performed under the same exact conditions as if it were the complete process and it is possible to have working membranes to further characterize its mechanical properties. The membrane is perforated to allow the HF vapour to reach the sacrificial layer. The diameter of the perforations are however smaller to avoid as much as possible weakening of the membrane.

Four recipes were used (see table 2.1 to obtain a stable film. Recipe 1 was used for a target thickness

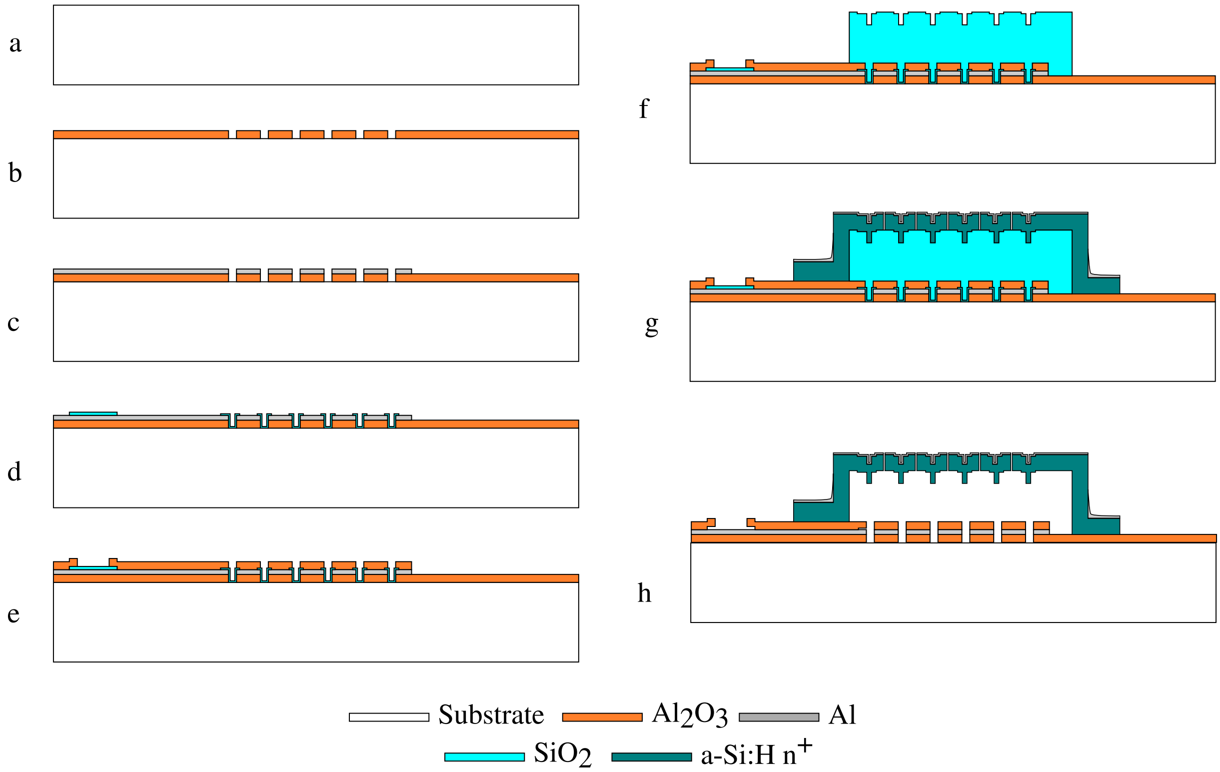

Figure 2.14: a-Si:H deposition test process summary. Each step represent the deposition, lithography and etch of the indicated material (see text for detail). (a) The process starts with a c-Si substrate; (b) Alumina layer for gate-substrate electric isolation; (c) Aluminium gate layer for electrostatic actuation; (d) Silica layer to protect the underling Al layer; (e) Alumina layer for gate-membrane electronic isolation; (f) Silica sacrificial layer; (g) a-Si:H n^+ / Al structural layer; Silica VPE (Structure release). Image not to scale.

Recipe	Pressure (Torr)	Power (W)	Temperature (° C)	SiH_4 (sccm)	PH_3 (sccm)	H_2 (sccm)	H_2 Dilution (%)
1	1	25	150/200	10	5	25	75
2	1	25	150/200	10	5	28	77
3	1	25	150/200	7	3.5	23	79
4	1	25	150/200	7	3.5	28	82

Table 2.1: Amorphous silicon deposition conditions

of 2 μm yielding very high levels of stress and the film was visibly peeled after deposition (Figure 2.13). The form of the cracks is consistent with tensile stress which lead to the increase of the content of hydrogen to 77% (previously 75 %) and a decrease in the film thickness to 1 μm in recipe 2. Although the film did not peeled during deposition, it was attacked by the developer during the developing step of the lithography resulting in a ”lift-off” effect. A recipe optimized to bulk resonators, 3 μm thick was then used with an hydrogen content of 79% and 82 % (recipe 3 and 4, respectively). These recipes yield very stable films which, although tensile stress is still present (see Chapter 4), did allowed the realization of clamped geometries using both the glass-aluminium and silicon-silica process.
Aluminium is then deposited in the Nordiko system at lower power (0.5 kW) to reduce the thermal stress between layer and patterned with a wet etch. The same photoresist mask and the aluminum itself are used to pattern the a-Si:H with an RIE step. Finally, an oxygen plasma RIE is performed to clean organic contaminants from the SF_3/CHF_3 etch step.

Substrate DRIE The substrate DRIE is performed on a SPTS Pegasus system at the *International Iberian Nanotechnology Laboratory* (INL). To first investigate the feasibility of the process a test sample was used as indicated in Figure 2.15. The sample is mounted on a carrying wafer on top of a wax (Figure 2.15 (b)) to assure good thermal contacts between the carrying wafer and the sample. This is particularly important in a DRIE process to assure a constant and uniform etch rate throughout all the substrate.

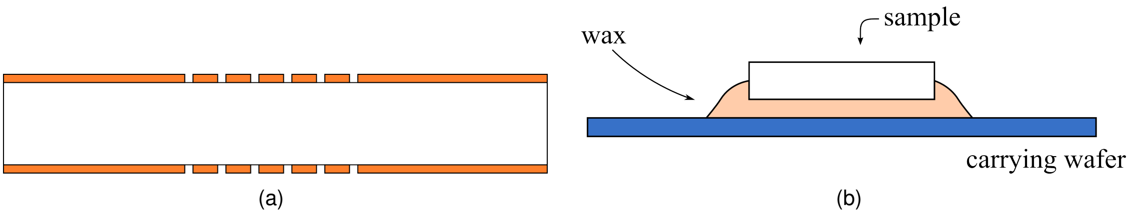

Figure 2.15: (a) Test sample used to first verify the feasibility of the DRIE process ; (b) the sample is placed in a carrying wafer on top of wax to assure good thermal contact.

The test samples have a geometry equal to the one used for the actual device. For the first run the perforations were design with a diameter of 40 μm in a substrate 750 μm thick, meaning an aspect ratio of approximately 1:19. The total etch time was 139 minutes and 56 seconds. After the etch is complete the alumina hard mask is striped in aluminium etchant and the substrate is diced, both with a dicing saw and a diamond tip. The results are shown in Figure 2.16. Of first notice is the visible damage to the top side of the sample (Figure 2.16 (e)). This is attributed to the dicing process and not to the etch itself.

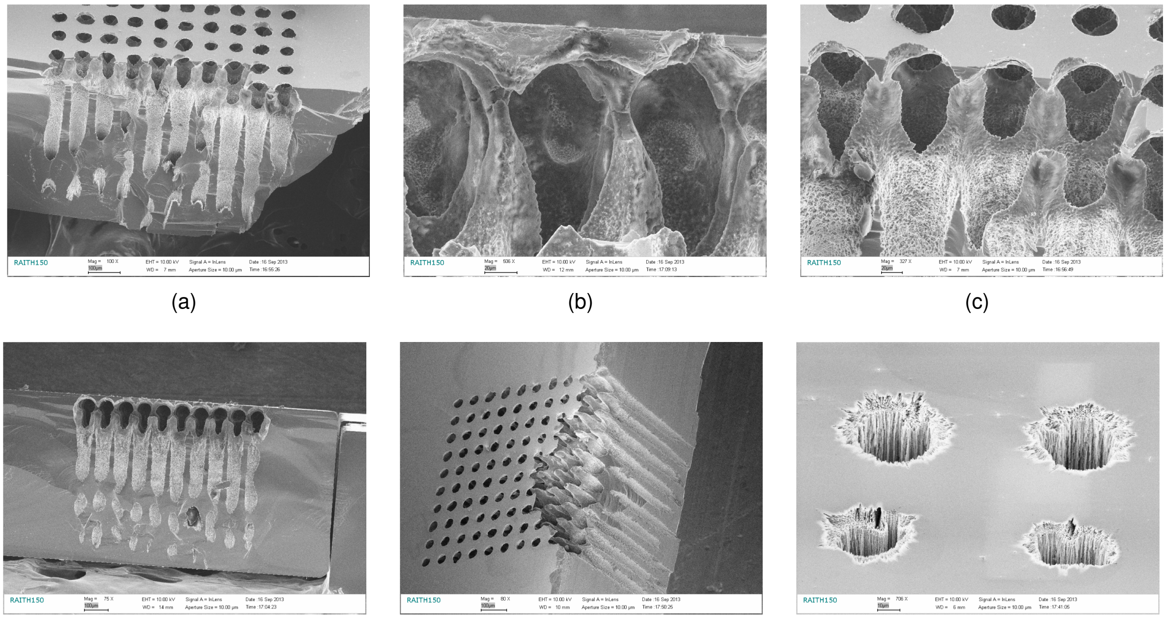

(a) (b) (c)

(d) (e) (f)

Figure 2.16: SEM micrographs of the DRIE cross-section on the first test sample with perforations' diameter of 40 μm and 80 μm from centre to centre.

Cross-section micrographs are specially difficult to obtain for dense or complex geometries without the proper tools. Nonetheless, a detail view on the etch profile is not the objective here but rather to verify if the perforation of the substrate is complete. As can be seen from Figure 2.16 (e) the perforation does go all the way through with an arguably constant diameter, except at the very end where it starts narrowing. This is not consistent throughout the sample though as can be seen from sub-figures (a) or (d). Another point of notice is the initial widening of the perforations, visible on Figure (2.16) (a) for example. This is not a characteristic aspect of a DRIE step where the perforations' diameter is expected to narrow instead. Also a ladder effect is expected from the cyclic nature of the process. From Figure 2.16 (f) it is clear that the walls were strongly attacked probably contributing to the widening of the perforation.

Perhaps too ambitious for a first try! A second test was performed now with a more flexible geometry — 80 μm for the diameter of the perforations, corresponding to an aspect ration of $\approx$ 1:9, and a less dense geometry with 160 μm between adjacent perforations, from centre to centre. Also only one batch with total time of 65 min was performed. An example by optical is shown in Figure 2.17. The damage at the top of the sample (front-side) is attributed to the cleaving of the substrate. The perforation has a much more uniform lateral profile and uniform depth[1]. The etch rate in a DRIE process is usually a function of time, it decreases has the aspect-ratio increases, so a third test would have to be performed for an etch time longer than 65 minutes to assess the total time required to open the substrate from side to side. At the time a substrate 750 μm thick was used for practical purposes but 350 μm thick wafers are a possibility and should allow more tolerance in this step as well as perforations diameters as small as 20 μm.

---

[1] The same depth is measured across the substrate with a variation less than 10 μm

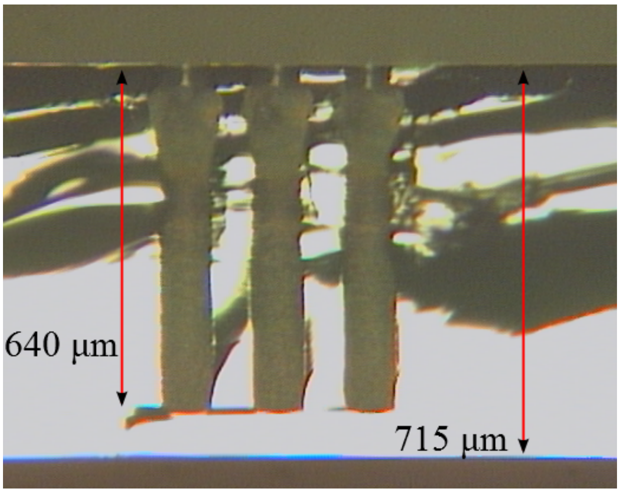

Figure 2.17: Opical inspection of the second DRIE test with perforation's diameter of 80 μm and 160 μm from centre to centre.

Dicing Before performing the structure release the rectangular substrate is diced into individual dies of 6.5 mm by 6.5 mm. A pre-coating of the substrate is usually performed to avoid damaging of the dies by shrapnel coming out of the dicing zone.

SiO2 HF VPE The silica sacrificial layer is removed using a HF VPE. As state above this is a critical step in MEMS processing and special care must be taken to avoid the collapsing of the suspended features or damaging the structural layer. Because this is a vapor phase etch there's no concern for *stiction* as there is only one phase during the whole process. Although hydrofluoric acid is very selective towards SiO_2 the etching is performed at high concentration and long over etch times are not recommended (see Figure 2.18 (e)). It is then crucial to have a well defined undercut rate as well as a dummy sample to track the progress of the etching.

A very simple solution, and the one employed here, is the fabrication of a SiO_2 / Al_2O_3 sample as exemplified in Figure 2.18 (a). The silica layer is deposited in the same batch as the one for the actual sample containing the devices to avoid discrepancies between different batches. The alumina layer is then patterned as described above. It works here as a hard mask and it is chosen due to its transparency making it easy to track the undercut of the underling silica. Note that because the devices are metallized on top its much harder to check where the etch front is due to the high reflectivity of the metal. To calculate the undercut rate the sample is subjected to several cycles of etching and the undercut front is measured by optical inspection at the end of each cycle (Figure 2.18). For the geometry presented 2 cycle are almost enough to complete the release and the third and fourth cycle are essentially over etch time to understand how the HF vapour reacts with alumina for prolonged exposure times and have better accuracy on the undercut rate regression. The linear regression yielded an undercut rate of 35.6 μm/cycle (data not shown).

For the a-Si:H deposition test process (see Figure 2.14) there were some residues left after the HF VPE. There are two distinct areas — the vertical wall of the structural layer and the bulk of the sacrificial layer. It is expected that the residues on the walls are coming from the RIE step used to pattern this layer. This may not be a very critical issue since for the complete process the sacrificial layer will be exposed to the HF from the perforation hole, within the membrane. The residues on the bulk of the sacrificial layer are

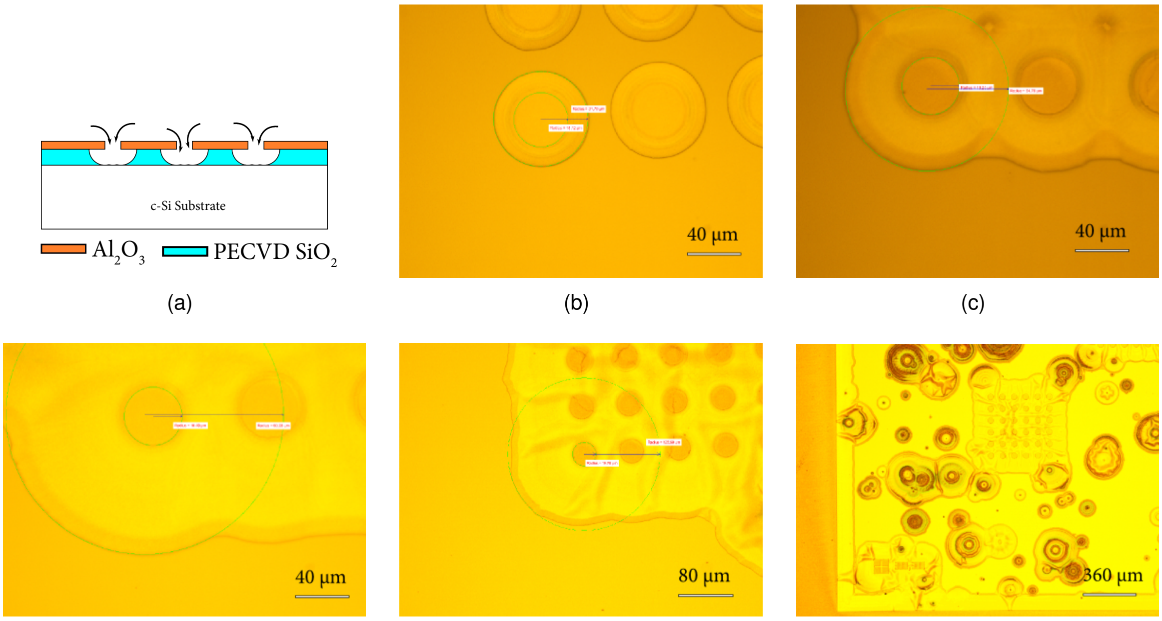

(a) (b) (c)

(d) (e) (f)

Figure 2.18: HF VPE undercut. The sample (a) is subjected to several cycles of etching and the undercut front is measured by optical inspection. Sub-figures (b) through (e) show the undercut front after (b) 1 cycle, (c) 2 cycles, (d) 3 cycles, (e) 4 cycles and (f) the overview after 4 cycles. This exemplifies why long exposure to the HF vapour should be avoid and a control sample is required.

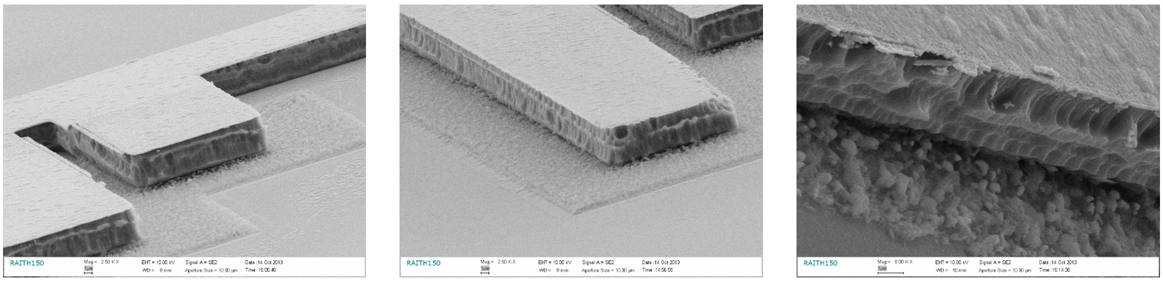

(a) (b) (c)

Figure 2.19: Detail on release structure right after the HF VPE in the a-Si:H deposition test process (see Figure 2.14) highlighting the residues left.

still an on-going problem. Although actuation is possible (see Chapter4), showing that the structures are indeed released, this is an undesired result.

Chapter 3

Theoretical description

An introduction to the basic theoretical elements for modelling harmonic vibrations of thin beams and plates is introduced in this chapter. The chapter is structured in four sections — thin beams, thin rectangular plates, thin circular plates and The one-degree-of-freedom approximation. The description is based on an energy formulation — the *extended Hamilton principle* (see Appendix B). The different contributions to the total energy are first presented based on the theory of deformation of linear isotropic elastic solids (see Appendix C) followed by the governing equation for the cases of thin beams and plates of constant cross-section including the contributions of in-plane, axial stress. The formalism for very general boundary conditions is also introduced. The special cases of interest for this work are then further developed and the equilibrium solutions for static loading and harmonic driving are presented. Finally a summary of the most important results is given. The discussion presented here follows closely the one in Magrab [2012] where a complete and rigorous description of the topic can be found.

3.1 Thin Beams

Consider the case of a thin beam under small transverse deflection as a result of a transverse, externally applied, force per unit length $f_a(x,t)$ (N/m) as exemplified in figure 3.1. The beam as length L (m), width b (m), thickness h (m), Young's modulus E (Pa) and Poisson Ration ν. It is assumed that the length of the beam is much greater than the width and thickness of the beam where the *Euler-Bernoulli theory* applies. The *neutral axis* (the axis equidistant form the top and bottom of the beam) experience no strain under deflection and therefore doesn't change in length. Also planes perpendicular to it remain unaltered in size under deflection of the beam. Attached to the boundary $x = 0$ there is a mass M_L with rotational inertia J_L, a translation spring with elastic constant k_L and a torsion spring k_{tL}. Analogously at the boundary $x = L$, there is a mass M_R with rotational inertia J_R, a translation spring with elastic constant k_R and a torsion spring k_{tR}.

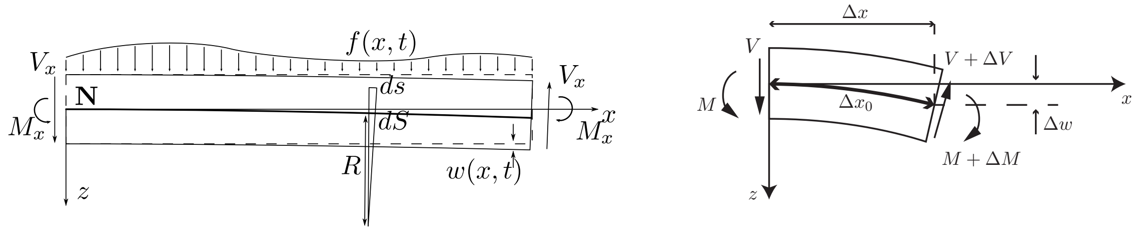

(a) (b)

Figure 3.1: Thin beam example

In terms of the strain tensor, the problem is translated as

$$\epsilon_{ij} = \begin{bmatrix} \epsilon_x & 0 & 0 \\ 0 & 0 & 0 \\ 0 & 0 & 0 \end{bmatrix} \tag{3.1}$$

From figure 3.1 and equation (C.7) one may write

$$\epsilon_x \equiv \frac{\mathrm{d}s - \mathrm{d}S}{\mathrm{d}S} = \frac{(R-z)\Delta\theta - R\Delta\theta}{R\Delta\theta} = -z\frac{1}{R} \tag{3.2}$$

where $\mathrm{d}S$ is the infinitesimal length of a fiber along the neutral axis, $\mathrm{d}s$ is the infinitesimal length of a fiber a distance z from the neutral axis, R is the local radius of curvature of the beam at position x and $\Delta\theta$ is the infinitesimal angle defined by the local curvature of the beam. The neutral axis is chosen to be at position $z = 0$.

The local curvature is given by (Hodges [1984])

$$\kappa \equiv \frac{1}{R} = \frac{(1+\partial u/\partial x)\partial^2 w/\partial x^2 - (\partial w/\partial x)\partial^2 u/\partial x^2}{\left[(1+\partial u/\partial x)^2 + (\partial w/\partial x)^2\right]^{3/2}} \tag{3.3}$$

which can be simplified to

$$\kappa \approx \frac{\partial^2 w}{\partial x^2} \tag{3.4}$$

since for small strains and negligible axial displacement

$$\frac{\partial u}{\partial x} \ll \frac{\partial w}{\partial x} \ll 1 \tag{3.5}$$

This way,

$$\epsilon_x = -z\frac{\partial^2 w}{\partial x^2} \tag{3.6}$$

and, from the stress-strain relations C.14 comes

$$\sigma_x = -E\frac{z}{R} = -Ez\frac{\partial^2 w}{\partial x^2} \tag{3.7}$$

The moment M_x at the internal cross-section of the beam around the neutral axis can be evaluated as

$$M_x(x) = \iint_A dA\ \sigma_x(x) z = -E\frac{\partial^2 w}{\partial x^2}\iint_A dA\ z^2 = -EI\frac{\partial^2 w}{\partial x^2} \qquad [\mathrm{N.m}] \tag{3.8}$$

where $I \equiv \iint_A dA\ z^2$ is the *area moment of inertia* of the beam. Although vertical shear strains are neglected in the *Euler-Bernoulli* theory, vertical shear forces, V, must be accounted for to balance the externally applied load. A simple moment balance around and infinitesimal segment of the beam (see Figure 3.1 (b)) immediately leads to

$$V(x) = \lim_{\Delta x \to 0}\left(\frac{\Delta M}{\Delta x} - \Delta V\right) = \frac{\partial}{\partial x}\left[EI(x)\frac{\partial^2 w}{\partial x^2}\right] \qquad [\mathrm{N}] \tag{3.9}$$

The different contribution to the total energy are now presented.

Strain energy From equations (C.17), (3.7) and (3.6) the strain energy is given by

$$U = \frac{1}{2}\iiint_V dV\ \sigma_x\epsilon_x = \frac{1}{2}E\int_{-w/2}^{w/2}dy\int_{-h/2}^{h/2}dz\int_0^L dx\ z^2\left(\frac{\partial^2 w}{\partial x^2}\right)^2 = \frac{1}{2}EI\int_0^L\left(\frac{\partial^2 w}{\partial x^2}\right)^2 dx \tag{3.10}$$

Kinetic Energy From equations (C.18) the kinetic energy is given by

$$T_\rho = \frac{1}{2}\iiint_V dV\ \rho\left(\frac{\partial w}{\partial t}\right)^2 = \frac{1}{2}\int_{-w/2}^{w/2}dy\int_{-h/2}^{h/2}dz\int_0^L dx\rho\left(\frac{\partial w}{\partial t}\right)^2 = \frac{1}{2}\rho A\int_0^L\left(\frac{\partial w}{\partial t}\right)^2 dx \tag{3.11}$$

where only the transverse displacement of the beam is accounted for.

External Forces The external forces are subdivided into a distributed transverse force $f_a(x,t)\hat{\mathrm{e}}_z$ $[\mathrm{N/m}]$ and an axial force $p(x,t)\hat{\mathrm{e}}_x$ $[\mathrm{N}]$.

The work done by the transverse force is given by

$$W_a = \int_0^L dx\ f_a(x,y)w(x,t) \tag{3.12}$$

When axial forces are present the neutral axis no longer remains constant in length. If the deformation is assumed to be small then, the change in length, Δ, can be approximated by

$$\Delta = ds - dx = \sqrt{dx^2 - dw^2} - dx = dx\left(\sqrt{1+\left(\frac{dw}{dx}\right)^2} - 1\right) \approx \frac{1}{2}\left(\frac{dw}{dx}\right)^2 dx \tag{3.13}$$

and the work done is given by

$$W_p = -\int_0^L dx\ p(x,t)\Delta = -\frac{1}{2}\int_0^L dx\ p(x,t)\left(\frac{\partial w}{\partial x}\right)^2 \tag{3.14}$$

The minus sign on W_p indicates that the force is tensile. If $p(x,t)$ is compressive a plus sign should be used instead.

The total work is then

$$W = W_a + W_p = int_0^L dx\ f_a(x,y)w(x,t) - \int_0^L dx\ p(x,t)\Delta = -\frac{1}{2}\int_0^L dx\ p(x,t)\left(\frac{\partial w}{\partial x}\right)^2 \tag{3.15}$$

Boundary attachments The minimization function at the boundaries, $F^{(C_1)}$, is given by the difference between the kinetic energy and the potential energy of the elements attached. This can be written straightforward as

$$\begin{aligned} F^{(C_1)} =& \frac{1}{2}(M_L\dot{w}^2(0,t) + J_L\dot{w}_x^2(0,t) + M_R\dot{w}^2(L,t) + J_R\dot{w}_x^2(L,t)) \\ &- \frac{1}{2}(k_L w^2(0,t) + k_{tL}w_x^2(0,t) + k_R w^2(L,t) + k_{tR}w_x^2(R,t)) \end{aligned} \tag{3.16}$$

3.1.1 Governing equation

From equations (B.2), (B.3), (3.10), (3.11), (3.12) and (3.14) the minimization function can now be written as

$$\begin{aligned} F =& \frac{1}{2}\rho A\left(\frac{\partial w}{\partial t}\right)^2 - \frac{1}{2}EI\left(\frac{\partial^2 w}{\partial x^2}\right)^2 \\ &+ f_a(x,t)w(x,t) - \frac{1}{2}p(x,t)\left(\frac{\partial w}{\partial x}\right) \end{aligned} \tag{3.17}$$

and from the one-dimensional particular case of equation (B.4) the governing equation is given by

$$\frac{\partial^2}{\partial x^2}\left(EI\frac{\partial^2 w}{\partial x^2}\right) - \frac{\partial}{\partial x}\left(p(x,t)\frac{\partial w}{\partial x}\right) + \rho A\frac{\partial^2 w}{\partial t^2} = f_a(x,t) \tag{3.18}$$

Boundary conditions

From the one dimensional particular case of equation (B.6) and (3.16) the boundary conditions are:
At $x = 0$, either $w(0,t) = 0$ or

$$\left[k_L w + M_L\frac{\partial^2 w}{\partial t^2} - p(x,t)\frac{\partial w}{\partial x}\right]_{x=0} + \frac{\partial}{\partial x}\left(EI\frac{\partial^2 w}{\partial x^2}\right)_{x=0} = 0 \tag{3.19}$$

and either $\partial w(0,t)/\partial x = 0$ or

$$\left[k_{tL}\frac{\partial w}{\partial x} + J_L\frac{\partial^3 w}{\partial x\partial t^2} - EI\frac{\partial^2 w}{\partial x^2}\right]_{x=0} = 0 \tag{3.20}$$

At $x = L$, either $w(L,t) = 0$ or

$$\left[k_R w + M_R\frac{\partial^2 w}{\partial t^2} - p(x,t)\frac{\partial w}{\partial x}\right]_{x=L} + \frac{\partial}{\partial x}\left(EI\frac{\partial^2 w}{\partial x^2}\right)_{x=L} = 0 \tag{3.21}$$

and either $\partial w(0,t)/\partial x = 0$ or

$$\left[k_{tR}\frac{\partial w}{\partial x} + J_R\frac{\partial^3 w}{\partial x\partial t^2} - EI\frac{\partial^2 w}{\partial x^2}\right]_{x=L} = 0 \tag{3.22}$$

Notice that these boundary conditions are simply force and moment balances at the respective boundary.

Typically boundary conditions such as clamped, hinged or simply support can be extracted directly from equations 3.19 to 3.22.

3.1.2 Natural frequencies and mode shapes

A complete description of the natural frequencies and mode shapes for very general boundary conditions and in-span attachments can be found at Magrab [2012]. Here, the special case of a clamped-clamped beam with constant axial force is presented.

The non-dimensional form of the governing equation is first present to simply the algebraic notation. Introducing the following notation

$$\begin{array}{cccc} \eta = x/L, & \tau = t/t_0, & y = w/L, & \Omega^4 = \omega^2 t_0^2 \\ t_0 = L^2\sqrt{A\rho/EI}\ [s], & m_b = \rho A L\ [kg], & S_0 = \frac{p_0 L^2}{EI} & \hat{f}_a = \frac{f_a L^3}{EI} \end{array} \tag{3.23}$$

the non-dimensional form the governing equation (3.18) is written as

$$\frac{\partial^4 y}{\partial \eta^4} - \frac{\partial}{\partial \eta}\left(S(\eta,\tau)\frac{\partial y}{\partial \eta}\right) + \frac{\partial^2 y}{\partial \tau^2} = \hat{f}_a(\eta,\tau) \tag{3.24}$$

with boundary conditions

$$y(0,\tau) = y'(0,\tau) = y(1,\tau) = y'(0,\tau) = 0 \tag{3.25}$$

Setting $p(x,t) = p_0$ and $\hat{f}_a(x,t) = 0$ in equation (3.24) yields

$$\frac{\partial^4 y}{\partial \eta^4} - S_0\frac{\partial^2 y}{\partial \eta^2} + \frac{\partial^2 y}{\partial \tau^2} = 0 \tag{3.26}$$

The natural modes must satisfy equation (3.26) with the boundary conditions (3.25).

The sought solution is assumed to be of the form

$$y(\eta,\tau) = Y(\eta)e^{j\Omega^2\tau} \tag{3.27}$$

given its harmonic temporal dependence. Substituting this into equation (3.26) yields

$$\frac{\partial^4 Y(\eta)}{\partial \eta^4} - S_0\frac{\partial^2 Y}{\partial \eta^2} - \Omega^4 Y(\eta) = 0 \tag{3.28}$$

The solution for this equation can be obtained by means of a *Laplace transformation* (see for example Riley et al. [2006]) yielding

$$Y(\eta) = Q(\eta;\Omega)Y(0) + R(\eta;\Omega)Y'(0) + S(\eta;\Omega)Y''(0) + T(\eta;\Omega)Y'''(0) \tag{3.29}$$

with

$$
\begin{aligned}
Q(\eta;\Omega) =& \frac{1}{\delta^2+\epsilon^2}(\delta^2\cos(\epsilon\eta)+\epsilon^2\cosh(\delta\eta)) & R(\eta;\Omega) =& \frac{1}{\delta^2+\epsilon^2}(\frac{\delta^2}{\epsilon}\sin(\epsilon\eta)+\frac{\epsilon^2}{\delta}\sinh(\delta\eta)) \\
S(\eta;\Omega) =& \frac{1}{\delta^2+\epsilon^2}(-\cos(\epsilon\eta)+\cosh(\delta\eta)) & T(\eta;\Omega) =& \frac{1}{\delta^2+\epsilon^2}(-\frac{1}{\epsilon}\sin(\epsilon\eta)+\frac{1}{\delta}\sinh(\delta\eta)) \\
\delta^2 =& \frac{S_0}{2}+\sqrt{\left(\frac{S_0}{2}\right)^2+\Omega^4} & \epsilon^2 =& -\frac{S_0}{2}+\sqrt{\left(\frac{S_0}{2}\right)^2+\Omega^4}
\end{aligned}
\tag{3.30}
$$

From the boundary conditions at $\eta = 0$ the first two terms are null leaving only the two unknowns $Y''(0)$ and $Y'''(0)$. Using the other two boundary conditions at $\eta = 1$ yields a system of 2 linear equations with two unknowns given by, in matrix form,

$$
\begin{bmatrix} S(1;\Omega) & T(1;\Omega) \\ S'(1;\Omega) & T'(1;\Omega) \end{bmatrix} \begin{bmatrix} Y''(1) \\ Y'''(1) \end{bmatrix} = 0 \tag{3.31}
$$

which has a non-trivial solution only if

$$
\begin{aligned}
D(\Omega) \equiv \det\left(\begin{bmatrix} S(1;\Omega) & T(1;\Omega) \\ S'(1;\Omega) & T'(1;\Omega) \end{bmatrix}\right) &= S(1;\Omega)T'(1;\Omega) - T(1;\Omega)S'(1;\Omega) = \\
&= S^2(1;\Omega) - T(1;\Omega)S'(1;\Omega) = 0
\end{aligned}
\tag{3.32}
$$

Equation (3.32) is called the *characteristic equation*. The values $\Omega = \Omega_n$ for which equation (3.32) is verified are called the *natural* or *resonant frequencies* of the beam (Table 3.1).In Hz units, the resonant frequencies of the beam, f_n, are given by

$$
f_n^2 = \frac{1}{4\pi^2}\Omega_n^4/t_0^2 = \frac{1}{4\pi^2}\frac{EI}{A\rho L^4}\Omega_n^4 \tag{3.33}
$$

The mode shapes of the beam corresponding to each natural frequency are then given by

$$
Y_n(\eta) = -\frac{S(1,\Omega_n)}{T(1,\Omega_n)}T(\eta,\Omega_n) + S(\eta,\Omega_n) \tag{3.34}
$$

where $Y(\eta_m)$ was set to unity since it's just a scaling parameter and has no influence on the mode shape. A very important property of the mode shapes is that they form an *orthogonal* set with respect to a weighting function $p(\eta)$, that is

$$
\int_0^1 d\eta\; p(\eta)Y_n(\eta)Y_m(\eta) = N_n\delta_{nm} \tag{3.35}
$$

with $N_n = \int_0^1 p(x)Y_n^2$. Any vibration can be written as an infinite sum of linear combination of mode shapes (Magrab [2012], Appendix B).

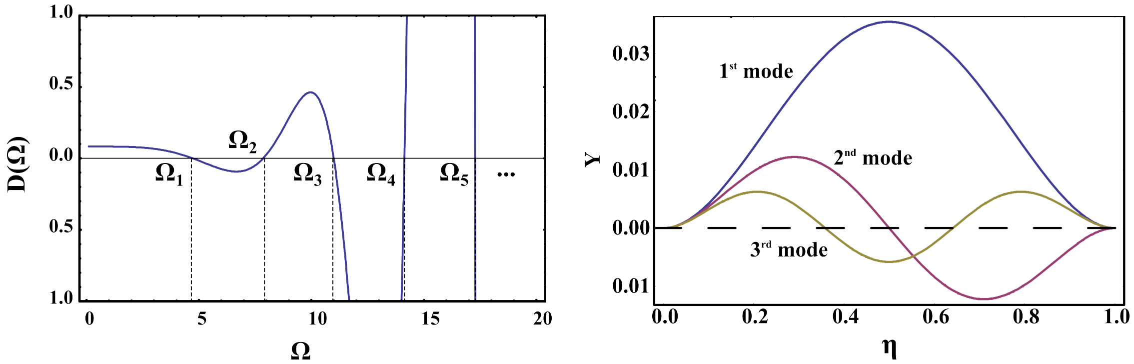

(a) $D(\Omega)$ and the solutions to the characteristic equation (3.32)

(b) First three modes corresponding to the first three solutions of the characteristic equation (3.32)

Figure 3.2: Non-dimensional natural frequencies Ω_n and the corresponding mode shapes.

Effect of the axial stress in the first resonance frequency

To understand the effect of axial stress on the first resonance frequency equation (3.32) is solve for different values of S_0 and first solution (Ω_1) is plotted in Figure 3.3. To fit the data a function of form

$$\Omega_1(S_0) = \Omega_1(0)\left(1 + \alpha S_0^{\beta}\right)^{\chi} \tag{3.36}$$

is used where $\Omega_1(0) \approx 4.73$ is the resonance frequency without any applied axial stress. Figure 3.3 shows good agreement for the coefficients $\alpha = 0.026$ and $\beta = 1$ and $\chi = 0.237$. Using equations (3.23) the resonance frequency as a function of the tensile stress can be approximated by

$$f_0(\sigma) \approx 3.56\frac{1}{L^2}\sqrt{\frac{EI}{wt\rho} + 0.026\frac{L^2}{\rho}\sigma} \qquad \text{[Hz]} \tag{3.37}$$

where $\sigma \equiv p_0/wt$ is the applied axial stress. If the beams is under compressive stress σ should be replaced by $-\sigma$.

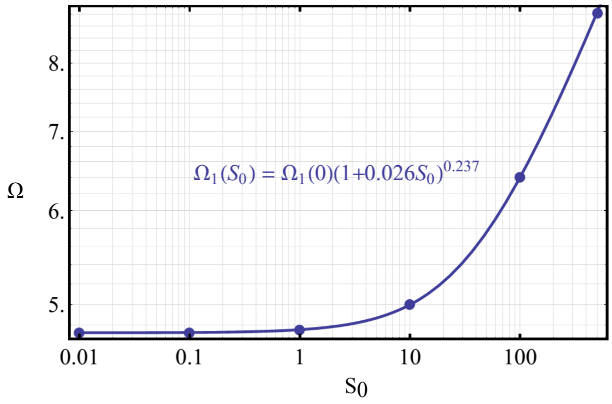

Figure 3.3: Effect of the applied axial stress on the resonance frequency of clamped thin beams.

3.1.3 Static load

The deflection caused by a static load can be evaluated neglecting all time derivatives in the governing equation (3.24). The particular case of a point-force applied at the center of the beam, $\eta_l = 0.5$, for a beam with no in-plane stress is presented here. The governing equation is then written as

$$\frac{\partial^4 y}{\partial \eta^4} = \hat{f}_a(\eta) = \hat{F}_a \delta(\eta - \eta_l) \tag{3.38}$$

where $\hat{F}_a$ is the force magnitude and $\delta(eta)$ is the *delta-Dirac* function (see for example Riley et al. [2006]). Solving equation (3.38) with clamped-clamped boundary conditions (3.25) yields

$$y(\eta) = \hat{F}_a \frac{1}{6} \left((\eta - \eta_l)^3 \theta(\eta - \eta_l) - \eta^2 (\eta_l - 1)^2 \theta(1 - \eta_l)(2\eta\eta_l + \eta - 3\eta_l) \right) \tag{3.39}$$

which has its maximum displacement at $\eta = \eta_l = 0.5$,

$$y_{\text{max}} = y(0.5) = \frac{1}{192} \hat{F}_a \tag{3.40}$$

3.1.4 Harmonic driving

The general solution for a thin plate with constant in-plane stress and a concentrated mass driven by an harmonic force is presented here. For harmonic driving the force and the sought solution have a temporal dependence of the form $e^{j\Omega^2\tau}$. The spatial form of the sought solution is written as the sum of all natural mode shapes $Y_n(\eta)$ times a weighting constant c_n, that is,

$$y(\eta, \tau) = \sum_{n=1}^{\infty} c_n Y_n(\eta) e^{j\Omega^2\tau} \tag{3.41}$$

where the mode shape $Y_n(\eta)$ is given by (3.34) and the driving force is written as

$$\hat{f}_a(\eta, \tau) = \hat{F}_a(\eta) e^{j\Omega^2\tau} \tag{3.42}$$

Here a damping force per unit length, proportional to the transverse velocity of the beam, is also introduce through the external force by writing $\hat{f}_a(\eta, \tau) = \hat{F}_{app}(\eta, \tau) \exp(j\Omega^2\tau) + \hat{f}_d(\eta, \tau)$ where $\hat{f}_{app}$ is the externally applied driving force and $\hat{f}_d(\eta, \tau)$ is the damping force per unit length written in its non-dimensional form as

$$\hat{f}_d(\eta, \tau) = -2\zeta \frac{\partial y}{\partial \tau} \tag{3.43}$$

with $\zeta = cL^4/2t_0EI$ where c is the damping coefficient. The non-dimensional governing equation (3.24) is now written as

$$\frac{\partial^4 y}{\partial \eta^4} - S_0 \frac{\partial^2 y}{\partial \eta^2} + 2\zeta \frac{\partial y}{\partial \tau} + \frac{\partial^2 y}{\partial \tau^2} = \hat{F}_{app}(\eta, \tau) e^{j\Omega^2\tau} \tag{3.44}$$

and using equations (3.41) and (3.26) yields

$$\sum_{n=1}^{\infty} c_n \left[\frac{d^4 Y_n(\eta)}{d\eta^4} - S_0 \frac{\partial^2 Y_n}{\partial \eta^2} + j2\zeta\Omega^2 Y_n(\eta) - \Omega^4 Y_n(\eta) \right] = \hat{F}_{app} \tag{3.45}$$

Multiplying this last equation by $Y_m(\eta)$, integrating from 0 to 1 and using equation (3.28) together with property (3.35) of the orthogonality of the mode shapes, yields

$$c_n = \frac{G_n}{(\Omega_n^4 - \Omega^4) + j2\zeta\Omega^2} \tag{3.46}$$

where

$$G_n = \frac{1}{N_n} \int_0^1 d\eta \, Y_n(\eta) f_{app} \quad \text{with} \quad N_n = \int_0^1 d\eta \, Y_n^2(\eta) \tag{3.47}$$

The factor G_n provides important information about the excitation of mode n for the given applied force f_{app}. It can be thought as a projection of the force shape onto the mode shape. In particular, if the applied force is symmetric, has is the case of an uniform load, and the natural mode is anti-symmetric, has is the case of even modes, the factor G_n will be zero and that mode will not be excited.

Finally, the general solution to harmonic driving is written as

$$y(\eta, \tau) = \sum_{n=1}^{\infty} \frac{G_n}{(\Omega_n^4 - \Omega^4) + j2\zeta\Omega^2} Y_n(\eta) e^{j\Omega^2 \tau} \tag{3.48}$$

The particular case of a point-load harmonic driving is consider here for future reference. A point-load force of magnitude f_a $[\mathrm{N}]$, applied on point x_l, can be represented, in its non-dimensional form, by

$$\hat{f}(\eta) = \hat{F}_a \delta(\eta - \eta_l), \qquad 0 \leq \eta_l \leq 1 \tag{3.49}$$

Substituting f_{app} in equation (3.47) by equation (3.23) a performing the integration immediately yields

$$G_n = \frac{1}{N_n} Y_n(\eta_l) \hat{F}_a \tag{3.50}$$

and, using equation (3.48), the solution for a point-load harmonic driving is written as

$$y(\eta, \tau) = \hat{F}_a \sum_{n=1}^{\infty} \frac{1}{N_n} \frac{Y_n(\eta_l)}{(\Omega_n^4 - \Omega^4) + j2\zeta\Omega^2} Y_n(\eta) e^{j\Omega^2 \tau} \tag{3.51}$$

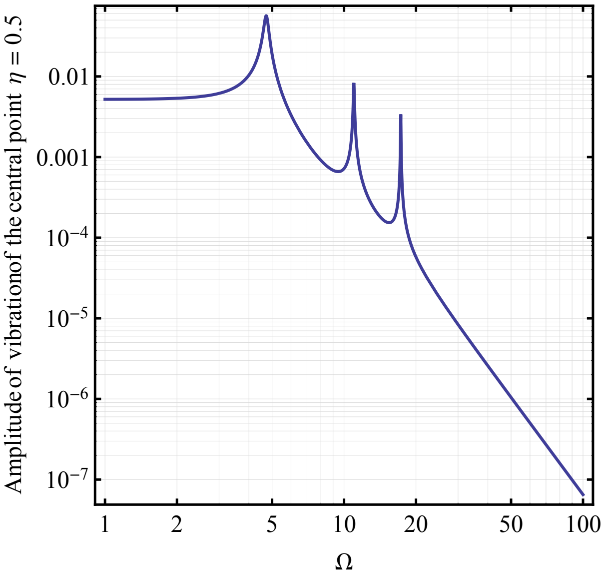

Figure 3.4: Frequency spectrum of the normalized displacement of the central position of a thin beam under a concentrated load at its center.

3.2 Thin Rectangular Plates

Considerer now a thin rectangular plate as exemplified in Figure 3.5. For the following discussion it is assumed that the lateral dimensions of the plate, a and b, are much larger than the thickness of the plate, h, and that the plane stress assumptions holds, that is, the normal stress σ_z and the shear stresses τ_{xz} and τ_{yz} are very small compared to the in-plane stresses σ_x and σ_y and to the in-plane shear stress τ_{xy}. This way, one sets

$$\sigma_z = \tau_{xz} = \tau_{yz} = 0 \tag{3.52}$$

Under the plane-stress assumption the *middle plane* (the plane equidistant from the top and bottom surfaces of a plate with constant thickness) remains unaltered in size, planes perpendicular to it remain perpendicular with their area unchanged and there is no transversal deformation, that is, $\frac{\partial w}{\partial z} = 0$.

Extending the rationale from thin beams a local curvature along the x and y direction are defined as $\kappa_x = \partial^2 w/\partial x^2$ and $\kappa_y = \partial^2 w/\partial y^2$, respectively, and from equations (3.2), (C.15), (3.52) and (C.4) the

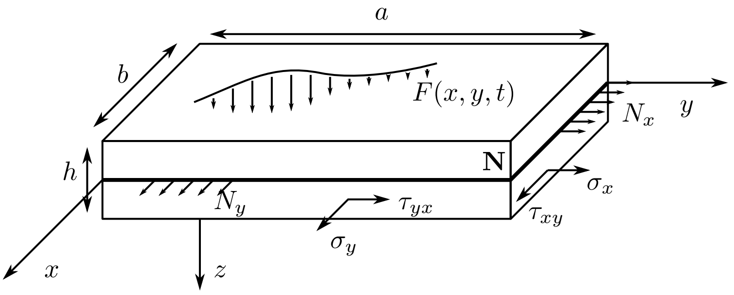

Figure 3.5: Thin rectangular plate example.

strain and stress components are written as

$$\begin{aligned} e_x &= -z\frac{\partial^2 w}{\partial x^2} & \sigma_x &= \frac{E}{1-\nu^2}(\epsilon_x + \nu\epsilon_y) \\ e_y &= -z\frac{\partial^2 w}{\partial x^2} \quad \text{and} & \sigma_y &= \frac{E}{1-\nu^2}(\epsilon_y + \nu\epsilon_x) \\ e_{xy} &= -2z\frac{\partial^2 w}{\partial x \partial y} & \sigma_{xy} &= \frac{E}{2(1+\nu)}\epsilon_{xy} \end{aligned} \tag{3.53}$$

The moments per unit length induced by the distributed normal and shear stress in equations (3.53) can be computed as

$$\begin{aligned} M_x &= \int_{-h/2}^{h/2} \sigma_x z dz = -D\left(\frac{\partial^2 w}{\partial x^2} + \nu\frac{\partial^2 w}{\partial y^2}\right) \\ M_y &= \int_{-h/2}^{h/2} \sigma_y z dz = -D\left(\frac{\partial^2 w}{\partial y^2} + \nu\frac{\partial^2 w}{\partial x^2}\right) \qquad [\mathrm{N}] \\ M_{xy} &= \int_{-h/2}^{h/2} \sigma_{xy} z dz = -D(1-\nu)\frac{\partial^2 w}{\partial x \partial y} \end{aligned} \tag{3.54}$$

where

$$D = \frac{Eh^3}{12(1-\nu^2)} \qquad [\mathrm{N.m}] \tag{3.55}$$

is called the flexural rigidity of the plate.

As in the case of the *Euler-Bernoulli* theory, vertical shear strains are neglect in the *plane-stress* formulation but they must be accounted for to balance the external load. It can be show (see for example Ventsel and Krauthammer [2001] or Timoshenko and Woinowsky-Krieger [1959]) that the *effective vertical shear forces* per unit length along the surface perpendicular to the x and y axis are, respectively,

$$V_x = D\left(\frac{\partial^3 w}{\partial x^3} + (2-\nu)\frac{\partial^3 w}{\partial x \partial y^2}\right) \quad \text{and} \quad V_y = D\left(\frac{\partial^3 w}{\partial y^3} + (2-\nu)\frac{\partial^3 w}{\partial y \partial x^2}\right) \tag{3.56}$$

where ∇^2 is the two dimensional Laplace operator.

The different contributions to the total energy are now presented.

Strain Energy From equations (C.17) and (3.53) the total strain energy is given by

$$\begin{aligned} U &= \frac{E}{2(1-\nu^2)} \iiint_V \left(e_x^2 + e_y^2 + 2\nu e_x e_y + \frac{1-\nu}{2}e_{xy}^2\right) dV \\ &= \frac{D}{2}\iint_A \left[\left(\frac{\partial^2 w}{\partial x^2}\right)^2 + \left(\frac{\partial^2 w}{\partial y^2}\right)^2 + 2\nu\frac{\partial^2 w}{\partial x^2}\frac{\partial^2 w}{\partial y^2} + 2(1-\nu)\left(\frac{\partial^2 w}{\partial y \partial x}\right)^2\right] dA \end{aligned} \tag{3.57}$$

where the integration over z was performed from $-h/2$ to $+h/2$.

Kinetic Energy From equations (C.18) the total kinetic energy is given by

$$T = \frac{1}{2}\iiint_V \rho\left(\frac{\partial w}{\partial t}\right)^2 = \frac{h}{2}\iint_A \rho\left(\frac{\partial w}{\partial t}\right)^2 \tag{3.58}$$

where ρ is the mass density of the material and the integration over z is performed from $-h/2$ to $+h/2$.

External Forces As in the case of thin beams, the external forces are subdivided into in-plane forces and transverse forces. The work done by the transverse forces can be expressed as

$$W_a = \iint_A F_a(x, y, t) w(x, y, t) dA \tag{3.59}$$

where $F_a(x, y, t)$ is the applied pressure distribution.

For the in-plane forces it is assumed that there are two constant and perpendicular forces per unit length —N_x $[N/m]$ which acts parallel to the x axis and N_y $[N/m]$ which acts parallel to the y axis. Following the same rationale behind equation (3.13) the elongations of the neutral plane along the x and y direction are, respectively,

$$\Delta_x \approx \left(\frac{\partial w}{\partial x}\right) dx \quad \text{and} \quad \Delta_y \approx \left(\frac{\partial w}{\partial y}\right) dy \tag{3.60}$$

and the work performed is

$$W_N = -\frac{1}{2} \iint_A \left[N_x \left(\frac{\partial w}{\partial x}\right) + N_y \left(\frac{\partial w}{\partial y}\right)\right] dA \tag{3.61}$$

The total work is then

$$W = W_a + W_N = \iint_A F_a(x, y, t) w(x, y, t) dA - \frac{1}{2} \iint_A \left[N_x \left(\frac{\partial w}{\partial x}\right) + N_y \left(\frac{\partial w}{\partial y}\right)\right] dA \tag{3.62}$$

Boundary attachments The boundary attachments for thin plates can be generalized from the thin beam cases with a translational spring, k, a rotational spring k_t and some mass M with rotational inertia J for each one of the four boundaries. For simplicity sake the general case will not be presented here and at all boundaries the clamped-condition is imposed. For reference these generalized boundary conditions are given in table 3.3. A complete description for very general boundary conditions can be found at Magrab [2012].

3.2.1 Governing equation

From equation (B.2), (B.3), (3.57), (3.58), (3.57) and (3.62) the minimization function can be written as

$$\begin{aligned} F = \frac{D}{2} &\left[\left(\frac{\partial^2 w}{\partial x^2}\right)^2 + \left(\frac{\partial^2 w}{\partial y^2}\right)^2 + 2\nu \frac{\partial^2 w}{\partial x^2} \frac{\partial^2 w}{\partial y^2} + 2(1-\nu)\left(\frac{\partial^2 w}{\partial y \partial x}\right)^2\right] + \frac{h}{2}\rho \left(\frac{\partial w}{\partial t}\right)^2 \\ &- \frac{1}{2}\left[N_x \left(\frac{\partial w}{\partial x}\right)^2 + N_y \left(\frac{\partial w}{\partial y}\right)^2\right] + F_a(x, y, t) w(x, y, t) = 0 \end{aligned} \tag{3.63}$$

and from equation (B.4) the governing equation for a thin plate is

$$D\nabla^4_{xy} w - N_x \frac{\partial^2 w}{\partial x^2} - N_y \frac{\partial^2 w}{\partial y^2} + \rho h \frac{\partial^2 w}{\partial t^2} = F_{ext}(x, y, t) \tag{3.64}$$

where

$$\nabla^4_{xy} = \frac{\partial^4}{\partial x^4} + 2\frac{\partial^4}{\partial x^2 \partial y^2} + \frac{\partial^4}{\partial y^4} \tag{3.65}$$

Boundary Conditions

The clamped condition along all edges is imposed by

$$w(0,y,t) = w(x,0,t) = w(a,y,t) = w(x,b,t) = 0 \tag{3.66}$$

and

$$\frac{\partial w(0,y,t)}{\partial x} = \frac{\partial w(x,0,t)}{\partial y} = \frac{\partial w(a,y,t)}{\partial x} = \frac{\partial w(x,b,t)}{\partial y} = 0 \tag{3.67}$$

3.2.2 Natural frequencies and mode shapes

The case of a square thin plate without any in-span attachment or concentrated masses is presented here. As in the case of thin beams, the following nomenclature is introduced to simplify the algebraic notation

$$\begin{array}{lllll} \hat{w} = \frac{w}{a} & \eta = \frac{x}{a} & \xi = \frac{y}{a} & \tau = \frac{t}{t_p} & t_p^2 = \frac{\rho h a^4}{D}\ [\mathrm{s}^2] \\ \hat{N}_x = \frac{N_x a^2}{D} & \hat{N}_y = \frac{N_y a^2}{D} & \hat{F}_a = \frac{F_a a^3}{D} & \Omega^2 = \omega t_p & \end{array} \tag{3.68}$$

and the governing equation is written in its non-dimensional form as

$$\nabla^4_{\eta\xi}\hat{w} - \hat{N}_x\frac{\partial^2 \hat{w}}{\partial \eta^2} - \hat{N}_y\frac{\partial^2 \hat{w}}{\partial \xi^2} + \frac{\partial^2 \hat{w}}{\partial \tau^2} = \hat{F}_a(\eta,\xi,\tau) \tag{3.69}$$

where

$$\nabla^4_{\eta\xi} = \frac{\partial^4}{\partial \eta^4} + 2\frac{\partial^4}{\partial \eta^2 \partial \xi^2} + \frac{\partial^4}{\partial \xi^4} \tag{3.70}$$

with boundary conditions

$$\hat{w}(0,\xi,\tau) = \hat{w}(\eta,0,\tau) = \hat{w}(1,\xi,\tau) = \hat{w}(\eta,1,\tau) = 0 \tag{3.71}$$

and

$$\frac{\partial \hat{w}(0,\xi,\tau)}{\partial \eta} = \frac{\partial \hat{w}(\eta,0,\tau)}{\partial \xi} = \frac{\partial \hat{w}(1,\xi,\tau)}{\partial \eta} = \frac{\partial \hat{w}(\eta,1,\tau)}{\partial \xi} = 0 \tag{3.72}$$

To calculate the natural mode shapes and frequencies the external force $\hat{F}_a(\eta,\xi,\tau)$ is set to zero in equation (3.69) yielding

$$\nabla^4_{\eta\xi}\hat{w} - \hat{N}_x\frac{\partial^2 \hat{w}}{\partial \eta^2} - \hat{N}_y\frac{\partial^2 \hat{w}}{\partial \xi^2} + \frac{\partial^2 \hat{w}}{\partial \tau^2} = 0 \tag{3.73}$$

Contrary to the case of thin beams under the Euler-Bernoulli theory, it is not possible, in general, to obtain an analytical solution for the mode shapes of thin plates. Here a numerical solution is derived from the *Rayleigh-Ritz method* applied to the case of an all-clamped square membrane. This method consist in minimizing a function Φ given by the difference between the maximum kinetic energy and the maximum strain energy, namely,

$$\Phi = T_{max} - U_{max} \tag{3.74}$$

For an harmonic vibration of the form $\hat{w}(\eta,\xi,\tau) = \hat{W}(\eta,\xi)\exp(j\Omega^2\tau)$ the maximum kinetic and strain energy is obtained by setting $\hat{w}(\eta,\tau)$ and $\partial\hat{w}(\eta,\tau)/\partial\tau$ to their maximum, absolute, values — $|\hat{W}(\eta,\xi)|$

and $\Omega^2|\hat{W}(\eta,\xi)|$, respectively. From equations (C.18), (3.57) and (3.68) the maximum kinetic and strain energy are given by

$$\begin{aligned}T_{max} &= \Omega^4\frac{h}{2}\iint_A \rho\hat{W}(\eta,\xi)dA\\ U_{max} &= \frac{D}{2}\iint_A\left[\left(\frac{\partial^2\hat{W}}{\partial\eta^2}\right)^2+\left(\frac{\partial^2\hat{W}}{\partial\xi^2}\right)^2+2\nu\frac{\partial^4\hat{W}}{\partial\eta^2\partial\xi^2}+2(1-\nu)\left(\frac{\partial^2\hat{W}}{\partial\eta\partial\xi}\right)^2\right]dA\end{aligned} \tag{3.75}$$

The solution $\hat{W}(\eta,\tau)$ is assumed to be decomposable by separation of variables, with general form (Young D [1950])

$$\hat{W}(\eta,\xi)=\sum_{n}^{N}\sum_{m}^{N}A_{nm}X_n(\eta)Y_m(\xi) \tag{3.76}$$

where $X_n(\eta)$ and $Y_m(\xi)$ are trail functions given by (3.34). The minimization of Φ is then obtained by substituting equation (3.76) into equations (3.75) and finding the values of Ω that verify

$$\frac{\partial\Phi}{\partial A_{lk}}=0 \tag{3.77}$$

After performing these operations the problem is reduced to the standard eigenvalue problem yields the N^2 natural frequencies corresponding to the N^2 natural modes, namely,

$$[A_{nm}][C_{nmlk}]-\Omega^4\{A_{nm}\}[B_{nmlk}]=0 \tag{3.78}$$

where the general form of Φ and components of the matrices A_{nm}, B_{nmlk} and C_{nmlk} are given in Appendix D. The mode shape $\hat{W}_j$, corresponding to the natural frequency Ω_j is then given by equation (3.76)

$$\hat{W}_j(\eta,\xi)=\sum_{n}^{N}\sum_{m}^{N}A_{mn}^{(j)}X_n(\eta)Y_m(\xi) \tag{3.79}$$

where $A_{mn}^{(j)}$ is the modal vector correspondent to the natural frequency Ω_j. The complete procedure can be found at (Magrab [2012], Chapter 6).The first four natural modes are depicted in figure (3.6) with natural frequencies

$$\Omega_j=\begin{cases}5.9992 & j=1\\ 8.5688 & j=2,\ j=3\\ 10.411 & j=4\end{cases} \tag{3.80}$$

It follows from definition (3.76) and the orthogonality property (3.35) that the natural modes $\{\hat{W}_j\}$ form an orthogonal set, namely,

$$\int_0^1 d\eta\int_0^1 d\xi\ \hat{W}_j\hat{W}_{j'}=\delta_{jj'} \tag{3.81}$$

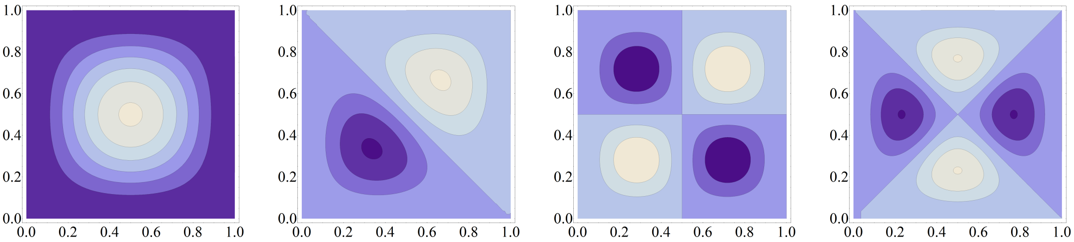

(a) First resonance mode, $\Omega_1^2 = 35.9899$.
(b) Second resonance mode with degenerancy 2, $\Omega_2^2 = \Omega_3^2 = 73.4238$.
(c) Third resonance mode, $\Omega_4^2 = 108.382$.
(d) Fourth resonance mode, $\Omega_5^2 = 131.635$.

Figure 3.6: First resonance modes for a square clamped plate without in-plane forces or concentrated masses.

3.2.3 Harmonic driving

Proceeding as in the case of thin beams, it is assumed that the solution as harmonic temporal dependence $\exp(j\Omega^2\tau)$, where Ω is the frequency at which the force $\hat{f}$ is driving the plate. The spatial form of the solution is written as liner combinations of the natural modes with general form

$$\hat{w}(\eta,\xi,\tau) = \sum_{j=0}^{\infty} a_j \hat{W}_j(\eta,\xi)\exp(j\Omega^2\tau) \tag{3.82}$$

A damping pressure, proportional to the transversal velocity of the plate, is introduced through $\hat{f}(\eta,\xi,\tau)$ by writing $\hat{f}(\eta,\xi,\tau) = \hat{F}_a(\eta,\xi,\tau)\exp(j\Omega^2\tau) + \hat{f}_d(\eta,\xi,\tau)$ where $\hat{F}_a$ is the magnitude of the externally applied load driving the plate and $\hat{f}_d$ is the damping pressure written as

$$\hat{f}_d = 2\frac{ca^4}{D}\frac{\partial w}{\partial t} = 2\zeta\frac{\partial \hat{w}}{\partial \tau} \tag{3.83}$$

with $\zeta = ca^4/D$, where c in the damping coefficient. Substituting equations (3.82) into (3.69) yields

$$\sum_j^{\infty} a_j\left[\nabla_{\eta\xi}^4\hat{W}_j - \hat{N}_x\frac{\partial^2 W_j}{\partial\eta^2} - \hat{N}_y\frac{\partial^2\hat{W}_j}{\partial\xi^2} + j2\zeta\Omega^2\hat{W}_j - \Omega^4\hat{W}_j\right] = \hat{F}_a(\eta,\xi,\tau) \tag{3.84}$$

Using equation (3.73) with $\Omega = \Omega_n$, multiplying both sides by $W_{j'}$ and using the orthogonality property of the mode shapes, yields

$$a_j = \frac{G_j}{(\Omega_j^4 - \Omega^4) + j2\zeta\Omega^2} \tag{3.85}$$

and

$$\hat{w}(\eta,\xi,\tau) = \sum_{j=1}^{\infty}\frac{G_j}{(\Omega_j^4 - \Omega^4) + j2\zeta\Omega^2}\hat{W}_j\exp(j\Omega^2\tau) \tag{3.86}$$

with

$$G_j = \frac{1}{N_j}\int_0^1 d\eta\int_0^1 d\xi\ \hat{F}_a(\eta,\xi)\hat{W}_j(\eta,\xi) \quad \text{and} \quad N_j = \int_0^1 d\eta\int_0^1 d\xi\ W_j^2(\eta,\xi) \tag{3.87}$$

Similar to expression (3.48) for thin beams, the factor G_j gives information about the strength at which each mode is excited.

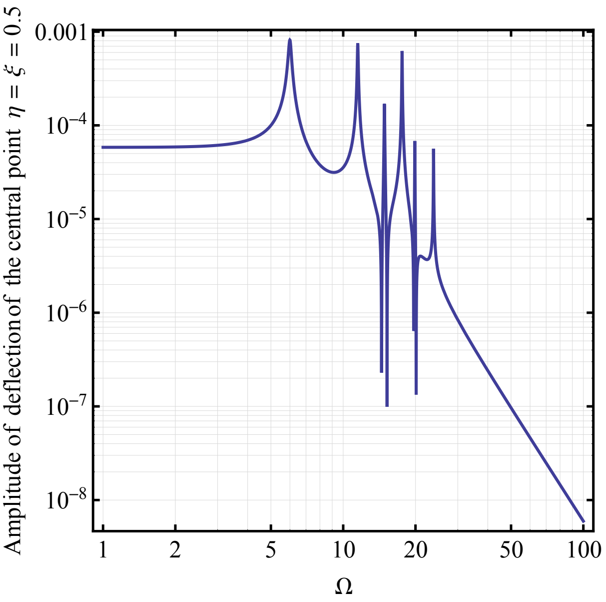

Figure 3.7: Normalized frequency spectrum for the normalized central deflection of a clamped square plate

3.2.4 Static loading

In keeping with the previous developed framework, a static load can be considered from the DC limit of harmonic driving. This way, from equation (3.86) one may write

$$\hat{w}(\eta,\xi) = \lim_{\Omega\to 0} \hat{w}(\eta,\xi,\tau) = \sum_{j=1}^{\infty} \frac{G_j}{\Omega_j^4}\hat{W}_j \tag{3.88}$$

which is simply the sum of all modes with a weighting factor G_j/Ω_j^4.

3.3 Thin Circular plates

Consider now a thin circular plate with radius a, thickness h, Young's modulus E and Poisson ration ν, actuated by a transversal force $f_a(x,y,t)$ (Figure 3.8). The thickness of the plate is much smaller than its radius and the plane stress assumption holds. To deal with a circular geometry it is convenient to first express the previously described formalism in polar coordinates. This is achieved by the following transformations (Magrab [2012], Chapter 6)

$$\begin{array}{lll} x = 0 \to r = 0 & \dfrac{\partial}{\partial x} \to \dfrac{\partial}{\partial r} \qquad \dfrac{\partial}{\partial y} \to \dfrac{\partial}{r\partial\theta} & \dfrac{\partial^2}{\partial x^2} \to \dfrac{\partial^2}{\partial r^2} \\ x = a \to r = a & \dfrac{\partial^2}{\partial y^2} \to \dfrac{\partial}{r\partial r} + \dfrac{\partial^2}{r^2\partial\theta^2} & \dfrac{\partial^2}{\partial x\partial y} \to \dfrac{\partial^2}{r\partial r\partial\theta} - \dfrac{\partial}{r^2\partial\theta} \end{array} \tag{3.89}$$

It is assumed that only axial stress is present with $N_x = N_y = N_r$ and no concentrated mass is present.

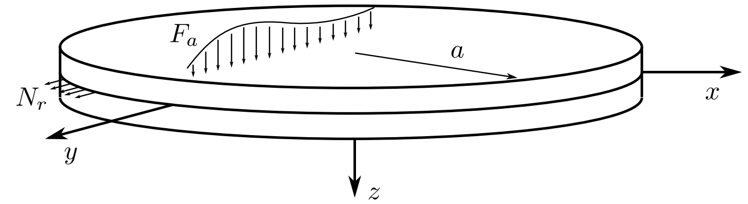

Figure 3.8: Thin circular plate example.

3.3.1 Governing equation

Because the governing equation must be valid in any coordinate system, equation (3.64) can be directly re-written using equations (3.89), yielding

$$D\nabla^4_{r\theta}w_r - N_r\nabla^2_{r\theta}w_r + \rho h\frac{\partial^2 w_r}{\partial t^2} = f_a(r,\theta,t) \tag{3.90}$$

where $w_r = w_r(r,\theta,t)$ is the transversal displacement of the plate and

$$\nabla^2_{r\theta} = \frac{\partial^2}{\partial r^2} + \frac{\partial}{r\partial r} + \frac{\partial^2}{r^2\partial\theta^2} \quad \text{and} \quad \nabla^4_{r\theta}(w_r) = \nabla^2_{r\theta}\left(\nabla^2_{r\theta}(w_r)\right) \tag{3.91}$$

The moment, M_r and vertical shear force, V_r, across the plate are given by

$$M_r(r,\theta,t) = -D\left(\frac{\partial^2 w_r}{\partial r^2} + \nu\left(\frac{\partial w_r}{r\partial r} + \frac{\partial^2}{r^2\partial\theta^2}\right)\right) \tag{3.92}$$

and

$$V_r(r,\theta,t) = D\left(\frac{\partial}{\partial r}\left(\nabla^2_{r\theta}w_r\right) + (1-\nu)\left(\frac{\partial^3 w_r}{r^2\partial\partial\theta^2} - \frac{\partial^2 w_r}{r^3\partial\theta^2}\right)\right) \tag{3.93}$$

Boundary conditions

The boundary conditions for a clamped circular membrane are

$$w_r(a,\theta,t) = 0 \quad \text{and} \quad \left.\frac{\partial w_r}{\partial r}\right|_{r=a} = 0 \tag{3.94}$$

and at the center, $r = 0$, it is imposed that the displacement remains finite.

3.3.2 Natural frequencies and mode shapes

In the interest of brevity, only the final equation for the natural mode shape, frequencies and characteristic equation are presented. The complete derivation can be found in Magrab [2012].

The characteristic equation of a clamped circular thin plate with constant in-plane stress and no in-span attachments is given by

$$\frac{\delta}{2}J_n(\epsilon)(I_{n-1}(\delta) + I_{n+1}(\delta)) - \frac{\epsilon}{2}I_n(\delta)(J_{n-1}(\epsilon) - J_{n+1}(\epsilon)) = 0 \tag{3.95}$$

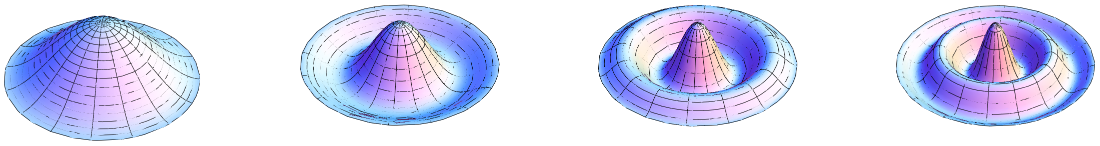

(a) (b) (c) (d)

Figure 3.9: First 4 axial symmetric natural mode shapes for a clamped circular plate with no concentrated mass nor axial stress

with the corresponding natural frequencies,

$$\Omega_{0m} = \pi \begin{cases} 1.0174 & m = 1 \\ 2.0074 & m = 2 \\ 3.0046 & m = 3 \\ 4.0034 & m = 4 \end{cases} \tag{3.96}$$

and $\Omega_{0m} \approx \pi\, m$ for $m > 4$. The natural mode shapes are given by

$$W_{nm} = \hat{R}_{nm}(\hat{r})\cos(n\theta) \quad 0 \leq \hat{r} \leq 1 \quad n = 0, 1, 2, \ldots \quad m = 1, 2, \ldots \tag{3.97}$$

Figure 3.9 shows the first four axisymmetric natural modes for clamped circular plates.

Effect of the axial stress in the first resonance frequency

Proceeding analogously to the case of thin beams, the values of the first resonance frequency are plotted against $\hat{N}_r$ in Figure 3.10. Equation (3.36) shows good agreement for the values $\alpha = 0.076$, $\beta = 0.91$ and $\chi = 0.27$ and the resonance frequency is approximated by

$$f_0(\sigma_r) = 1.63\sqrt{\frac{D}{\rho t a 4}}\left(1 + 0.076\left(\frac{ta^2}{D}\sigma\right)^{0.91}\right)^{0.55} \tag{3.98}$$

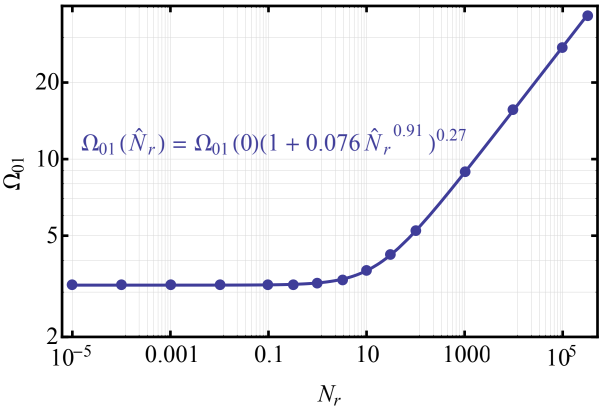

Figure 3.10: Effect of the applied axial stress on the resonance frequency of clamped thin beams.

3.3.3 Harmonic driving

For the sake of simplicity the discussion is restricted to the case of axial symmetric solution, that is, independent of θ. Analogously to the case of rectangular plates, the excitation force is assumed to be of the form

$$\hat{f}_a(\hat{r}, \tau) = \hat{F}_a(\hat{r}) \exp(j\Omega^2 \tau) \tag{3.99}$$

and the solution is written as the sum of all natural modes (3.97) for the case $n = 0$, that is,

$$\hat{w}(\hat{r}, \tau) = \sum_{m=0}^{\infty} a_{0m} \hat{R}_{0m}(\hat{r}) \exp(j\Omega^2 \tau) \tag{3.100}$$

Here a damping force with the same form as (3.83) is also introduce and proceeding analogously to the case of rectangular plates the solution is written as

$$\hat{w}(\hat{r}, \tau) = \sum_{m=1}^{\infty} \frac{G_{0m}}{(\Omega_{0m}^4 - \Omega^4) + j2\zeta\Omega^2} \hat{R}_{0m} \exp(j\Omega^2 \tau) \tag{3.101}$$

with

$$G_{0m} = \frac{1}{N_{0m}} \int_0^1 d\hat{r} \hat{F}_a(\hat{r}) \hat{R}_{0m}(\hat{r}) \quad \text{and} \quad N_{0m} = \int_0^1 d\hat{r}\ R_{0m}^2(\hat{r}) \tag{3.102}$$

3.3.4 Uniform static loading

For the general case where axial stress is present the same method employed for the case of square membranes can be used. Proceeding analogously, from equation (3.101) comes

$$\hat{w}(\hat{r}) = \lim_{\Omega \to 0} \hat{w}(\hat{r}, \theta, \tau) = \sum_{m=1}^{\infty} \frac{G_{0m}}{\Omega_{0m}^4} \hat{R}_{0m} \tag{3.103}$$

For the particular case where axial stress can be neglected one may write

$$\nabla_{\hat{r}}^4 \hat{w}(\hat{r}) = \hat{f}_0 \tag{3.104}$$

Note that because the loading is uniform, and therefore axisymmetric, all derivatives with respect to θ are discarded. This equation can be integrated directly yielding

$$\hat{w}(\hat{r}) = \frac{\hat{f}_0}{64}(1 - \hat{r}^2)^2 \tag{3.105}$$

3.4 The One-Degree-of-Freedom approximation

The membrane-gate system can then thought as an ideal parallel plate capacitor with capacitance $C = \epsilon A/g$, where A is the area of the membrane, ϵ is the permittivity of air and g is the air gap height. When a potential difference, V, is applied across the plates an electrostatic pressure, P_{el}, appears, with

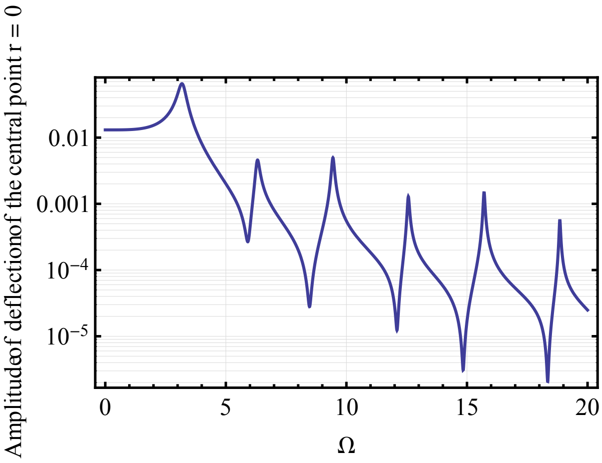

Figure 3.11: Normalized frequency spectrum for the normalized central deflection of a clamped circular plate

magnitude given by (Griffiths [2012])

$$P_{el} = \epsilon \frac{V^2}{2(g_0 - x)^2} \qquad [N/m^2] \tag{3.106}$$

At any given time the charge on the plates is always equal and opposite so that they always attract each other.

3.4.1 The equation of motion

For frequencies below the first natural frequency (and around it) the system can be modelled as spring-mass system with natural frequency ω_0, elastic constant k_e, effective mass m_0, damping coefficient c_d and electrostatic force F_{el} (see for example Bao [2005]). The equation of motion of such system is written as

$$m_0\ddot{x} + c_d\dot{x} + k_e x = F_{el}(t) \tag{3.107}$$

The different contributions to the equation of motion are now derived. Figure 3.13 illustrates the nomenclature used in the following sections.

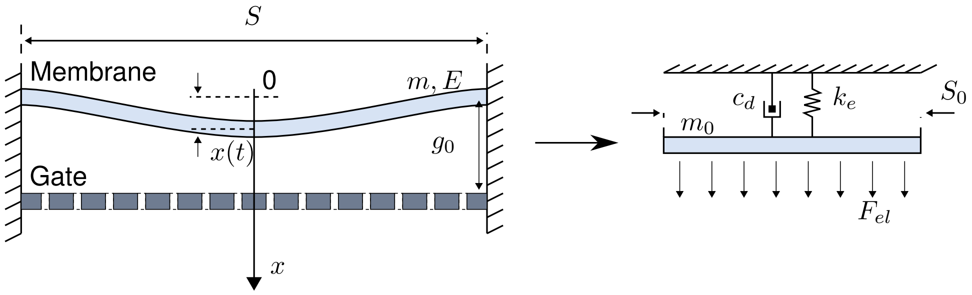

Figure 3.12: One-degree-of-freedom (odf) approximation. The membrane with mass m, Young's modulus E and area S is converted into a mass-spring system with effective mass m_0, elastic constant k_e and an effective area S_0. The electrostatic and damping force geometry dependency is included on the elastic constant and damping coefficient, respectively.

Natural frequency

The natural frequency of a spring-mass system must match the first resonance frequency of the membrane. For square plates, using equation (3.80) for the first mode (Ω_1) immediately yields

$$f_0^{\square} = \frac{1}{2\pi}\omega_0 = \frac{1}{2\pi}\Omega_{00}^2\sqrt{\frac{D}{\rho_{\text{Si}}ta^4}} \approx 5.72797\sqrt{\frac{D}{\rho_{\text{Si}}ta^4}} \qquad [\text{Hz}] \tag{3.108}$$

For circular membranes equation (3.96) must be used instead yielding

$$f_0^{\circ} = 1.6259\sqrt{\frac{D}{\rho_{\text{Si}}ta^4}} \tag{3.109}$$

For the case of the suspended square the effective elastic constant and the total effective mass is first computed (see bellow) and the natural frequency is extracted from (3.115), namely,

$$f_0^{\text{eff}} = \frac{1}{2\pi}\omega_0 = \frac{1}{2\pi}\sqrt{\frac{k_0^{\text{eff}}}{m_T}} = 4.411\sqrt{\frac{EI}{L_b^3\rho t(1.5344wL_b + a^2)}} \tag{3.110}$$

For every case the effect of axial stress is neglected.

Elastic constant

The elastic constant is determined by calculating the maximum displacement for the case of static loading. For square membranes, equation (3.88) must be evaluated numerically. Taking as the basis the first 25 natural modes the calculated spring constant is

$$k_0^{\square} = \frac{P_eS}{\delta_{\text{max0}}} \approx 787.402\frac{D}{a^2} \qquad [\text{N/m}] \tag{3.111}$$

where $\delta_{\text{max0}} = w(r = 0)$ is the maximum displacement of the membrane.
For circular membranes equation (3.105) is used instead yielding

$$k_0^{\circ} = \frac{P_eS}{\delta_{\text{max0}}} = 64\pi\frac{D}{a^2} \tag{3.112}$$

For the suspended square it is assumed that the plate doesn't deform and the stiffness is dominated by the thin beams. For a single tether, the resulting elastic constant for a point-load at its centre can be derived from equation (3.39), namely,

$$k_0^{\text{beam}} = \frac{F}{\delta_{\text{max0}}} = \frac{192EI}{L^3} \tag{3.113}$$

where $\delta_{\text{max0}} = w(x = L/2)$ and F is the magnitude of the applied force. Because all four tethers share the same displacement the effective elastic constant is simply the sum of all four elastic constants, namely,

$$k_0^{\text{eff}} = 4k_0^{\text{beam}} = \frac{768EI}{L^3} \tag{3.114}$$

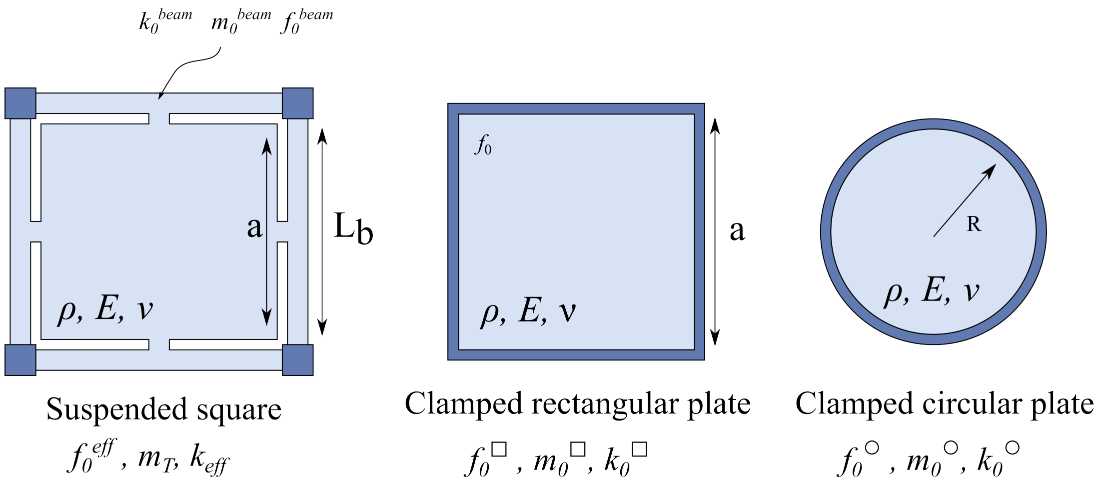

Suspended square f_0^{eff}, m_T, k_{eff}

Clamped rectangular plate $f_0^{\square}$, $m_0^{\square}$, $k_0^{\square}$

Clamped circular plate f_0°, m_0°, k_0°

Figure 3.13: Geometry nomenclature.

Effective mass

The effective mass can be immediately calculated from the well known relation

$$m_0 = \frac{k_e}{\omega_0^2} \qquad [\text{kg}] \tag{3.115}$$

For the case of square membranes this yields

$$m_0^{\square} = 0.607904\ \rho t a^2 \tag{3.116}$$

For the circular membranes

$$m_0^{\circ} = 0.613243\ \rho t \pi R^2 \tag{3.117}$$

For the suspended square, the first natural frequency for a single beam is given by equation (3.33) for $\Omega_n = \Omega_1$ and the effective mass is

$$m_0^{\text{beam}} = 0.3836\ \rho A L \tag{3.118}$$

The total effective mass is then the sum of all four beams plus the suspended square,

$$m_T = 4m_0^{\text{beam}} + m_{\text{square}} = \rho t(1.5344 w L_b + a^2) \tag{3.119}$$

Damping coefficient

There are several types on damping originating from different phenomena. They can be divided into *intrinsic damping* and *extrinsic damping*. The former relates to the energy dissipation from the material itself such as structural damping, thermoelastic damping (TED), phonon-phonon damping, etc (see for example Cleland [2003], Chapter 8). The latter encompasses energy dissipation to the external media such as air damping, viscous fluid damping or squeeze film damping (see for example Magrab [2012], Chapter 4). Here all forms of damping are ignored with the exception of squeeze-film damping which is the dominant form of dissipation (Pratap et al. [2007])

Squeeze-film damping arises from the constrain imposed to air flow when the membrane is pulled against the gate or pushed away from it. Depending on the geometry the damping effect can have a dissipative component, proportional to the velocity of the membrane, and an elastic component, proportional to the displacement of the membrane, which comes from the compression of trapped air. Usually this compression of air is undesirable since it greatly increases the overall stiffness of the system decreasing the maximum possible deflection of the membrane and shifting the resonance frequency.

The value of the damping coefficient, c_d, depends on the geometry of the problem and it is not possible, in general, to provide an analytical solution. Here the basic principles of squeeze film damping are introduced together with a simple model.

Squeeze-film models are based on solutions of the *Reynolds equation*. The general form of the non-linear Reynolds equation for compressible gas between two parallel surfaces moving perpendicularly to each other is given by (Gross et al. [1980])

$$\frac{\partial}{\partial x}\left(\rho\frac{h^3}{\mu}\frac{\partial P}{\partial x}\right)+\frac{\partial}{\partial y}\left(\rho\frac{h^3}{\mu}\frac{\partial P}{\partial y}\right)=12\frac{\partial(h\rho)}{\partial t} \tag{3.120}$$

where ρ is the density of the air, $h(x, y)$ is the separation of the plates, μ is the coefficient of viscosity and $P(x, y)$ is the total pressure between the plates. Under isothermal conditions, the pressure is proportional to density of the air and one may write

$$\frac{\partial}{\partial x}\left(P\frac{h^3}{\mu}\frac{\partial P}{\partial x}\right)+\frac{\partial}{\partial y}\left(P\frac{h^3}{\mu}\frac{\partial P}{\partial y}\right)=12\frac{\partial(hP)}{\partial t} \tag{3.121}$$

Assuming that the membrane moves rigidly against the gate[1] with amplitude much smaller than the air gap height, that is, $h = h_0 + \delta h(t)$, with $\delta h \ll h_0$, and that the pressure variation, p, is much smaller than the atmospheric pressure, P_a, that is, $P(x, y, t) = P_a + p(x, y, t)$, with $p \ll P_a$, the Reynolds equation is further simplified to

$$P_a\nabla^2 p-\frac{12\mu}{{h_0}^2}\frac{\partial p}{\partial t}=\frac{12\mu P_a}{{h_0}^3}\frac{dh}{dt} \tag{3.122}$$

where ∇^2 is the 2-dimensional Laplacian operator. Introducing the normalized variables, $\tilde{x} = x/a$, $\tilde{y} = y/a$, $\tilde{h} = \delta h/g_0$, $\tilde{p} = p/P_a$ and $\tau = \omega\tau$ and substituting them into the above equation yields the non-dimensional, linearized Reynolds equation for compressible films

$$\nabla^2\tilde{p}-\sigma\frac{\partial\tilde{p}}{\partial\tau}=\sigma\frac{d\tilde{h}}{d\tau} \tag{3.123}$$

where ω is the frequency at which the membrane is being driven (see bellow) and

$$\sigma=\frac{12\mu\omega a^4}{P_a {g_0}^2} \tag{3.124}$$

is the *squeeze-film number*, which plays an important role in the designing of MEMS. If $\sigma > 1$ compression of the air film must be taken into consideration. If $\sigma \ll 1$ compression of the film can be ignored. For

---

[1] This will overestimate the damping coefficient but it is justified bellow

the latter case, the second term in the LHS of equation (3.123) can be neglected and the film is deemed *incompressible*.

When dealing with a perforated structure it is common to divided the whole structure into single *perforation cells* (see figure 3.14). There are different geometries that can be adopted, one of which is the rectangular geometry with an uniform grid. The perforation cell is then approximated to an annulus plate with inner radius r_0 and outer radius r_c. The outer radius is determined by imposing conservation of area —if the area of a single cell is A then $\pi r_c^2 = A$, which yields for this case $r_c = \frac{a_c}{\sqrt{\pi}}$. Bao et al. proposed a modified non-linear Reynolds equation to account for the flow of air in long perforated structures (Bao [2005], Bao and Yang [2007]),

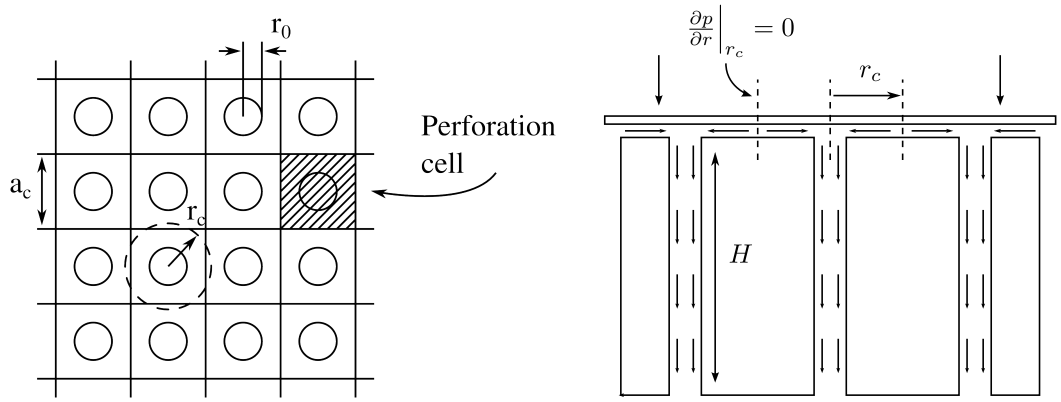

(a)

(b)

Figure 3.14: (a) Concept of a perforation cell and (b) 2-dimensional flow model.

$$\frac{\partial}{\partial x}\left(P\frac{\partial P}{\partial x}\right) + \frac{\partial}{\partial y}\left(P\frac{\partial P}{\partial y}\right) - P\frac{3\eta^2 r_0^2}{2{g_0}^2 H}\frac{p}{\Pi(\eta)} = \frac{12\mu}{{g_0}^3}\frac{\partial(Ph)}{\partial t} \tag{3.125}$$

where $P = P_a + p$, H is the thickness of the perforation, $\eta = r_0/r_c$ and

$$\Pi(\eta) = 1 + 3{r_0}^4/16H{g_0}^3 k(\eta) \quad \text{with} \quad k(\eta) = 4\eta^2 - \eta^4 - 4\ln\eta - 3 \tag{3.126}$$

Applying the same principles described above for small vibration amplitude and small pressure variation, equation (3.125) reduces to

$$\nabla^2 p - \frac{3\eta^2 {r_0}^2}{2{g_0}^3 H}\frac{1}{\Pi(\eta)}p = \frac{12\mu}{{g_0}^3}\frac{\partial h}{\partial t} \tag{3.127}$$

This model is adequate for high aspect-ratio structure with narrow perforation radius, small air gap height and long perforation length (Pratap et al. [2007]).

Bao et al. [2003] solved the modified Reynolds equation for ideal vented conditions ($p = 0$ in all boundaries) extracting the damping coefficient

$$c_d = \gamma\frac{\mu a^4}{{g_0}^3} \tag{3.128}$$

with

$$\gamma = 3\alpha^2 - 6\alpha^3\frac{\sinh^2 1/\alpha}{\sinh 2/\alpha} - \frac{24\alpha^3}{\pi^2}\sum_{n=1,3,5,\ldots}^{\infty}\frac{\tanh\frac{\sqrt{1+(n\pi\alpha/2)^2}}{\alpha}}{n^2(1+(n\pi\alpha/2)^2)^3/2} \tag{3.129}$$

where $\alpha = l/a$ and $l = \sqrt{\frac{3{g_0}^3 H\Pi(\eta)}{3\eta^2 {r_0}^2}}$ called the *attenuation length*.

For the suspended square geometry these conditions apply but for the clamped geometry this is no longer true. Nonetheless equation (3.128) can be used for a first design approach and grasping of fundamental concepts in squeeze film damping of high density perforated geometries.

Electrostatic loading

The actuation signal can always be decomposed into a static component plus its sinusoidal components. Consider here that the driving voltage is composed of a bias voltage V_{DC} plus an harmonic component $V_{AC}\cos(\omega t)$, where the phase is set to zero by choice. Replacing $V = V_{DC} + V_{AC}\cos(\omega t)$ in equation (3.106) yields

$$F_{el} = \frac{\epsilon A}{2(g_0 - x)^2}(V_{DC}^2 + \frac{1}{2}V_{AC}^2 + 2V_{DC}V_{AC}\cos(\omega t) + \frac{1}{2}V_{AC}^2\cos(2\omega t)) \tag{3.130}$$

The first two terms will force the membrane to a new equilibrium position and the last two terms contribute to the harmonic driving, the first at the fundamental frequency f and the second at the first harmonic $2f$. This harmonic is to be suppressed by a convenient choice of the DC bias and input signal amplitude (see discussion bellow) and it is therefore ignored in the following discussion. The electrostatic force is therefore written as

$$F_{el} = \frac{\epsilon A}{2(g_0 - x)^2}(V_{DC}^2 + \frac{1}{2}V_{AC}^2 + 2V_{DC}V_{AC}\cos(\omega t)) \tag{3.131}$$

3.4.2 Solution to the equation of motion

Due to the non-linear spacial dependence of the electrostatic force, the complete solution must be attained, in general, by numerical methods. However, for small displacement compared to air gap height, equation (3.131) can linearized using a Taylor's series expansion. The solution is separated into a static equilibrium displacement, x_0, plus an harmonic component at the fundamental frequency with amplitude $\delta \ll x_0$, namely,

$$x(t) = x_0 + x_\omega(t) = x_0 + \delta\cos(\omega t + \phi) \tag{3.132}$$

The equilibrium position is obtained by solving equation the equation of motion (3.107) neglecting all time derivatives and considering only the first two terms of the electrostatic expansion (3.131),

$$\omega_0^2 x_0 = \frac{\epsilon A}{2m_0(g_0 - x_0)^2}(V_{DC}^2 + \frac{1}{2}V_{AC}^2) \tag{3.133}$$

where the approximation $g_0 + x(t) \approx g_0 + x_0$ was used. Figure 5.6 (a) illustrates the solutions to equation (3.133). Only one has physical meaning (see discussion bellow) which has the general form

$$x_0(V_{DC}) = g_0\frac{1}{3}\left(2 - f(V_{DC}^2) - \frac{1}{f(V_{DC}^2)}\right) \tag{3.134}$$

with

$$f(v) = \left[\frac{1}{2}\left(2 - 27ev + \sqrt{(2-27ev)^2 - 4}\right)\right]^{1/3} \tag{3.135}$$

where $e = \epsilon A / 2m_0\omega_0^2 g_0^3$. This equilibrium position is used to define a new air gap height,

$$g_0' \equiv g_0 - x_0 \tag{3.136}$$

which is commonly refered to as the *membrane's operating point*. The amplitude of vibration is now obtained by solving the equation of motion for the harmonic component of the electrostatic loading at the membrane's operating point, that is,

$$\ddot{x_\omega}(t) + \beta\dot{x_\omega}(t) + \omega_0^2 x_\omega(t) = \frac{\epsilon A}{m_0(g_0' - x_\omega(t))^2} V_{DC}V_{AC}\cos(\omega t) \tag{3.137}$$

To linearize equation (3.137) the term $1/(g_0' - x_\omega(t))^2$ in the RHS is expand around g_0' using a Taylor series and terms of second order or higher are ignored, yielding

$$\ddot{x_\omega}(t) + \beta\dot{x_\omega}(t) + \omega_0^2 x_\omega(t) \approx \frac{\epsilon A}{m_0 g_0'^2}\left(1 + \frac{2}{g_0'}x_\omega(t)\right) V_{DC}V_{AC}\cos(\omega t) \tag{3.138}$$

which can be viewed as an harmonic driving force

$$F^\omega(t) = \frac{\epsilon A}{g_0'^2} V_{DC}V_{AC}\cos(\omega t) \tag{3.139}$$

plus an *electrostatic elastic force*

$$F_{\text{spring}}(t) = \frac{\epsilon A}{g_0'^3} V_{DC}V_{AC}\cos(\omega t)\; x_\omega(t) \tag{3.140}$$

From equation 3.140 an *electrostatic elastic constant* is defined by

$$k_{el} \equiv \left(\frac{\partial F_{\text{spring}}}{\partial x_\omega}\right)_{\text{RMS}} = \frac{\epsilon A}{g_0'^3}\frac{V_{DC}V_{AC}}{\sqrt{2}} \tag{3.141}$$

The equation of motion is now rewritten as

$$\ddot{x}_\omega + \beta\dot{x}_\omega + \omega_0'^2 x_\omega = F^\omega / m_0 \tag{3.142}$$

with $\omega_0'^2 = (k_e - k_{el})/m_0$. Writing $x_\omega(t) = \text{Re}[\delta\exp(j(\omega t + \phi))]$ and substituting into equation (3.142) immediately yields

$$x_\omega(t) = \frac{\epsilon A}{m_0 g_0'^2}\frac{V_{DC}V_{AC}}{\sqrt{(\omega_0'^2 - \omega^2)^2 + \beta^2\omega^2}}\cos(\omega t + \phi) \tag{3.143}$$

with

$$\phi = -\arctan\frac{\beta\omega}{\omega_0^2 - \omega^2} \tag{3.144}$$

3.5 Conclusion

The basic theoretical elements for modelling and designing thin beams and thin rectangular and circular plates are presented here. The formalism for very general boundary conditions with in-plane axial stress is presented together. The particular cases of relevance to this work are further developed throughout the text. Finally, a summary of the these results is portrayed in tables (3.1) through (3.6).

	Clamped thin-beams with constant axial stress
Governing equation	$\frac{\partial^4 y}{\partial \eta^4} - S_0 \frac{\partial^2 y}{\partial \eta^2} + \frac{\partial^2 y}{\partial t^2} = f_a(\eta, \tau)$
Boundary Conditions	$y(0,\tau) = y(1,\tau) = y'(0,\tau) = y'(1,\tau) = 0$
Characteristic equation	$S^2(1;\Omega) - T(1;\Omega) S'(1;\Omega) = 0$
Natural frequencies (without axial stress)	$\Omega_n = \begin{cases} \pi 1.5056 & n = 1 \\ \pi 2.4998 & n = 2 \\ \pi(n + 0.5) & n \geq 3 \end{cases}$
Modes shape	$Y_n(\eta) = -\frac{S(1,\Omega_n)}{T(1,\Omega_n)} T(\eta, \Omega_n) + S(\eta, \Omega_n)$

Table 3.1: Summary of the governing equation, boundary conditions, characteristic equation, natural frequencies and mode shapes for a clamped-clamped thin beam. All equation are presented in their non-dimensional form.

Boundary	Conditions		
$x = 0$	$\left[k_{xL}w - N_x b\frac{\partial w}{\partial x} + bV_x(x,y,t)\right]_{x=0} = 0$	and	$\left[k_{txL}\frac{\partial w}{\partial x} + bM_x(x,y,t)\right]_{x=0} = 0$
$x = a$	$\left[k_{xR}w + N_x b\frac{\partial w}{\partial x} - bV_x(x,y,t)\right]_{x=a} = 0$	and	$\left[k_{txR}\frac{\partial w}{\partial x} + bM_x(x,y,t)\right]_{x=a} = 0$
$y = 0$	$\left[k_{yL}w + N_y a\frac{\partial w}{\partial y} - aV_y(x,y,t)\right]_{y=0} = 0$	and	$\left[k_{tyL}\frac{\partial w}{\partial y} + aM_y(x,y,t)\right]_{y=0} = 0$
$y = a$	$\left[k_{yR}w - N_y a\frac{\partial w}{\partial y} + aV_y(x,y,t)\right]_{y=b} = 0$	and	$\left[k_{tyR}\frac{\partial w}{\partial y} - aM_y(x,y,t)\right]_{y=b} = 0$

Table 3.2: General boundary conditions for a thin rectangular plate. These conditions assume the following boundary attachments — at $x = 0$ there is a translational spring $k_{xL}[\mathrm{N/m}]$, and a torsion spring $k_{txL}[\mathrm{N.m/rad}]$; at $x = a$ there is a translational spring k_{xR}, and a torsion spring k_{txR}; at $y = 0$ there is a translational spring k_{yL}, and a torsion spring k_{tyL}; at $y = b$ there is a translational spring k_{yR}, and a torsion spring k_{tyR}.

Boundary	Conditions		
$r = a$	$\left[k_a w_r + 2\pi a N_r\frac{\partial w_r}{\partial r} - 2\pi a V_r(r,\theta,t)\right]_{r=a} = 0$	and	$\left[k_{ta}\frac{\partial w_r}{\partial x} - 2\pi a M_r(r,\theta,t)\right]_{r=a} = 0$

Table 3.3: General boundary conditions for a thin solid circular plate. These conditions assume the following boundary attachments — at $r = a$ there is a translational spring $k_a[\mathrm{N/m}]$, and a torsion spring $k_{ta}[\mathrm{N.m/rad}]$. At $r = 0$ the conditions of finite displacement is used.

Boundary	Conditions		
$x=0$	$\left[k_L w + M_L \frac{\partial^2 w}{\partial t^2} - p(x,t)\frac{\partial w}{\partial x}\right]_{x=0} + \frac{\partial}{\partial x}\left(EI\frac{\partial^2 w}{\partial x^2}\right)_{x=0} = 0$	and	$\left[k_{tL}\frac{\partial w}{\partial x} + J_L\frac{\partial^3 w}{\partial x \partial t^2} - EI\frac{\partial^2 w}{\partial x^2}\right]_{x=0} = 0$
$x=L$	$\left[k_R w + M_R \frac{\partial^2 w}{\partial t^2} - p(x,t)\frac{\partial w}{\partial x}\right]_{x=L} + \frac{\partial}{\partial x}\left(EI\frac{\partial^2 w}{\partial x^2}\right)_{x=L} = 0$	and	$\left[k_{tR}\frac{\partial w}{\partial x} + J_R\frac{\partial^3 w}{\partial x \partial t^2} - EI\frac{\partial^2 w}{\partial x^2}\right]_{x=L} = 0$

Table 3.4: General boundary conditions for a thin rectangular plate. These conditions assume the following boundary attachments — at $x = 0$ there is a mass $M_L[\mathrm{Kg}]$ with rotational inertia $J_L[\mathrm{kg.m}^2]$, a translation spring with elastic constant $k_L[\mathrm{N/m}]$ and a torsion spring $k_{tL}[N.m/rad]$; at $x = L$, there is a mass M_R with rotational inertia J_R, a translation spring with elastic constant k_R and a torsion spring k_{tR}.

	Resonance frequency (f_0)	Elastic constant (k_0)	Effective mass (m_0)
Square membrane	$5.72797\sqrt{\frac{D}{\rho t a^4}}$	$787.402\frac{D}{a^2}$	$0.607904\ \rho t a^2$
Circular membrane	$1.6259\sqrt{\frac{D}{\rho t R^4}}$	$64\pi\frac{D}{R^2}$	$0.613243\ \rho t \pi R^2$
Suspended square	$4.411\sqrt{\frac{EI}{L_b^3 \rho t(1.5344 w L_b + a^2)}}$	$\frac{768 EI}{L^3}$	$\rho t(1.5344 w L_b + a^2)$

Table 3.5: Resonance frequency, elastic constant and effective mass for the square and circular membranes and for the suspended square without axial stress. For circular membranes, R is the radius of the membrane.

	Clamped thin square plates	Clamped thin circular plates
Governing equation	$\nabla^4_{\eta\xi}\hat{w} - \hat{N}_x \frac{\partial^2 \hat{w}}{\partial \eta^2} - \hat{N}_y \frac{\partial^2 \hat{w}}{\partial \xi^2} + \frac{\partial^2 \hat{w}}{\partial \tau^2} = \hat{F}_a(\eta, \xi, \tau)$	$\nabla^4_{\hat{r}\theta}\hat{w}_r - \hat{N}_r \nabla^2_{\hat{r}\theta}\hat{w}_r + \frac{\partial^2 \hat{w}_r}{\partial \tau^2} = \hat{f}_a(\hat{r}, \theta, \tau)$
Boundary Conditions	$\hat{w}(0,\xi,\tau) = \hat{w}(\eta,0,\tau) = \hat{w}(1,\xi,\tau) = \hat{w}(\eta,1,\tau) = 0$ $\frac{\partial \hat{w}(0,\xi,\tau)}{\partial \eta} = \frac{\partial \hat{w}(\eta,0,\tau)}{\partial \xi} = \frac{\partial \hat{w}(1,\xi,\tau)}{\partial \eta} = \frac{\partial \hat{w}(\eta,1,\tau)}{\partial \xi} = 0$	$\hat{w}_r(1,\theta,\tau) = 0$ and $\frac{\partial \hat{w}_r}{\partial \hat{r}}\Big\rvert_{r=1} = 0$
Characteristic equation	$[A_{nm}][C_{nmlk}] - \Omega^4\{A_{nm}\}[B_{nmlk}] = 0$	$\frac{\delta}{2}J_n(\epsilon)(I_{n-1}(\delta) + I_{n+1}(\delta)) - \frac{\epsilon}{2}I_n(\delta)(J_{n-1}(\epsilon) - J_{n+1}(\epsilon)) = 0$
Natural frequencies (without axial stress)	$\Omega_j = \begin{cases} 5.9992 & j = 1 \\ 8.5688 & j = 2,\ j = 3 \\ 10.411 & j = 4 \end{cases}$	$\Omega_{0m} = \pi \begin{cases} 1.0174 & m = 1 \\ 2.0074 & m = 2 \\ 3.0046 & m = 3 \\ 4.0034 & m = 4 \end{cases}$
Modes shape	$\hat{W}_j(\eta,\xi) = \sum_n^N \sum_m^N A^{(j)}_{mn} X_n(\eta) Y_m(\xi)$	$W_{nm} = \left(J_n(\epsilon_{nm}\hat{r}) - \frac{J_n(\epsilon_{nm})}{I_n(\delta_{nm})} I_n(\delta_{nm}\hat{r})\right)(\hat{r})\cos(n\theta)$

Table 3.6: Summary of the governing equation, boundary conditions, characteristic equation, natural frequencies and mode shapes for a clamped thin square and circular plate. All equation are presented in their non-dimensional form.

Chapter 4

Experimental Characterization

An initial characterization of the purposed structures is presented here. Two distinct experimental setups were used — one for high frequency characterization at low pressure and one for quasi-DC and audible range measurements. The former highlights intrinsic mechanical properties of the resonators such as resonance frequencies and axial stress while the later allows for measurements of absolute deflection in the audible range at room pressure and temperature.

4.1 Quasi-DC and audible range setup

4.1.1 Introduction

This simple setup comprises a laser, focused on the membrane, and a quadrant photodiode detector aligned with the reflected beam off the membrane. The current generated from the detector is converted to a potential difference by a transimpedance amplifier and fed to a lock-in amplifier, synchronized with the signal generator that is exciting the membrane.

The following nomenclature is introduced — δ is the amplitude of vibration of the membrane, δ_l is the amplitude of vibration of the reflected beam on the detector, $V_A(t)$ is the corresponding instantaneous voltage of quadrant A after amplification, $V_B(t)$ is the corresponding instantaneous voltage of quadrant B after amplification, $V_{AB} = V_A(t) - V_B(t)$ is the corresponding instantaneous voltage of quadrant A minus the corresponding instantaneous voltage of quadrant B after amplification and ${V_{AB}}^{\text{out}}$ is the output voltage read by the lock-in amplifier, which corresponds to the root-means-square (RMS) value of the input signal at the reference frequency.

From Figure 4.1 (b) one may write,

$$\delta = \cos\frac{\pi}{4}\,\delta_l = \sqrt{2}/2\delta_l \tag{4.1}$$

The position of the beam in the detector can be mapped by measuring the DC output V_{AB} for several position of the detector. From the slope around the central position one may define a constant of proportionality, ζ, by

$$\zeta \equiv \frac{\delta_l}{\Delta V_{AB}} \tag{4.2}$$

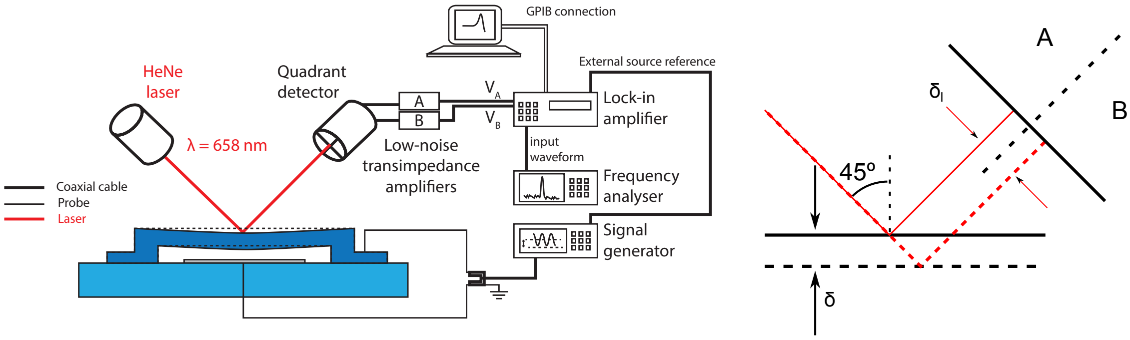

(a) (b)

Figure 4.1: Quasi-DC experimental setup. Sub-figure (a) shows the overall view of the setup and sub-figure (b) illustrates the relation between the deflection of the membrane and the position of the beam on the detector.

where ΔV_{AB} is the amplitude of oscillation of the input signal V_{AB}. Note that the absolute value V_{AB} has no meaning for the lock-in measurement because it only measure amplitude of oscillations and not the absolute position.

If the membrane is vibrating harmonically at the reference frequency — this is confirmed using the frequency analyser and/or oscilloscope — then $V_{AB} = {V_{AB}}^{\text{out}}\sqrt{2}$ and from relations (4.1) and (4.2) one may write

$$\delta = \sqrt{2}/2\ \zeta V_{AB} = \zeta {V_{AB}}^{\text{out}} \tag{4.3}$$

So the amplitude of vibration of the membrane is just the value read at the lock-in output multiplied by the proportionality constant ζ. The output data is directly transfered to the computer via a GPIB connection.

4.1.2 Absolute deflection characterizations

First generation structures alone were characterized using the quasi-DC setup. The structures are $\sim$ 2 μm thick with a target air gap of 1.5 μm. All the results presented are for the perpendicular geometry with 20 μm wide tethers.

Figure 4.2 (a) shows the frequency spectrum of a 300 μm by 300 μm membrane held by 200 μm long tethers in the audible range. This configuration shows a very good positioning of the resonance frequency, just over the limit of the audible range at $\sim$ 22.5 kHz, which assures a flat response through all the audible range. At resonance the amplitude of deflection goes well beyond the target air gap height indicating that the structures are indeed *lifted* (figure not shown). This is a consequence of the in-plane stress which forces the anchors to bend to reach an equilibrium position. This has the benefit of achieving higher air gap heights without the need of depositing the sacrificial layer with the corresponding thickness, which would lead to more complexity in the fabrication. It also allows the fabrication of longer tethers and plates and reduces the squeeze-film damping. On the downside it reduces the electrostatic force. Also, such strategy to control the air gap height is problematic because of the low control over the residual stress through the entire substrate.

Figure 4.2 (b) shows the response of a 500 μm by 500 μm membrane held by 100 μm long tethers at

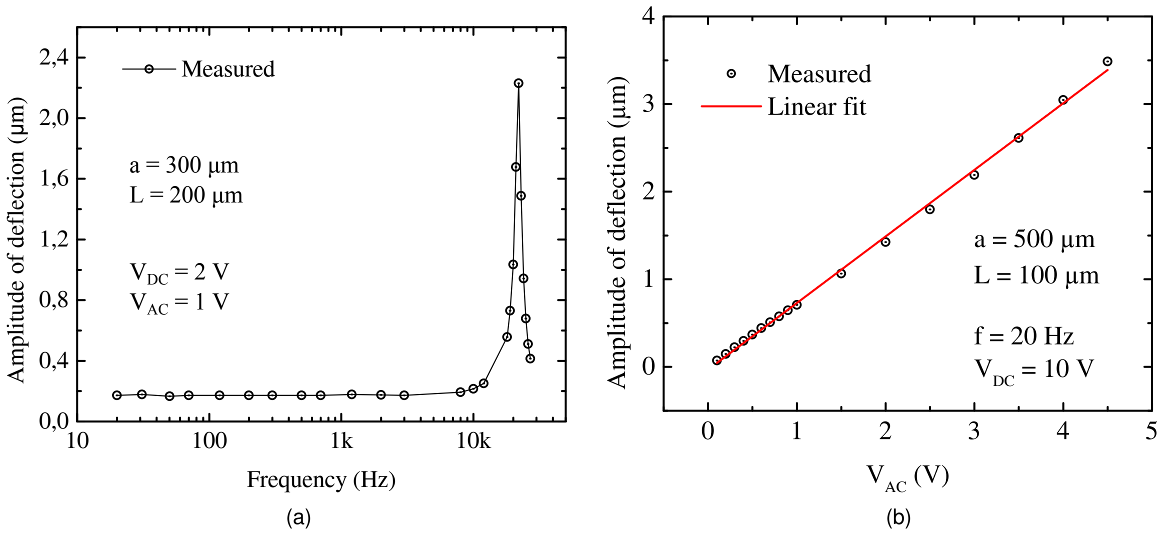

Figure 4.2: (a) Frequency spectrum in the audible range of a 300 μm by 300 μm membrane held by 200 μm long tethers and (b) amplitude of deflection at 20 Hz of a 500 μm by 500 μm membrane held by 100 μm long tethers at constant DC bias as a function of the input excitation signal.

constant frequency (20 Hz) and DC bias (10 V) as a function of the amplitude of the input sinusoidal signal. As in the case of the previous example the structure deflects beyond the target air gap height indicating that the structures are lifted. The membrane shows linear behaviour within the range presented with a sensitivity of (0.76 $\pm$ 0.01) $\mu m/V$.
Further characterization on these structures was not carried because of their incompatibility with a loudspeaker application (see Chapter 5). Nonetheless, preliminary results such as the ones presented above did serve as a starting point for the design of second generation structures, namely for a rough estimation on the in-plane stress, feasibility of suspended features with dimensions of the order of 500 μm and validation of the quasi-DC experimental setup.

4.2 High frequency detection setup

4.2.1 Introduction

The high frequency detection setup also uses an optical detection method but instead of a quadrant detector it uses a APD detector (*Hamamatsu C5331*) connected to a network analyzer (HP Network Analyser 4195A). Because the detector has a low frequency cut around 4 kHz this setup is only used for measurement above 50-100 kHz and no information about absolute deflection is provided. Instead, higher modes of vibration can be detected in a pressure controlled chamber with information about mode shape a quality factor. The setup is summarized in Figure 4.3 — An external source is used to set a DC bias and the membrane is excited harmonically by the network analyser. The output of the detector is fed to the network analyser. The sample is wire bonded to a chip carrier and placed on a pressure controlled chamber.

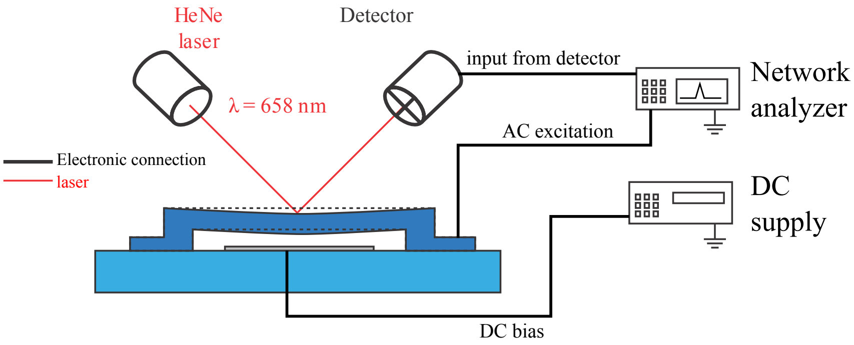

Figure 4.3: High-frequency experimental setup.

4.2.2 Resonance frequencies characterization

The high-frequency setup allows the determination of the resonance frequencies of the loudspeakers, its quality factor and resonance peak shape as a function of the applied voltage, temperature and pressure. The quality factor is defined here as the ratio between the resonance frequency, f_0, and the width of the resonance peak at -3 dB of its height, $w_{-3\mathrm{dB}}$, namely,

$$Q = \frac{f_0}{w_{-3\mathrm{dB}}} \tag{4.4}$$

A Lorentzian fit of general form

$$f = f_0 + \frac{2A}{\pi} \frac{w}{4(f - f_0)^2 + w^2} \tag{4.5}$$

is used to fit the data where A is the area under the fitting curve and w is the height of the peak at 50 % of its height. The quality factor can be an indicator of the properties of the material. If the chamber pressure is low enough, so that intrinsic dissipation dominates over exterior dissipation, the quality factor will carrier information on thermoelastic damping (TED), anchor dissipation and other intrinsic dissipation mechanisms. Such information plays a little role on the design of a loudspeaker, which is actuated at ambient pressure where the dissipation is dominated by squeeze-film damping, but it is important for the design of high quality materials which will influence the durability and reliability of the loudspeaker.

Suspended Square

Suspended square membranes were fabricated using the first generation process. Membranes 3 μm thick with an air gap height of 1 μm and sides from 210 μm up to 710 μm were fabricated. The supporting tethers are 10 μm long than the square side (see Figure 3.13). The frequency spectrum from 100 kHz to 2 MHz was measured and plotted in Figure 4.4 for the 210, 410, 610 and 710 membranes. The possibility of fabrication of membranes up to 700 μm was only possible using recipe 4 in table 2.1 for 200 ° C which has higher tensile stress. The structures were ”lifted” (figure not shown) as a result of this tensile stress which lead to higher tolerance to the release step, where stiction sets an upper limit on the dimensions that can be used.

Figure 4.5 shows the dependence of the first resonance mode with the dimensions of the tethers side.

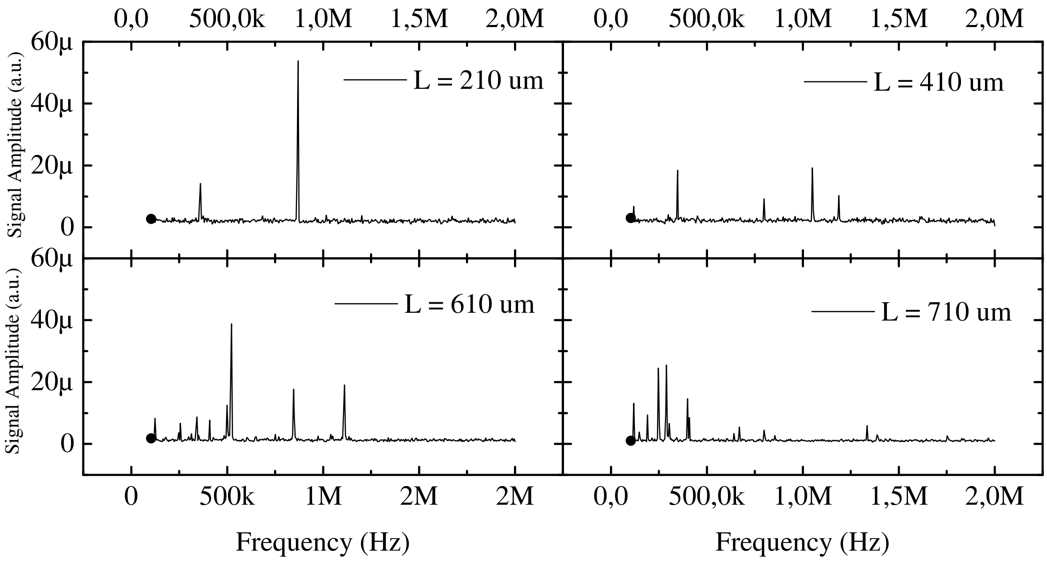

Figure 4.4: Frequency spectrum overview for the suspended square for different membrane dimensions.

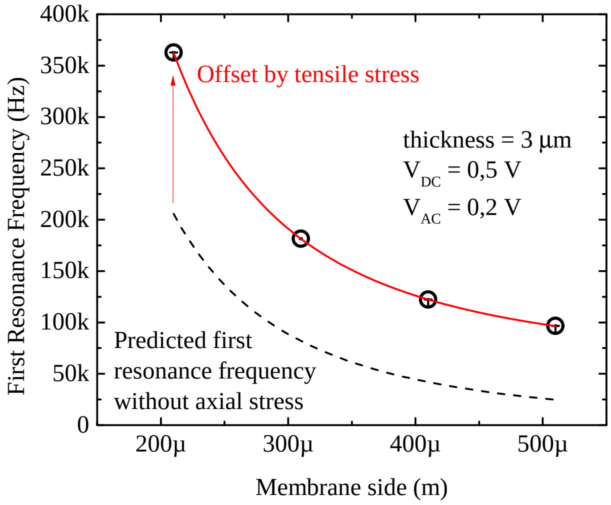

Figure 4.5: First resonance frequency as a function of the side of the membrane for the suspended square geometry with in-plane tensile stress.

Based on equation (3.36) a non-linear fit of general form

$$f = f_0 + c_1 L^{c_2} \tag{4.6}$$

is used where f_0, c_1 and c_2 are fitting parameters and L is the tether length. The resulting fit (in red) shows very good correlation with the measured data with an adjusted R-squared of 1 for $f_0 = (57.0 \pm 0.45)$ kHz, $c_1 = (0.99 \pm 0.07)$ Hz.m$^{2.3}$ and $c_2 = -2.3 \pm 0.01$. By comparing to the expected resonance frequency without axial stress, the in-plane tensile stress assumption is further validated in conformation with previously obtained results.

Figure 4.6 shows the dependence of the resonance peak shape with DC bias for a $210\mu m$ suspended square and the corresponding change in the resonance frequency. As the membrane side increases, the stiffness decreases and the influence of the DC bias will be more pronounced. The frequency-to-voltage ratio measured for the 210 μm membrane is 0.83 kHz/V. It is expected that larger dimension yield larger ratios. Applications for a voltage-to-frequency converter can also be derived from these type

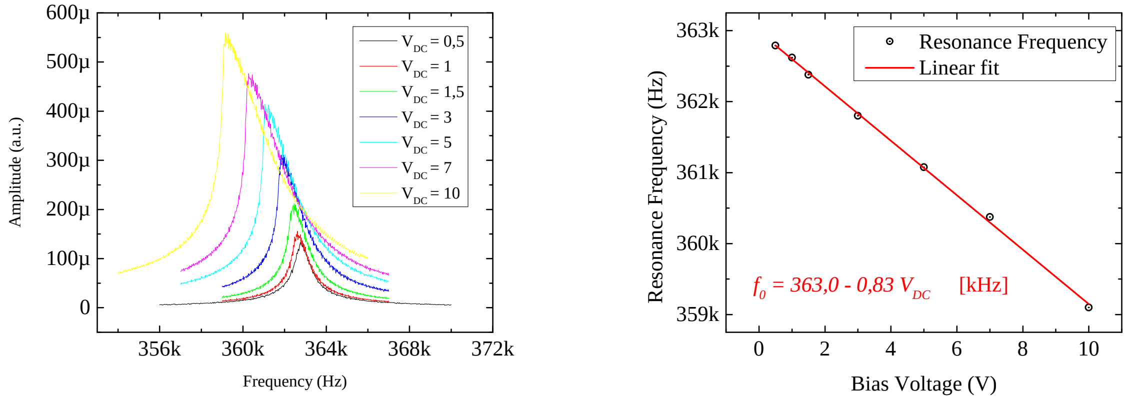

(a) (b)

Figure 4.6: Effect of the bias voltage on the (a) resonance peak shape and (b) resonance frequency for a suspended square with 210 μm side.

of structures.

Clamped Membranes

Clamped membranes were fabricated using the modified version of the glass-aluminium process and using the silicon-silica process for the amorphous silicon deposition tests (see Chapter 2). Figure 4.7 shows the frequency spectrum of a clamped rectangular membrane with 500 μm radius for the glass-aluminium process. The first resonance mode predicted for these structures (see Chapter 3) is around 155 kHz which suggests an in-plane stress value between 10 MPa to 100 MPa based on Figure 5.3 which shows the dependence of the first resonance frequency with in-plane tensile stress, membrane side length and thickness. This is in line with the values expected for this fabrication process.

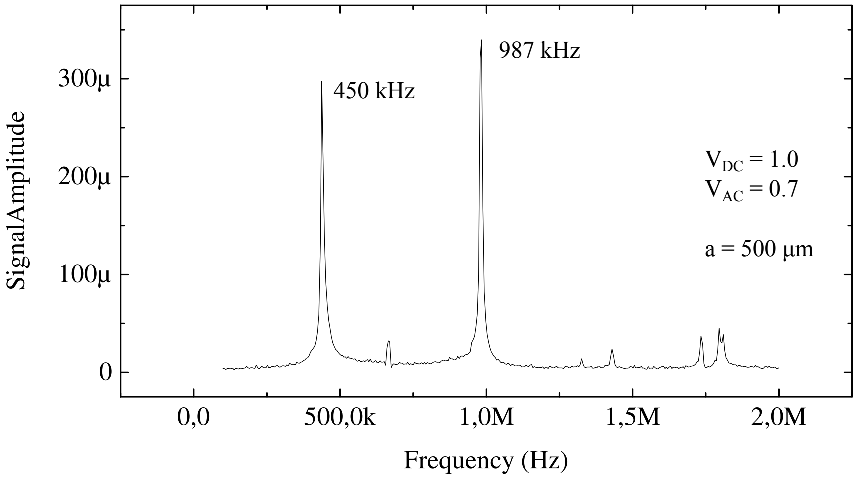

Figure 4.7: Frequency spectrum of a clamped rectangular membrane with 500 μm radius using the revised aluminium-glass process (see Appendix A).

Figure 4.8 shows in detail the two highest resonance peaks in Figure 4.7 indicating the quality factor of each one. Note that these do not correspond to the first two natural resonance modes, since only symmetrical modes are excited[1].

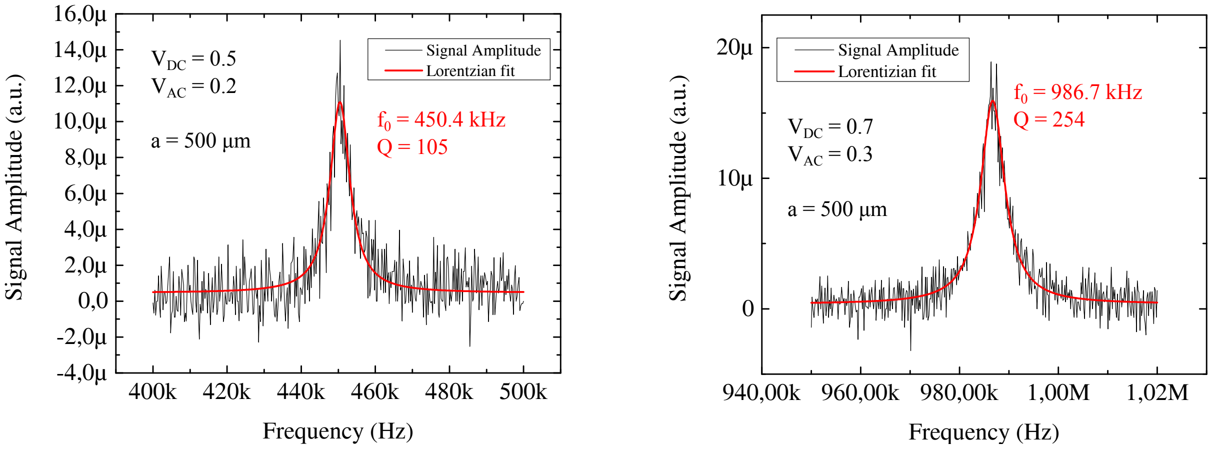

(a) (b)

Figure 4.8: Detail on the two highest resonance peaks in Figure 4.7

Figure 4.9 shows the variation of the first resonance for the equal membranes across the die indicating good reproducibility. The mean calculated resonance frequency is 420.7 kHz with a standard deviation of 27.4 Hz corresponding to 6.5 % of the mean value. This is an important assessment if arraying is required to assure that all membranes show minimal variation in their mechanic characteristics.

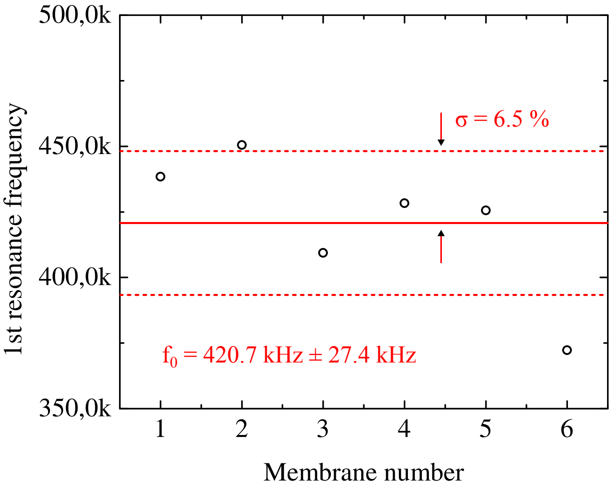

Figure 4.9: First resonance frequency variation across a single die of 500 μm clamped membranes showing a standard deviation of 6.5 %.

Finally, Figure 4.10 shows a SEM micrograph of a 800 μm side clamped membrane using the silicon-silica process for the amorphous silicon deposition tests and Figure 4.11 shows the corresponding frequency spectrum The membranes are 3 μm thick. Although these first structures shows some cracks over the border, which probably is the origin of the high number of resonances, and there is still some problems during the structure release to be overcome the realization of the first standing and vibrating membranes for the newly developed process is definitely a landmark.

---

[1] Because of perforations on the membrane, gate design and small imperfection from the fabrication, asymmetrical modes will also be excited but to much less extent than symmetrical modes.

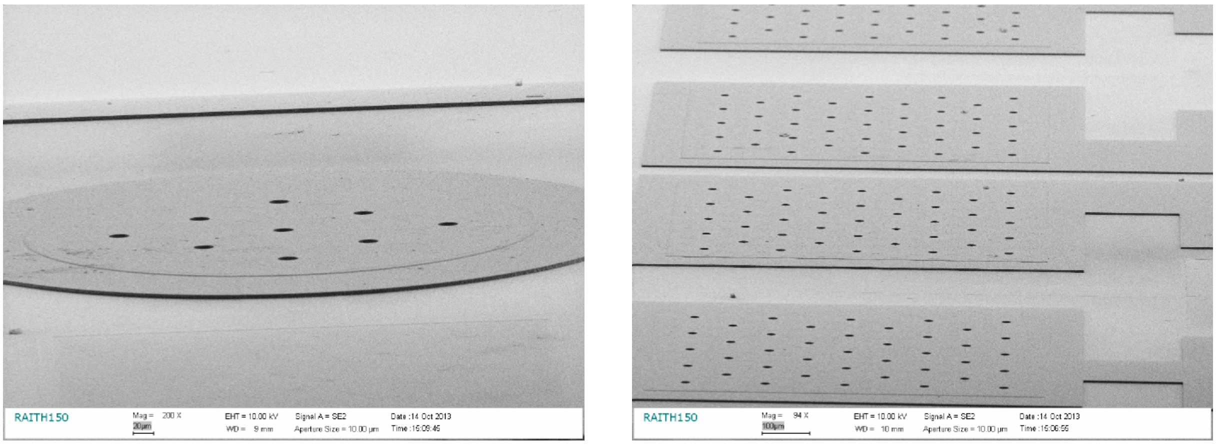

(a)

(b)

Figure 4.10: Second generation released clamped membranes fabricated using the amorphous silicon deposition test process. Sub-figure (a) shows 500 μm circular membrane and sub-figure (b) shows an array of released membranes.

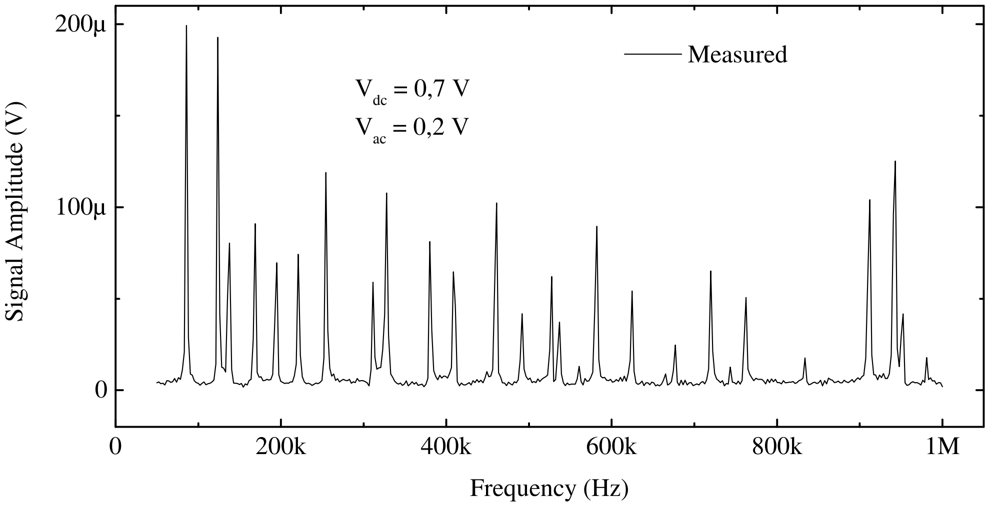

Figure 4.11: Frequency spectrum of a 800 μm clamped membrane for the silicon-silica process.

4.3 Conclusion

An initial inspection on the mechanical properties of the proposed structures was presented. Using the first generation process it was possible to assess some mechanical properties of said structures such as resonance frequencies, in-plane tensile stress, and the dependence of the resonance frequencies and resonance peak shape with DC bias. A working prototype for the second generation structures was also presented showing the viability of the process. The results suggest a tensile stress of the order 10 MPa to 100 MPa in line with previously obtained results, roughly doubling the resonance frequency and increasing the pull-in voltage (see Chapter 5). It is also shown the variation of the first resonance frequency across a full die (6.5 × 6.5 mm^2) of 500 × 500 $\mu\mathrm{m}^2$ membranes with a standard deviation of 6.5 % of the mean value. The results presented here form a basis for further research of the mechanical properties of the clamped and suspended membranes.

Chapter 5

Discussion

There are several parameters that affect the overall performance of the device. Understanding how each one affect the response of the system, the limits of validity of the previous assumptions and the limitations imposed by technology is essential to the design and optimization of the device. In the following discussion several considerations are presented supported by examples based on the above discussion, reports on the literature and accumulated knowledge from the group. With a few exceptions, duly noted in the text, the fundamental ideas and concepts apply to all three geometries proposed here.

5.1 First generation vs Second generation

The first generation structures were design as an extension of a well developed microfabrication process for amorphous silicon thin beams and plates. This is an attractive process due to its low temperature characteristics, great flexibility on the choice of substrate and overall simplicity. The frequency spectrum of the first batch of structures was measure showing values of the order of magnitude expected for the deflection but with high variation from die to die. This indicates low tolerance to specific steps in the fabrication (see Chapter 2). Also noticeable was the effect of the intrinsic stress on these structures — although extensive characterization was not possible due to a very low yield of functioning membranes, the structures were clearly *lifted* (figure not shown)). Unfortunately this geometry proved to be inconsistent for the realization of a loudspeaker. A suspended membrane radiates like a dipole (see for example Morse and Ingard [1968]) meaning that the pressure immediately above a bellow the membrane are equal and opposite or, in other words, the front-wave and back-wave are in complete opposition of phase. For these first generation membranes there is no path for the back-wave to propagate and two phenomena can happen —the back-wave is reflected into the front volume or the air gap is sufficiently small so that there is no propagation and the air between the plates is *squeezed*, behaving like a spring. For the former, because the characteristic dimensions are much smaller than the wavelength of the wave (taken at 1 kHz) the back and front wave will interfere destructively cancelling each other. For the latter, although the compression of air strongly reduces the amplitude of the back-wave it also greatly increases the overall stiffness of the system, reducing the vibration amplitude and therefore the front-wave amplitude.

The second generation structures were design considering the limitation of the first generation ones. The perforation of the substrate proved to be indispensable based on several numerical simulations (results not shown). Due to technology limitations the substrate had to be change to crystalline silicon to allow back-side/front-side alignment, material compatibility and the etch of the perforations. The necessity for complete physical isolation of the back-side and front-side volumes is not clear and for this reason both clamped structure and open structures are presented. Open structures have particular advantages over clamped ones such as simplification in the fabrication process, more tolerance to the intrinsic stress of the structural layer and more degrees-of-freedom for performance optimization. Also, relative to the first generation structures, electric passivation layers are introduce to assure electric isolation between the substrate and gate electrode and between the membrane and the gate electrode (for the case of the clamped structures).

5.2 Design considerations

5.2.1 Membrane dimensions

The are of the membrane affects the electrostatic force, the elastic constant, the electrostatic elastic constant, the damping coefficient and the natural frequencies.

From equations (3.111) and (3.108), the elastic constant and natural frequency is inversely proportional to the area of the membrane, so by increasing(decreasing) the side of the membrane the elastic constant will decrease(increase) together with the natural frequency. This is somewhat intuitive, the membrane becomes floppier and easier to deflect when its area is increased (while keeping the thickness constant) and vice-versa. This is not entirely true for the suspended square case. Because the stiffness of the system is dominated by the tethers[1] an increase in area can be accomplished while keeping the same stiffness (see Figure 5.1). In other words, the stiffness of the system can be controlled independently of its mass introducing a new degree-of-freedom to control the elastic constant and resonance frequency of the membrane.

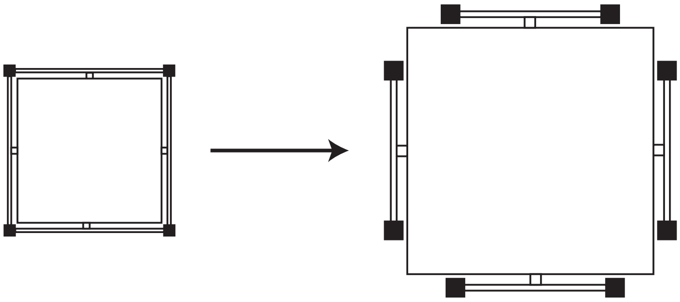

Figure 5.1: Changing the area of the suspended square independently of the length of the tethers. The anchor points are are marked as black.

The electrostatic force depends linearly on the area of membrane so increasing (decreasing) the area will increase (decrease) its strength. The same is valid for the electrostatic elastic constant and damping

---

[1] For the case where the area of the suspended square is much bigger than that of the tethers

coefficient. The exact form of the damping coefficient is hard to determine and it is highly dependent on the geometry used. However, for dense perforated geometries, with perforation cell area much smaller than the area of the membrane, it is reasonable to assume that the pressure is a smooth function of the position. Using the simple model described above, from equations (3.139) and (3.128) both the electrostatic and damping force depend linearly with the area of the membrane, making the side of the membrane a poor parameter for the electrostatic vs damping force optimization.

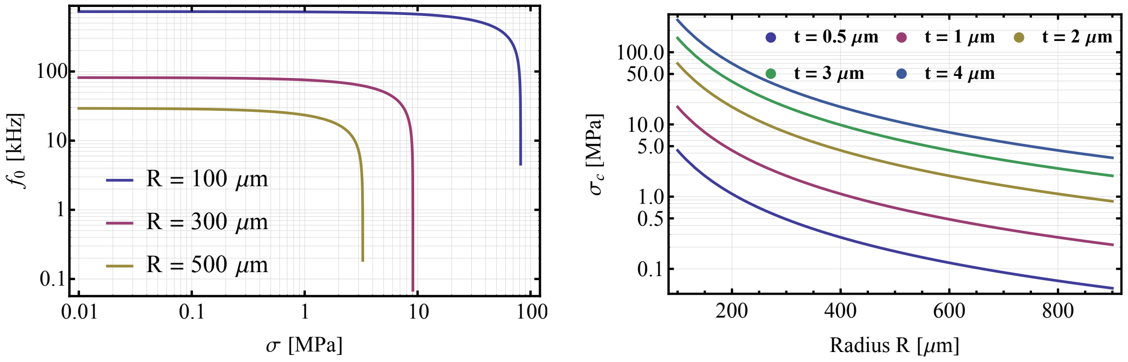

(a)

(b)

Figure 5.2: (a) First resonance frequency f_0 as a function of the compressive stress for 2 μm thick circular membranes with different radius and (b) the critical compressive axial stress at which the membrane will buckle as function of membrane's radius for different thicknesses.

The residual stress present in the structural layer will have affect the resonance frequency and elastic constant of the membrane depending on its size (see Chapter 4). Figure 5.2 shows the effect of the compressive axial stress on the natural frequency of the first axisymmetric mode of a circular membrane for several different radii. Figure 5.2 (b) show the critical frequency at which the structure buckles (see for example Timoshenko [1951]). This is an undesired effect and the higher the radius the lower is this critical frequency. For the fabrication methods used in this work, residual stress of the order of 1 MPa are typical so thick structures, above 2 or 3 μm are required to have some flexibility in the membrane's area size. The resonance frequency for the case of tensile stress is plotted in Figure 5.3 for different thicknesses and radii. Taking again 1 MPa as the reference order of magnitude its easy to see that the effect of stress must be accounted for thinner and larger membranes. A resonance frequency close to end of the audible range would be ideal, making the response of the membrane flat in this range while keeping the stiffness of the membrane to a minimum. Take as an example the R = 400 μm, t = 1 μm membrane — without axial stress the resonance frequency is very well place just above the 20 kHz threshold but at 5 MPa it roughly doubles to about 50 kHz, quadrupling the stiffness of the system[2]. Thus, the intrinsic stress of the structural layer is a critical design parameter and fine optimization of deposition conditions must be pursued for reliability.

Figure 5.4 show the effect of the tensile stress on the resonance frequency of a *single beam* (not the entire structure). The same arguments can be made here, the axial stress has a pronounced effect on the resonance frequency for thinner and larger beams. Here however, because the size of the tethers

---

[2] It is expect that the effective mass of the membrane is not strongly affected so that the stiffness varies with the resonance frequency as if there were no axial stress

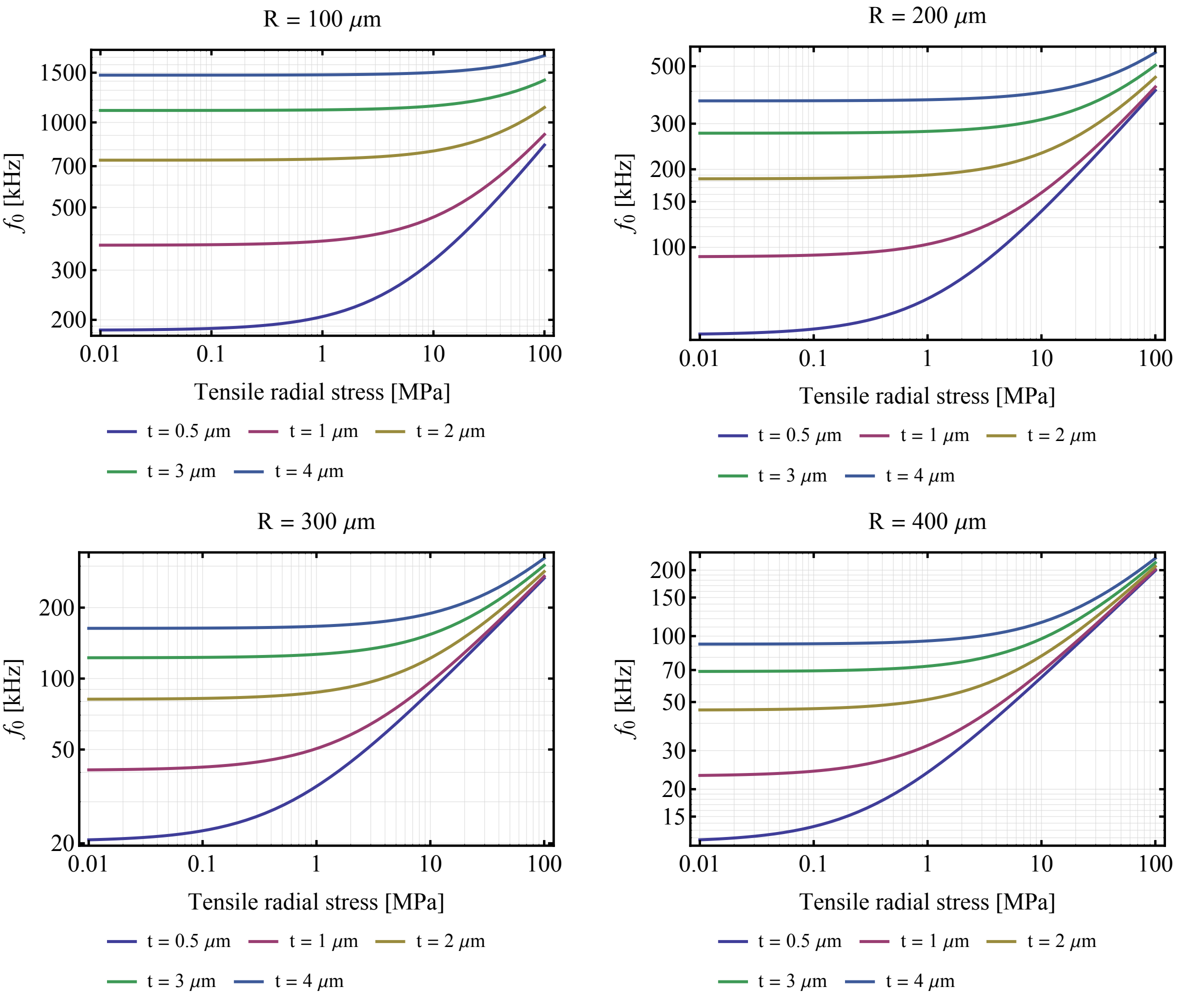

Figure 5.3: Effect of radial tensile stress on the first resonance frequency of circular membranes.

is not dependent on the side of the suspend square, it may be possible the realization of larger active areas, using thicker and smaller tethers, with good tolerance over the intrinsic stress of the structural layer.

The thickness of the membrane has influence on the elastic constant and resonance frequency of the membrane alone. From equations (3.111) and (3.108) comes that the elastic constant is proportional to the cube of the thickness while the resonance frequency is linearly proportional with the thickness. (see Figure 5.5). Since the thickness doesn't affect the electrostatic force nor the damping force it serves as a fine-tunning parameter to adjust de stiffness of the membrane independently of its area. Figure 5.5 shows the natural frequency and elastic constant as a function of the membrane's side for different thicknesses.

The limitation on the thickness is imposed by the technology, namely in the PECVD of the a-Si:H step (see chapter 2). Residual stress during the deposition makes it difficult to go over 3 μm.

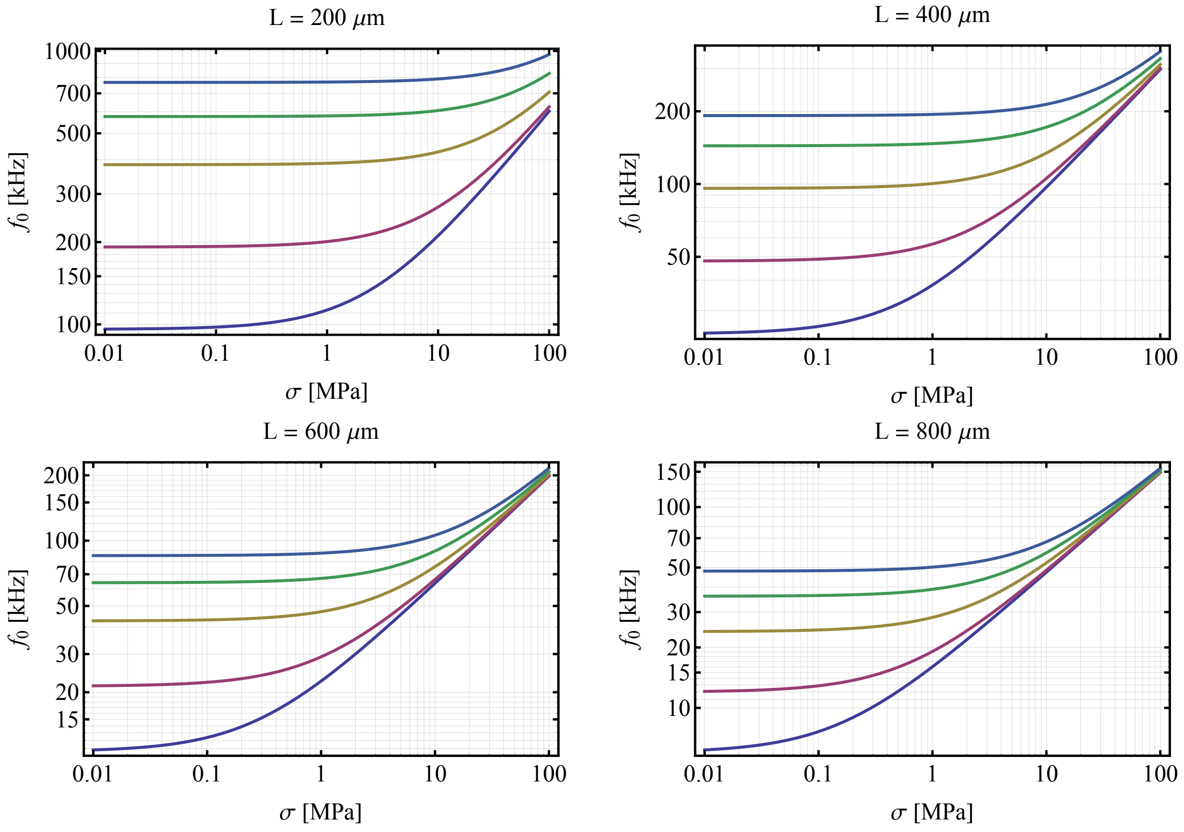

Figure 5.4: Effect of radial tensile stress on the first resonance frequency of thin beams.

5.2.2 Pull-in Voltage, Air gap height and Bias Voltage

A common parameter in the characterization of MEMS is the *pull-in voltage* — the voltage at which the membrane collapse onto the gate electrode. This happens because the electrostatic force depends on the square of the distance between the membrane and gate and, as the membrane approaches the gate (while increasing the voltage drop across the plates), the magnitude of the electrostatic force increases faster than the elastic force of restoration of the membrane, up until the point where a stable balance can no longer be reach and the membrane collapses. Using the ODF approximation the equilibrium position of plate is found by equating the restoring force with the electrostatic force, that is,

$$k_e x = \frac{1}{2}\epsilon A \frac{V_0^2}{(g_0 - x)^2} \tag{5.1}$$

This can be written in a non-dimensional form by defining a normalized displacement, $\hat{x} = x/g_0$ and an electrostatic constant $e^2 = {}^{\epsilon A}/_{2k_e g_0^3}\ [V^{-2}]$, yielding

$$\hat{x} = \frac{e^2 V_0^2}{(1 - \hat{x})^2} \tag{5.2}$$

Equation (5.2) has 3 roots which can be evaluated by analysing the sign of the quantity (Magrab [2012], chapter 2)

$$D = e^2 V_0^2 \left(\frac{e^2 V_0^2}{4} - \frac{1}{27} \right) \tag{5.3}$$

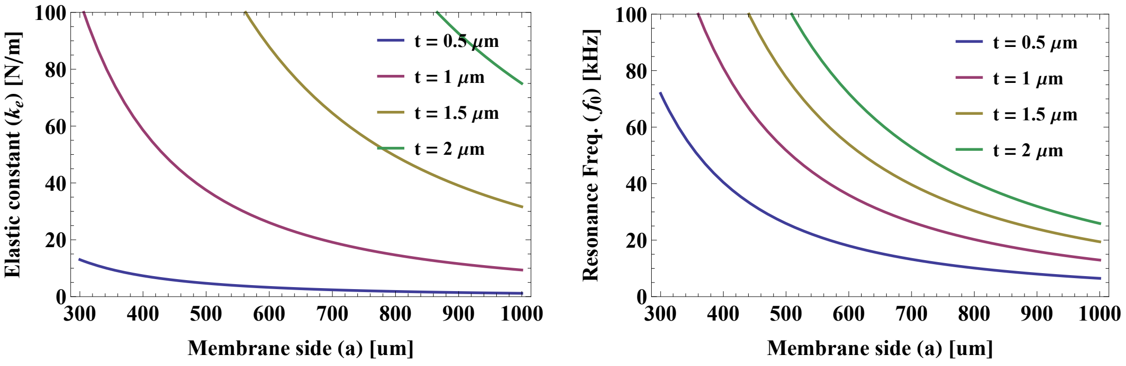

(a) (b)

Figure 5.5: Elastic constant (a) and resonance frequency (b) as a function of the side and thickness of a rectangular membrane without axial stress. The case for circular plates yields very similar values as can be seen from table (3.5).

Figure (5.6) shows the real part of the 3 possible solutions to equation (5.2). Solution 2 and 3 have no physical meaning since for zero applied voltage the displacement must be zero. So, if $e^2V_0^2 < 4/27$ there is one stable solution and if $e^2V_0^2 > 4/27$ there aren't any solutions with physical meaning which leads to

$$V_{pull-in} = \frac{1}{e}\sqrt{\frac{4}{27}} = \sqrt{\frac{8k_e x_0^3}{27\epsilon A}} \tag{5.4}$$

This simple approximation neglects non-linearities of the electrostatic force and restoring force but provides a good reference in MEMS design. It is also noted that in Figure (5.6) the effect of the perforated geometry was ignored (see discussion bellow). To account for this the correction factor $\gamma(\eta')$ must be introduced into equation (5.1) which redefines the electrostatic constant e^2, leading to,

$$V_{pull-in} = \sqrt{\frac{8k_e x_0^3}{27\gamma(\eta')\epsilon A}} \tag{5.5}$$

The air gap height influences the electrostatic force and the damping coefficient. The smaller the gap the higher the electrostatic and damping force, as can be seen from equation (3.139) and (3.128). The desired amplitude of vibration should be taken in consideration when designing the air gap height to account for unintended non-linearities. From the above discussion, the linear equation of motion is only valid under the assumption that the vibration amplitude is much smaller than the air gap height. When this assumption is not valid, the waveform is deformed and the response of the membrane is no longer proportional to the input, harmonic, signal. Figure 5.7 shows the complete numerical solution to equation (3.107) and the small displacement approximation (3.143) for two different cases - one where there isn't an appreciable waveform distortion and another where the waveform deformation is clear. The plot range in the displacement axis goes from 0 to $1/3$ of the air gap to highlight the effect of the pull-in effect which limits the displacement of the membrane to $1/3$ of the gap. The closer the plate moves to this limit the higher the deformation will be. When no voltage threshold is imposed an high air gap height is typical in MEMS devices for loudspeakers (Neumann and Gabriel [2008], Roberts et al. [2007], Kim et al. [2005]). However, in this work, the ideal maximum voltage of actuation is around 3.3 V so a careful

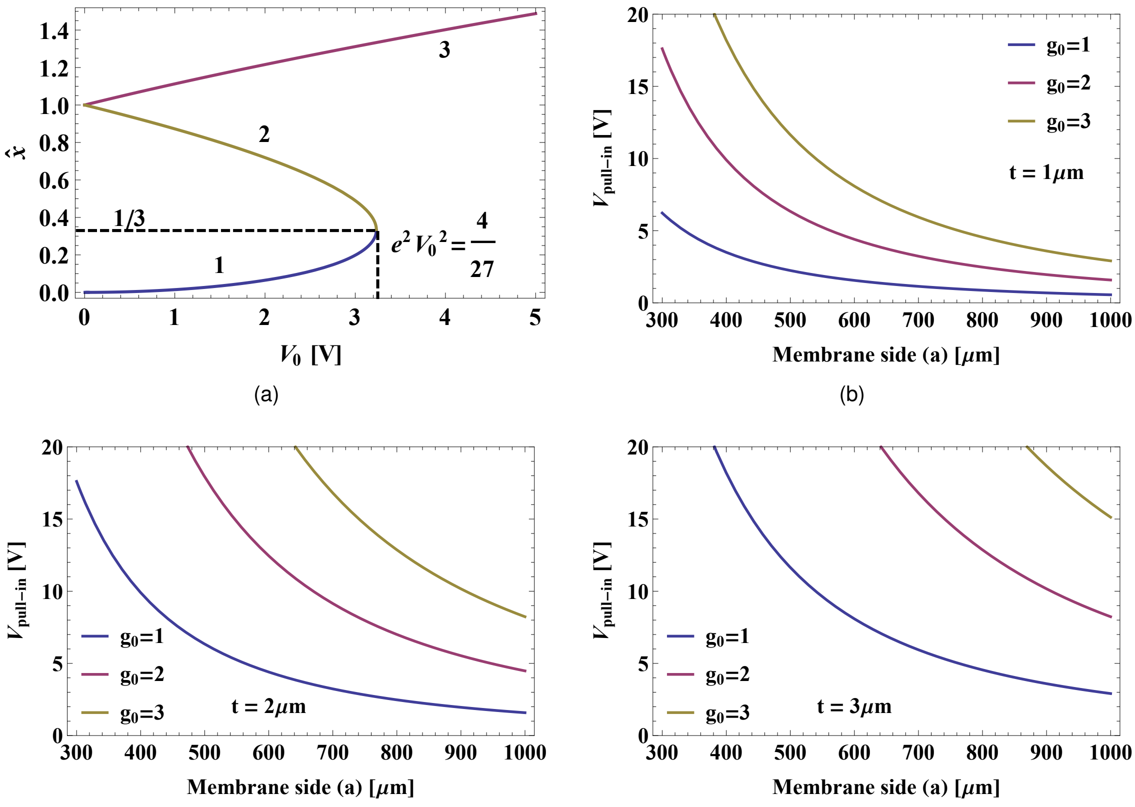

(a) (b)

(c) (d)

Figure 5.6: The pull-in effect. Sub-figure (a) shows the real part of the three solution to equation (5.2). Solutions (2) and (3) have no physical meaning, only solution (1) represents the equilibrium displacement, valid for $0 \leq \hat{x} \leq 1/3$. Sub-figures (b), (c) and (d) show the pull-in voltage for a membrane thickness $t = 1,\ 2$ and 3, respectively, for different air gap heights.

optimization of the air gap height is necessary to minimize non-linearities while keeping a sufficiently high electrostatic force. Special techniques can also be employed to allow deflections beyond $1/3$ of the air gap height and increase the pull-in. A simple example is the use of an electronic capacitor (C_f) in series with the resonator (Seeger and Crary [1997]) (Figure 5.8). This capacitor creates a negative feedback effect by decreasing the voltage across the resonator as the free electrode is pushed. It is shown that if $C_0/C_f > 2$ ($C_0 = \epsilon A/g_0$ and C_f is the capacitance of the feedback capacitor) the pull-in effect is completely removed and the membrane can swing over the full gap. The downside is a high voltage cost to reach any equilibrium position. An improvement to this scheme is the use of a MOS capacitor operated in depletion. It is shown that the voltage require to close the gap can be reduce to half of that necessary with the simple capacitor.

The bias voltage essentially sets the membrane's operating point and allows the membrane to be driven at the excitation frequency. In equation (3.131) the term in $\cos(2\omega t)$ is discarded on the imposition that it is much smaller than the remaining terms. To see how this restricts the values of V_{DC} and V_{AC} a factor α is set between the term in $\cos(2\omega t)$ and the fundamental term ($\cos(\omega t)$), leading to

$$2V_{DC}V_{AC} \geq \alpha \frac{V_{AC}^2}{2} \tag{5.6}$$

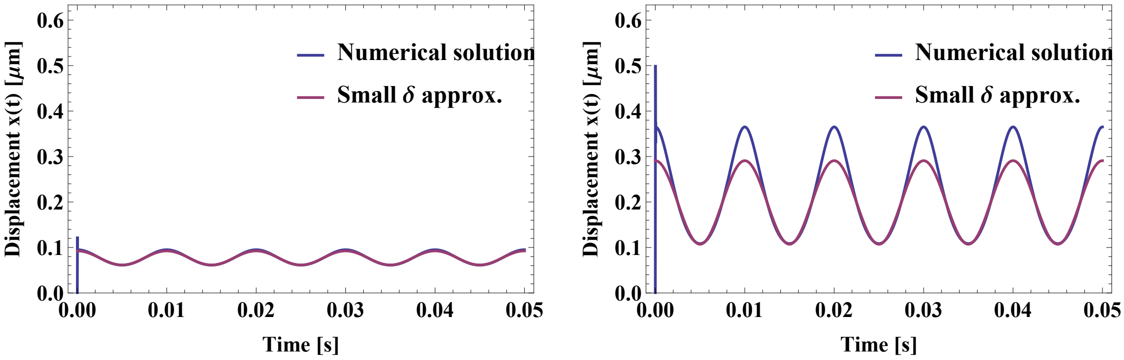

(a) (b)

Figure 5.7: Sample waveform for the numerical solution of the equation of motion (3.107) and for the small amplitude approximation (3.143). Sub-figure (a) show the case where the small displacement approximation is in good agreement with the complete solution of equation (3.107) and sub-figure (b) show the case where the small displacement approximation starts to fail and the waveform distortion must be taken into account. The plot range is from 0 to $1/3$ of the air gap height.

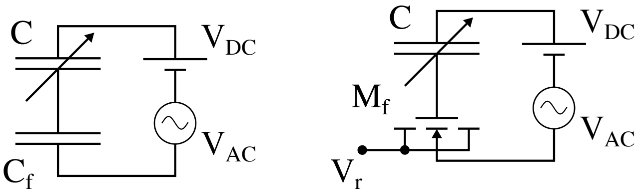

(a) (b)

Figure 5.8: Feedback technique to eliminate the pull-in effect using (a) a simple capacitor or (b) a MOS capacitor.

which immediately leads to the restriction

$$\frac{V_{DC}}{V_{AC}} \geq \frac{\alpha}{4} \tag{5.7}$$

It is also possible to minimize the static term in (3.131) with respect to the fundamental one. Consider that $V_{DC} = \alpha V_{AC}$. From equation (3.131) the ratio, R, of the two components is

$$R = \frac{V_{DC}^2 + V_{AC}^2/2}{2V_{DC}V_{AC}} = \frac{1+\alpha^2/2}{2\alpha} \tag{5.8}$$

which is minimum for $\alpha = \sqrt{2}$ The extent to which the first harmonic is to be damped must have in consideration the overall response of the system including electronic restrictions and acoustical and psychoacoustical factors (see for example Rossing [2007], chapter 13).

5.2.3 Perforation cell density

The perforation cell density plays a critical role in optimizing the electrostatic vs damping force. To account for the effect of the perforated electrode on the displacement of the membrane it is assumed that the deformation shape is not significantly altered and only the maximum displacement is affected.

A correction factor γ is introduced such that

$$\delta_{\text{max}} = \gamma\delta_{\text{max0}} = \gamma\frac{F_0}{k_0} = \frac{F_0^{\text{eff}}}{k_0} \tag{5.9}$$

where δ_{max0} and F_0 is the maximum displacement of the membrane and the total force acting on the membrane, respectively, as if there were no perforations, δ_{max} is the maximum displacement of the membrane accounting for the perforated geometry and F_0^{eff} is an *effective total force* acting on the membrane.

Using a finite-element-method (FEM) simulation the maximum displacement was calculated for a constant uniform load for different values of r_0, r_c and a. It is reasonable to assume that, for dense perforated geometries, γ will depend on the ratio between the radius of the perforation and side or radius of the perforation cell. The factor γ is plotted against $\eta'^2 \equiv r_0/(a_c/2)$ and a linear fit model of general form

$$f(x) = \beta_0 + \beta_1 x \tag{5.10}$$

was used to fit the data. The simulation was performed for $a = 400\ \mu m$, $a = 600\ \mu m$ and $a = 800\ \mu m$. For each case, $a_c \in \{40, 60, 80\}\ \mu m$ and, for each a_c, r_0 ranges from $10\ \mu m$ to $a_c/2 - 2.5\ \mu m$ in steps of $2.5\ \mu m$, e.g., for $a_c = 80\ \mu m$, $r_0 \in \{10, 12.5, 15, \ldots, 35, 37.5\}\ \mu m$.

A strong correlation is seen between γ and η'^2 which, within the values presented here, can be considered independent of the area of the membrane. The correction factor γ is defined by averaging the constants β_i for the different membranes, namely,

$$\gamma(\eta') \approx 1 - 0.78\eta'^2 \tag{5.11}$$

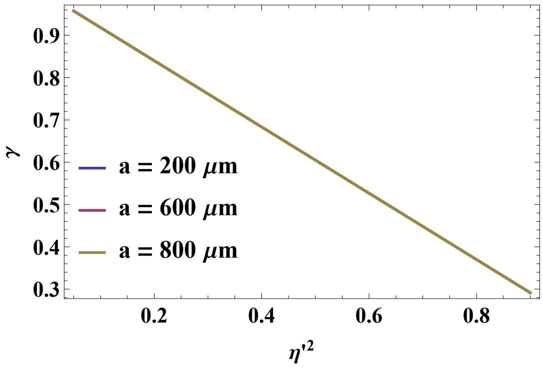

Figure 5.9: Effect of the perforated geometry on the maximum displacement of the membrane. Overlap of the fitted functions for the cases $a = 400\mu m$, $a = 600\mu m$ and $a = 800\mu m$ showing that γ is independent of the membrane's area, for the range of values presented. The values of $a_c/2$ are $20\ \mu m$, $30\ \mu m$ and $40\ \mu m$ and r_0 ranges over $10\ \mu m$ to $a_c/2 - 2.5\ \mu m$ with steps of $2.5\ \mu m$

The effect of the perforation density on the behaviour of the system is easily seen from the frequency spectrum of the oscillator (Figure 5.10). The resonance peak can be completely nullified while maintaining a constant deflection through the audible range provided that a good description of the damping force is known. It is emphasized that the modelling of the damping force for perforated geometries still

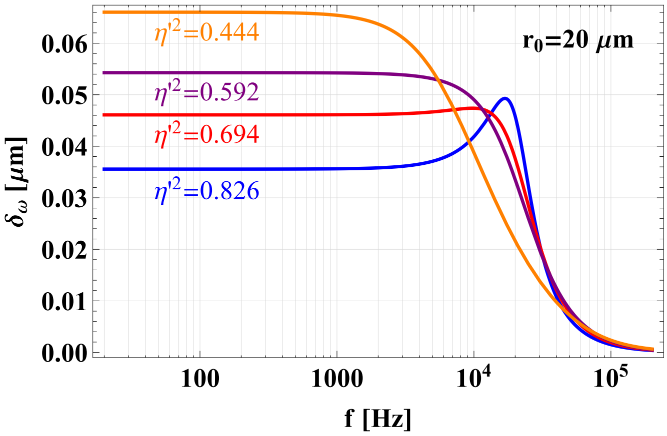

Figure 5.10: The effect of perforation density on the frequency spectrum of the oscillator for constant membrane area and thickness, electrostatic pressure and air gap height.

resorts to numerical methods to provide values with accuracy better than 15% (see discussion bellow).

5.3 Squeeze-film damping

Of every aspect of the problem, squeeze-film damping is by far the most difficult to model. Several models have been proposed in the literature to deal with perforated geometries. The problem can be broke down into different categories depending on the radius or length of the perforations, the air gap height or the pattern of the perforations. Pratap et al. [2007] consider three distinct regimes — 1) 2D lateral flow, adequate for thin perforations with small air gaps compared to the radius of the perforations; 2) 2D lateral flows plus 1D vertical flow, adequate for long perforations with an air gap much smaller than the radius of the perforations and 3) full 3D model for when all dimensions are of the same order of magnitude. Three phenomena are in the centre of this division — *Rarefaction*, *Compressibility* and *Inertia*.

Rarefaction Rarefaction occurs when the mean free path of the molecules of the gas starts to become of the same order of magnitude as the characteristic dimensions of the problem. Rarefaction is measured[3] by the *Knudsen Number*

$$\mathrm{Kn} = \frac{\lambda}{l_0} \tag{5.12}$$

where λ is the mean free path of the molecules of the gas ($\approx 0.064 \mu m$ for air at ambient conditions) and l_0 is the characteristic dimension. For $\mathrm{Kn} < 0.01$ continuum flow regime applies while for $\mathrm{Kn} > 1$ full molecular regime must be considered. For the presented devices the characteristic dimensions are the air gap height and the radius of the perforations. Considering an air gap of 5 μm and a radius of 10 μm, $\mathrm{Kn}_g \approx 0.013$ and $\mathrm{Kn}_h \approx 0.006$, respectively. Thus, full continuum regime can be applied for an air gap height greater than 5 μm but slip flow conditions might have to be taken into consideration for smaller air gaps. For the perforations full continuum flow can be used.

---

[3] In this context, measuring refers to the determination of considering or not the respective phenomena.

Compressibility Compressibility relates to the extent of compression of air in the air gap. If the air gap is too small or the frequency of actuation too high, the fluid will not be able to flow and it will compress. This is measured by the *squeeze number*, already introduced in Chapter 3, reproduced here for reference

$$\sigma = \frac{12\mu l_0^2 \omega}{P_a h_0^2} \tag{3.124}$$

Here the characteristic dimension of the problem, l_0, is the radius of the perforation cell, r_c. Compression of the film is an effect to be avoided. Not only it will change the resonance frequency of the system it will greatly increase its stiffness. If $\sigma > 1$ the compression of the film has to be taken into considerations, if $\sigma \ll 1$ then compression of the film can be ignored. Take the following example — a radius cell of 30 μm, an air gap of 2 μm and a driving frequency of 2 kHz correspond to $\sigma \approx 0.006 \ll 1$. These are typical values that represent the orders of magnitude to be used for each parameter. Thus, compression of the film can be ignored.

Inertia The effect of inertia is quickly dismissed in MEMS devices because of the very small volume displaced. Inertia is measured by the *Reynolds number*

$$\mathrm{Re} = \frac{\rho \omega l_0^2}{\mu} \tag{5.13}$$

where ρ is the density of air, μ is the viscosity of air, ω is the driving frequency and l_0 the characteristic dimension. If $\mathrm{Re} \ll 1$ inertia effects can be neglected, otherwise it has t be considerer. As in the case of compressibility both the air gap height and the perforations' radius are characteristic dimensions. Taking the same values used for compressibility and rarefaction, one gets $\mathrm{Re}_g \approx 0.02 \ll 1$ and $\mathrm{Re}_h \approx 0.08 \ll 1$, for the air gap and perforations, respectively. Therefore, inertia can be discarded.

This justifies the use of Bao's model in Chapter 3, however, three critical assumptions in this model must be noted — First, the motion of plates is independent of the reaction of the fluid, second, the amplitude of vibration is much smaller than the air gap height and third, the fluid in the perforations is a fully developed *Poiseuille* fluid. The first assumption greatly simplifies the problem and it is the most common assumption in analytical models (Nayfeh and Younis [2004]). This is a poor assumption however leading to lack of accuracy of the model, speciality for large deflections. The second assumption suits many MEMS applications, even loudspeakers, but large deflections (relative to the air gap) must be taken into account here for a practical application. Finally the third assumption doesn't account for losses at the perforations walls due to their roughness and irregular shape.

A good review of the present models in the literature can be found in Pratap et al. [2007]. Recently, Nigro et al. [2011] summarized the most up-to-date models, both analytical and numerical, also introducing their own, and compare them to experimental data available in the literature. Rectangular plates with perforation ratios up to 77% are compared. They show that analytical models are well suited for high perforation ratio although limited to regular geometries. Accurate modelling of squeeze-film damping in complex geometries still relies heavily in numerical methods under some set of assumptions.

Squeeze-film damping is a critical aspect in the design of the loudspeaker an extensive experimental data must be acquired for the particular structure under investigation if an accurate model is to develop.

5.4 Circuit analogy

For design purposes and quick analysis it is common practice to use an equivalent circuit to represent the resonator. As shown in Figure 3.12 the thin plate is substituted by an ideal spring k_0, a dash-pot c_d and an effective mass m_0. These are *lumped parameters*. Using the *conjugate power variables* (Force, Velocity) instead of (Voltage, Current) one may replace the elastic constant, the dash-pot and the effective mass by a capacitor C_M, a resistor Z_M and an inductor L_M (Senturia [2000]). The values of each component are

$$C_M = 1/k_0 \qquad Z_M = c_d \qquad L_M = m_0 \tag{5.14}$$

The "M" index indicates that these are the mechanical equivalent lumped parameters, or in another words, that they are valid in the mechanical energy domain. Because the problem of the loudspeaker involves conversion of energy between the electrical, mechanical and acoustic domain the system can be represented in any one of these domains to better model particular aspects of the problem (see for example Beranek [1954]). The electrostatic force arising from the parallel plate capacitor is better modelled by a current or voltage source and a *two-port capacitor* as illustrated in Figure 5.12 (Senturia [2000]). This is because the energy stored in the capacitor is a function of both the charge in the plates and the distance between the plates. This can be further simplified using standard linearization theory or evaluated numerically for an exact solution (Senturia [2000]). Such evaluation however falls beyond the scope of this work.

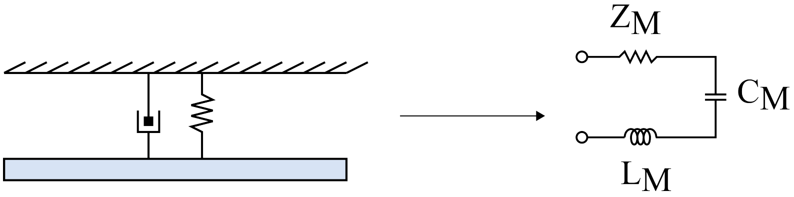

Figure 5.11: Equivalent circuit of the resonator. The dashpot is replaced by a resistor, the spring by a capacitor and the mass by an inductor.

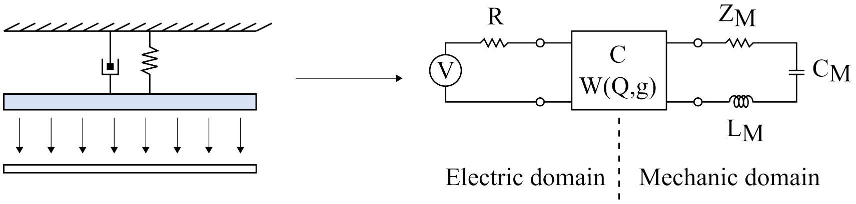

Figure 5.12: Equivalent circuit for the electric/mechanic domain of a electrostatic loudspeaker.

Figure 5.13 shows a possible model for the mechano-acoustical system (Neumann and Gabriel [2008], Beranek [1954]). The circuit is written in the acoustic domain using (Pressure (P), volume velocity (U)) as the conjugate power variables. The volume velocity is defined here as $U = vS$, where v is the particles' velocity amplitude and S is the cross-section area of the canal. The index "A" indicates that the acoustic domain is being used with

$$L_A = L_M/S^2 \qquad C_A = S^2 C_M \qquad Z_A = Z_M/S^2 \tag{5.15}$$

The values of Z_{bvA}, C_{bvA}, Z_{ecA} and C_{ecA} will depend on exterior conditions such as packaging or placement in the ear canal. The circuit is only valid if the pressure is being generated through all of the cross-section of the ear-canal, that is, the active area of the loudspeaker must be comparable to that of the cross-section of the ear canal. From the discussion above, its not reasonable to fabricate a single element with side or radius of the order of millimetres so a practical solution would involve arraying of single structures. The simplicity of this model allows the extraction of pertinent design rules — for instance, if the ear canal can be modelled as a pure spring, that is, $Z_{ecA} \to \infty$, then the design rule should be to minimize as much as possible the impedance to the left-side of the pressure generator so that P_{ear} is maximized. This means a very floppy, low mass membrane with a perforation ratio sufficiently high to allow the desire pressure to be achieved. Moreover, the amplitude of deflection becomes irrelevant in the design and the aim is to maximize the generated pressure. Using equation (3.139) pressures of 6 Pa can be achieved using just $V_{DC} = 1.8\ V$, $V_{AC} = 1.5\ V$ and $g'_0 = 2\mu m$. If this air leakage cannot be ignored the aim is to maximize the amplitude of vibration therefore maximizing the volume velocity and the pressure in the ear canal.

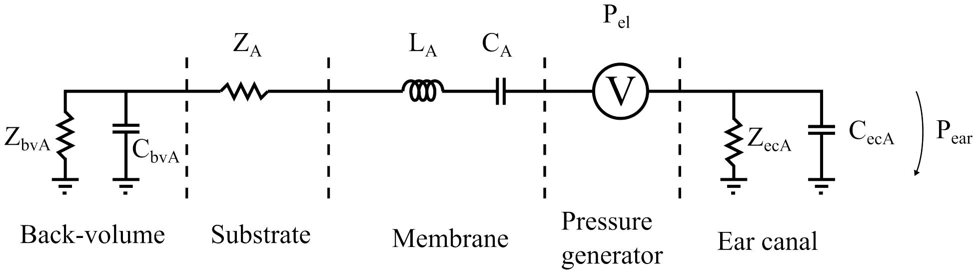

Figure 5.13: Possible circuit for mechano-acoustical model of the loudspeaker.

5.5 Conclusion

A general discussion on the proposed devices is provided here. There are several degree-of-freedom such as area, thickness, bias voltage or perforation density that can affect the overall behaviour of the system, each one of which playing a particular role. Through both theoretical and experimental data several conclusions are drawn setting guidelines for further investigation on the topic. It is clear that single structures with side or diameter of the order of millimetres are not straightforwardly realizable without fine optimization of the intrinsic stress of the a-Si:H structural layer. The same is valid for the thickness of such layer, where a narrow margin between 1 to 3 μm exists imposed by the technology. Extensive experimental data must be collected for different geometries in order to provide faithful information on non-linear parameters such as squeeze-film damping or electrostatic force in a large-deflection regime, together with the limitation imposed by the technology available.

Chapter 6

Conclusions

6.1 Achievements

The microfabrication process for an amorphous silicon electrostatic actuated loudspeaker for ultra low power consumption applications was presented. The proposed process allows different geometries compatible with a loudspeaker application and also introduce new concepts not yet present in the market or literature. Moreover typical materials in MEMS processing are used facilitating the transition to a possible production scale. The minimal dependence on the substrate also shows great promising for new trends such as processing on glass and flexible substrates.

Parallel to the process development a consistent theoretical description is provided including different aspects of the problem that will play a fundamental roll in the design and optimization of the loudspeaker. An initial experimental characterization is also provided showing the viability of the process, validating some presented theoretical elements, such as in-plane stress or voltage controlled resonance frequency, and also providing initial information on orders of magnitude of residual stress, dimensions feasibility or possible actuation voltage range.

Finally, a general discussion is provided considering both theoretical and experimental results providing a strong basis and general guidelines to further develop and optimize the loudspeaker performance.

6.2 Future Work

Future work must be set on fine-optimization of the fabrication thus providing a consistent and robust process. Namely, focusing on the amorphous silicon deposition and substrate DRIE is crucial for control of the mechanical properties of the membrane, reproducibility and high yields. Extensive experimental characterization on non-linear phenomena such as squeeze-film damping is also imperative, which will provide important data to model this crucial effect. The study of squeeze-film damping will certainly yield pertinent information not only for the particular application of a loudspeaker but also for many MEMS applications where perforations are present.

Feedback from acoustical measurements will also provide important information for further development and optimization and comparison of the performance of clamped vs suspended geometries.

Finally, double gate structure may also be consider which present some advantages such as a wider linear rage of actuation and lower actuation voltages required.

Appendix A

Runsheet example

A runsheet example is present here for the second generation process for the *clamped geometry*. Please refer to Chapter 2 for details.

Step	0. Substrate	**Performed by:**	NA	**Date:**	NA
Equipment	NA				
Substrate	2 by 1 inch intrinsic Si substrate; $<$100$>$ plane; 750 μm thick;				

Step	1. Lithography FS-AM	**Performed by:**		**Date:**	
Equipment	SVG/DWL				
Substrate	Si substrate (**Front-Side**)				

Conditions:	**Read / Comments:**
Coating: Standard coating - Program 6-2[1] **Exposure:** **Map:** BRES2 **Mask:** LS_AM **Energy:** 75 **Focus:** 50 **Align. offset:** (-19500,-13000) **Developing:** Standard developing - Program 6-2[2]	

Step	2. Lithography BS-AM	**Performed by:**		**Date:**	
Equipment	SVG/DWL				
Substrate	Si substrate (**Back-Side**)				

Conditions:	**Read / Comments:**
Coating: Standard coating - Program 6-2[3] **Exposure:** **Map:** BRES2 **Mask:** LS_AM **Energy:** 75 **Focus:** 50 **Align. offset:** (-19500,-13000) **Developing:** Standard developing - Program 6-2[4]	

Step	3. Substrate	**Performed by:**	NA	**Date:**	NA
Equipment	NA				
Substrate	2 by 1 inch intrinsic Si substrate; <100> plane; 750 μm thick; Alignment marks on both sides				

Step	4. Al_2O_3 PVD	**Performed by:**		**Date:**	
Equipment	UHV2				
Substrate	Si substrate (**Back-Side**)				

Conditions:	**Read / Comments:**
RF power: 200W; **Base Pressure:** ∼ 1E-7 Torr; **Pressure:** 3 mTorr; **Ar:** 50 sccm **Time:** 3h **Target thickness:** 2000 Å	

Step	5. Lithography BS-L1	**Performed by:**		**Date:**	
Equipment	SVG/DWL				
Substrate	Si substrate / 2000 Å Al_2O_3 (**Back-Side**)				

Conditions:	**Read / Comments:**
Coating: Standard coating - Program 6-2 **Exposure:** **Map:** BRES2 **Mask:** LS_RC_10_BS_L1_NI **Energy:** 75 **Focus:** 50 **Align. offset:** (0,0) **Developing:** Standard developing - Program 6-2	

Step	6. Al_2O_3 wet etch	**Performed by:**		**Date:**	
Equipment	Wet bench				
Substrate	Si substrate / 2000 Å Al_2O_3 / 1.5 μm PR (**Back-Side**)				

Conditions:	**Read / Comments:**
Media: Gravure Aluminium etchant; **Temperature:** 85 ° C; **Time:** 10 min; **Etch rate:** ∼ 33 Å/s **Cleaning:** Rinse with IPA + DI-water; Blow dry with compressed air.	

Step	7. Resist strip	**Performed by:**		**Date:**	
Equipment	Wet bench				
Substrate	Si substrate / 2000 Å Al_2O_3 / 1.5 μm PR (**Back-Side**)				

Conditions:	**Read / Comments:**
Media: Microstrip 3001; **Temperature:**65 ° C; **Time:** 15 min; **Cleaning:** Rinse with IPA + DI-water; Blow dry with compressed air.	

Step	8. Al_2O_3 PVD	**Performed by:**	**Date:**
Equipment	UHV2		
Substrate	Si substrate (**Front-Side**)		

Conditions:	**Read / Comments:**
RF power: 200W; **Base Pressure:** $\sim$ 1E-7 Torr; **Pressure:** 3 mTorr; **Ar:** 50 sccm **Time:** 3h **Target thickness:** 2000 Å	

Step	9. Lithography FS-L1	**Performed by:**	**Date:**
Equipment	SVG/DWL		
Substrate	Si substrate / 2000 Å Al_2O_3 (**Front-Side**)		

Conditions:	**Read / Comments:**
Coating: Standard coating - Program 6-2 **Exposure:** **Map:** BRES2 **Mask:** FS_RC_10_BS_L1_NI **Energy:** 75 **Focus:** 50 **Align. offset:** (900,0) **Developing:** Standard developing - Program 6-2	

Step	10. Al_2O_3 wet etch	**Performed by:**	**Date:**
Equipment	Wet bench		
Substrate	Si substrate / 2000 Å Al_2O_3 / 1.5 μm PR (**Front-Side**)		

Conditions:	**Read / Comments:**
Media: Gravure Aluminium etchant; **Temperature:** 85 $^\circ$ C; **Time:** 10 min; **Etch rate:** $\sim$ 33 Å/s **Cleaning:** Rinse with IPA + DI-water; Blow dry with compressed air.	Sample is placed on top of an adherent film to protect the back-side.

Step	11. Resist strip	**Performed by:**	**Date:**
Equipment	Wet bench		
Substrate	Si substrate / 2000 Å Al_2O_3 / 1.5 μm PR (**Front-Side**)		

Conditions:	**Read / Comments:**
Media: Microstrip 3001; **Temperature:**65 $^\circ$ C; **Time:** 15 min; **Cleaning:** Rinse with IPA + DI-water; Blow dry with compressed air.	

Step	12. Al PVD	**Performed by:**	**Date:**
Equipment	Nordiko 7000		
Substrate	Si substrate / 2000 Å Al_2O_3 (**Front-Side**)		

Conditions:	Read / Comments:
Sequence: Al 1500 A **RF power:** 2 kW; **Base Pressure:** ∼ 1E-8 Torr; **Pressure:** 3 mTorr; **Ar:** 50 sccm **Time:** 27s **Target thickness:** 1500 Å	

Step	13. Lithography FS-L2	**Performed by:**	**Date:**
Equipment	SVG/DWL		
Substrate	Si substrate / 2000 Å Al_2O_3 / 1500 Å Al (**Front-Side**)		

Conditions:	Read / Comments:
Coating: Standard coating - Program 6-2 **Exposure:** **Map:** BRES2 **Mask:** FS_RC_10_BS_L2_I **Energy:** 75 **Focus:** 50 **Align. offset:** (300,300) **Developing:** Standard developing - Program 6-2	

Step	14. Al_2O_3 wet etch	**Performed by:**	**Date:**
Equipment	Wet bench		
Substrate	Si substrate / 2000 Å Al_2O_3 / 1500 Å Al / 1.5 μm PR (**Front-Side**)		

Conditions:	Read / Comments:
Media: Gravure Aluminium etchant; **Temperature:** Room temperature; **Time:** 3-5 min; **Etch rate:** ∼ 8.3 Å/s **Cleaning:** Rinse with IPA + DI-water; Blow dry with compressed air.	

Step	15. Resist strip	**Performed by:**	**Date:**
Equipment	Wet bench		
Substrate	Si substrate / 2000 Å Al_2O_3 / 1500 Å Al / 1.5 μm PR (**Front-Side**)		

Conditions:	Read / Comments:
Media: Microstrip 3001; **Temperature:**65 ° C; **Time:** 15 min; **Cleaning:** Rinse with IPA + DI-water; Blow dry with compressed air.	

Step	16. SiO_2 PVD	**Performed by:**	**Date:**
Equipment	Alcatel		
Substrate	Si substrate / 2000 Å Al_2O_3 / 1500 Å Al (**Front-Side**)		

Conditions:	Read / Comments:
RF power: 140 kW; **Pressure:** 3 mTorr; **Ar:** 20 sccm **Time:** 25 min **Target thickness:** 500 Å	

Step	17. Lithography FS-L3	**Performed by:**	**Date:**
Equipment	SVG/DWL		
Substrate	Si substrate / 2000 Å Al_2O_3 / 1500 Å Al / 500 Å SiO_2 (**Front-Side**)		

Conditions:	**Read / Comments:**
Coating: Standard coating - Program 6-2 **Exposure:** **Map:** BRES2 **Mask:** FS_RC_10_BS_Al2O3_Pass_I **Energy:** 75 **Focus:** 50 **Align. offset:** (300,400) **Developing:** Standard developing - Program 6-2	

Step	18. SiO_2 RIE	**Performed by:**	**Date:**
Equipment	LAM		
Substrate	Si substrate / 2000 Å Al_2O_3 / 1500 Å Al / 500 Å SiO_2 / 1.5 μm PR (**Front-Side**)		

Conditions:	**Read / Comments:**
Recipe: CF4_O2_He; **Power:** 200 W; **Pressure:** 275 mTorr; **CF_4 flow:** 50 sccm; **O_2 flow:** 20 sccm; **He flow:** 100 sccm; **Time:** 50 s **Etch rate:** $\sim$ 20 Å/s	

Step	19. Resist strip	**Performed by:**	**Date:**
Equipment	Wet bench		
Substrate	Si substrate / 2000 Å Al_2O_3 / 1500 Å Al / 1.5 μm PR (**Front-Side**)		

Conditions:	**Read / Comments:**
Media: Microstrip 3001; **Temperature:**65 $^\circ$ C; **Time:** 15 min; **Cleaning:** Rinse with IPA + DI-water; Blow dry with compressed air.	

Step	20. Al_2O_3 PVD	**Performed by:**	**Date:**
Equipment	UHV2		
Substrate	Si substrate / 2000 Å Al_2O_3 / 1500 Å Al / 500 Å SiO_2 (**Front-Side**)		

Conditions:	**Read / Comments:**
RF power: 200W; **Base Pressure:** $\sim$ 1E-7 Torr; **Pressure:** 3 mTorr; **Ar:** 50 sccm **Time:** 3h **Target thickness:** 2000 Å	

Step	21. Lithography FS-L1	**Performed by:**	**Date:**
Equipment	SVG/DWL		
Substrate	Si substrate / 2000 Å Al_2O_3 / 1500 Å Al / 500 Å SiO_2 2000 Å Al_2O_3 (**Front-Side**)		

Conditions:	**Read / Comments:**
Coating: Standard coating - Program 6-2 **Exposure:** **Map:** BRES2 **Mask:** FS_RC_10_BS_L3_NI **Energy:** 75 **Focus:** 50 **Align. offset:** (300,400) **Developing:** Standard developing - Program 6-2	

Step	22. Al_2O_3 wet etch	**Performed by:**	**Date:**
Equipment	Wet bench		
Substrate	Si substrate / 2000 Å Al_2O_3 / 1500 Å Al / 500 Å SiO_2 2000 Å Al_2O_3 / 1.5 μm PR (**Front-Side**)		

Conditions:	**Read / Comments:**
Media: Gravure Aluminium etchant; **Temperature:** 85 ° C; **Time:** 10 min; **Etch rate:** $\sim$ 33 Å/s **Cleaning:** Rinse with IPA + DI-water; Blow dry with compressed air.	Sample is placed on top of an adherent film to protect the back-side.

Step	23. Resist strip	**Performed by:**	**Date:**
Equipment	Wet bench		
Substrate	Si substrate / 2000 Å Al_2O_3 / 1500 Å Al / 500 Å SiO_2 2000 Å Al_2O_3 / 1.5 μm PR (**Front-Side**)		

Conditions:	**Read / Comments:**
Media: Microstrip 3001; **Temperature:**65 ° C; **Time:** 15 min; **Cleaning:** Rinse with IPA + DI-water; Blow dry with compressed air.	

Step	24. SiO_2 PECVD	**Performed by:**	**Date:**
Equipment	Electrotech		
Substrate	Si substrate / 2000 Å Al_2O_3 / 1500 Å Al / 500 Å SiO_2 / 2000 Å Al_2O_3 (**Front-Side**)		

Conditions:	**Read / Comments:**
RF power: 430W; **Pressure:** $\sim$ 700 mTorr; **Shower head temp:** 350 ° C; **Substrate temp:** 300 ° C; **N_2 flow:** 2500 sccm; **SiH_4 flow:** 125 sccm; **Time:** 50s **Target thickness:** 1 μm **Measured thickness:**	

Step	25. Lithography FS-L4	**Performed by:**	**Date:**
Equipment	SVG/DWL		
Substrate	Si substrate / 2000 Å Al_2O_3 / 1500 Å Al / 500 Å SiO_2 / 2000 Å Al_2O_3 / 1 μm SiO_2 (**Front-Side**)		

Conditions:	Read / Comments:
Coating: Double coating - Program 6-2 / Program 6-2 **Exposure:** **Map:** BRES2 **Mask:** FS_RC_10_BS_L4_NI **Energy:** 75 **Focus:** 50 **Align. offset:** (300,400) **Developing:** Standard developing - Program 6-2 / +60s on developer	

Step	26. SiO_2 RIE	**Performed by:**	**Date:**
Equipment	LAM		
Substrate	Si substrate / 2000 Å Al_2O_3 / 1500 Å Al / 500 Å SiO_2 / 2000 Å Al_2O_3 / 1 μm SiO_2 / 2.6 μm PR (**Front-Side**)		

Conditions:	Read / Comments:
Recipe: CF4_O2_He_3step; **Power:** 200 W; **Pressure:** 275 mTorr; **CF_4 flow:** 50 sccm; **O_2 flow:** 20 sccm; **He flow:** 100 sccm; **Time:** 3 steps 200s with 25s cool down **Etch rate:** ~ 20 Å/s	

Step	27. Resist strip	**Performed by:**	**Date:**
Equipment	Wet bench		
Substrate	Si substrate / 2000 Å Al_2O_3 / 1500 Å Al / 500 Å SiO_2 / 2000 Å Al_2O_3 / 1 μm SiO_2 / 1.5 μm PR (**Front-Side**)		

Conditions:	Read / Comments:
Media: Microstrip 3001; **Temperature:**65 ° C; **Time:** 1 hour; **Cleaning:** Rinse with IPA + DI-water; Blow dry with compressed air.	

Step	28. O_2 plasma cleaning	**Performed by:**	**Date:**
Equipment	LAM		
Substrate	Si substrate / 2000 Å Al_2O_3 / 1500 Å Al / 500 Å SiO_2 2000 Å Al_2O_3 / 1 μm SiO_2 (**Front-Side**)		

Conditions:	Read / Comments:
Recipe: O2_plasma_2step; **Power:** 400 W; **Pressure:** 275 mTorr; **O_2 flow:** 20 sccm; **Time:** 2 steps 300s with 25s cool down **Etch rate:** ~ -	

Step	29. a−Si:H/n^+ PECVD	**Performed by:**	**Date:**
Equipment	CVD system		
Substrate	Si substrate / 2000 Å Al_2O_3 / 1500 Å Al / 500 Å SiO_2 / 2000 Å Al_2O_3 / 1 μm SiO_2 (**Front-Side**)		

Conditions:

Read / Comments:

RF power: 25W; **Pressure:** $\sim$ 1 Torr; **Substrate temp:** 150 °C;
H_2 flow: 28 sccm; **SiH_4 flow:** 7 sccm; **PH_3 flow:** 3.5 sccm; **Time:** 2h15min
Target thickness: 3 μm
Measured thickness:

Step 30. Al PVD **Performed by:** **Date:**
Equipment Nordiko 7000
Substrate Si substrate / 2000 Å Al_2O_3 / 1500 Å Al / 500 Å SiO_2 / 2000 Å Al_2O_3 / 1 μm SiO_2 / 3 μm a$-$Si.H/n$^+$ (**Front-Side**)

Conditions:

Read / Comments:

Sequence: Al 1500 A
RF power: 2 kW; **Base Pressure:** $\sim$ 1E-8 Torr; **Pressure:** 3 mTorr;
Ar: 50 sccm **Time:** 27s
Target thickness: 1500 Å

Step 31. Lithography FS-L5 **Performed by:** **Date:**
Equipment SVG/DWL
Substrate Si substrate / 2000 Å Al_2O_3 / 1500 Å Al / 500 Å SiO_2 / 2000 Å Al_2O_3 / 1 μm SiO_2 / 3 μm a$-$Si.H/n$^+$ / 1500 Å Al (**Front-Side**)

Conditions:

Read / Comments:

Coating:
Double coating - Program 6-2 / Program 6-2
Exposure:
Map: BRES2 **Mask:** FS_RC_10_BS_L5_NI **Energy:** 75 **Focus:** 50
Align. offset: (300,400)
Developing:
Standard developing - Program 6-2 / +60s on developer

Step 32. Al_2O_3 wet etch **Performed by:** **Date:**
Equipment Wet bench
Substrate Si substrate / 2000 Å Al_2O_3 / 1500 Å Al / 500 Å SiO_2 / 2000 Å Al_2O_3 / 1 μm SiO_2 / 3 μm a$-$Si.H/n$^+$ / 1500 Å Al / 2.6 μm PR (**Front-Side**)

Conditions:

Read / Comments:

Media: Gravure Aluminium etchant; **Temperature:** Room temperature;
Time: 3-5 min;
Etch rate: $\sim$ 8.3 Å/s
Cleaning: Rinse with IPA + DI-water; Blow dry with compressed air.

Step 33. a$-$Si:H/n$^+$ RIE **Performed by:** **Date:**
Equipment LAM
Substrate Si substrate / 2000 Å Al_2O_3 / 1500 Å Al / 500 Å SiO_2 / 2000 Å Al_2O_3 / 1 μm SiO_2 / 3 μm a$-$Si:H/n$^+$ / 1500 Å Al / 2.6 μm PR (**Front-Side**)

Conditions:	Read / Comments:
Recipe: SF6_CHF3_2step; **Power:** 200 W; **Pressure:** 100 mTorr; **SF_6 flow:** 50 sccm; **CHF_3 flow:** 50 sccm; **Time:** 2 steps 400s with 60s cool down **Etch rate:** $\sim$ 5 nm/s a$-$Si:H/n$^+$ / $\sim$ 1.7 nm/s TiW	

Step 34. Resist strip **Performed by:** **Date:**
Equipment Wet bench
Substrate Si substrate / 2000 Å Al_2O_3 / 1500 Å Al / 500 Å SiO_2 / 2000 Å Al_2O_3 / 1 μm SiO_2 / 3 μm a$-$Si:H/n$^+$ / 1500 Å Al / 2.6 μm PR (**Front-Side**)

Conditions:	Read / Comments:
Media: Microstrip 3001; **Temperature:**65 ° C; **Time:** 1 hour; **Cleaning:** Rinse with IPA + DI-water; Blow dry with compressed air.	

Step 35. O_2 plasma cleaning **Performed by:** **Date:**
Equipment LAM
Substrate Si substrate / 2000 Å Al_2O_3 / 1500 Å Al / 500 Å SiO_2 / 2000 Å Al_2O_3 / 1 μm SiO_2 / 3 μm a$-$Si:H/n$^+$ / 1500 Å Al (**Front-Side**)

Conditions:	Read / Comments:
Recipe: O2_plasma_2step; **Power:** 400 W; **Pressure:** 275 mTorr; **O_2 flow:** 20 sccm; **Time:** 2 steps 300s with 25s cool down **Etch rate:** -	

Step 36. Substrate DRIE **Performed by:** **Date:**
Equipment SPTS Pegasus (INL)
Substrate Si substrate / 2000 Å Al_2O_3 (**Back-Side**)

Conditions:	Read / Comments:
Recipe: INL Complex HF **Etching step:** **Pressure:** 100 mTorr **Coil Power:** 2.8 kW **Platten Power:** 40 kW HF **SF_6:** 450 sccm **O_2:** 45 sccm **Time/cycle:** 7s **Passivation step:** **Pressure:** 25 mTorr **Coil Power:** 2 kW **Platten Power:** 0 kW **SF_6:** 0 sccm **O_2:** 200 sccm **Time/cycle:** 4s	

Step	37. Dicing	**Performed by:**	**Date:**
Equipment	Dicing saw		
Substrate	Si substrate / 2000 Å Al_2O_3 / 1500 Å Al / 500 Å SiO_2 / 2000 Å Al_2O_3 / 1 μm SiO_2 / 3 μm a$-$Si:H/n$^+$ / 1500 Å Al		

Conditions:	**Read / Comments:**
Die size: 6.5 mm^2 $\times$ 6.5 mm^2 **Rows:** 2 **Columns:** 6	

Step	38. HF VPE	**Performed by:**	**Date:**
Equipment	Primaxx (INL)		
Substrate	Si substrate / 2000 Å Al_2O_3 / 1500 Å Al / 500 Å SiO_2 / 2000 Å Al_2O_3 / 1 μm SiO_2 / 3 μm a$-$Si:H/n$^+$ / 1500 Å Al (**Front-Side**)		

Conditions:	**Read / Comments:**
Recipe: INL2 **Cycles:** 3	

Appendix B

Extended Hamiltonian principle

B.1 Governing equation for a two dimensional system with one dependent variable

The discussion presented here follows closely the one in Magrab [2012] where a thorough mathematical description of the subject can be found.

In its most general form, a physical system can be described by the Hamilton principle which states that the path of motion taken by a system between two instants of time, t_1 and t_2, corresponds to an extremum of the integral

$$I = \int_{t_1}^{t_2} L(t)\, dt \tag{B.1}$$

where $L(t)$ is known as the Lagrangian of the system given by (for the cases studied here)

$$L(t) = T(t) - U(t) + W(t) \tag{B.2}$$

where $T(t)$ is the kinetic energy of the system, $U(t)$ is the potential energy of the system and $W(t)$ is the external non conservative work performed on the system. In what is referred as the *extended Hamilton's principle*, for a system with one dependent variable $w(x, y, t)$, it is assumed that L can be expressed as

$$L = \iint_R F dxdy + F^{(C_1)} + F^{(C_2)} \tag{B.3}$$

where

$$\begin{aligned} F &= F(x, y, w, \dot{u}, w_{,x}, w_{,y}, w_{,xx}, u_{,xy}, w_{,yy}) \\ F^{(C1)} &= F^{(C1)}(x, y, t, w(C_1), \dot{w}(C_1), w_{,x}(C_1), \dot{w}_{,x}(C_1)) \\ F^{(C2)} &= F^{(C2)}(x, y, t, w(C_2), \dot{w}(C_2), w_{,y}(C_2), \dot{w}_{,y}(C_2)) \end{aligned}$$

with

$$\dot{w} = \frac{\partial w}{\partial t} \quad w_{,\alpha} = \frac{\partial w}{\partial \alpha} \quad w_{,\alpha\beta} = \frac{\partial^2 w}{\partial \alpha \partial \beta} \quad \dot{w}_{\alpha} = \frac{\partial \dot{w}}{\partial \alpha} = \frac{\partial^2 w}{\partial t \partial \beta}$$

$$\alpha = x, y \qquad \beta = x, y$$

where R is the two-dimensional region, delimited by the boundary C $(C_1 + C_2)$, where the system is described. The function F is called the minimization function and can be viewed as the Lagrangian for an infinitesimal volume of the system and the functions $F^{(C_1)}$ and $F^{(C_2)}$ are the difference between the kinetic and potential energy of the elements attached to the boundaries C_1 and C_2, respectively. The discussion is restricted to a region of rectangular form and symmetric quadratic functions F, $F^{(C_1)}$ and $F^{(C_2)}$. Although these are somewhat strong restrictions they will prove to be sufficient for the cases studied here.

The condition for B.1 to be an extremum yields the governing equation (Magrab [2012], Appendix B)

$$F_w - \frac{\partial F_{w,x}}{\partial x} - \frac{\partial F_{w,y}}{\partial y} + \frac{\partial^2 F_{w,xx}}{\partial x^2} + \frac{\partial^2 F_{w,yy}}{\partial y^2} + \frac{\partial^2 F_{w,xy}}{\partial x \partial y} - \frac{\partial F_{\dot{w}}}{\partial t} = 0 \tag{B.4}$$

where $F_\alpha \equiv \frac{\partial F}{\partial \alpha}$ with $\alpha \in \{w, \dot{w}, w_{,x}, ...\}$. Equation B.4 is known as the *Euler-Lagrange equation*.

At the boundary C it must fulfill the condition

$$B_C(u(x,y,t), u(x,y,t)) = 0 \tag{B.5}$$

where

$$\begin{aligned} B_C(w(x,y,t), w(x,y,t)) & \\ =& \sum_{j=1}^{2} w(x_j,y,t) \left[H_3(w(x_j,t),1) + (-1)^j H_1(x,y,j) \Delta y \right] \\ &+ \sum_{j=1}^{2} w_{,x}(x_j,y,t) \left[H_3(w_{,x}(x_j,t),1) + (-1)^j H_2(x,y) \Delta y \right] \\ &+ \sum_{j=1}^{2} w(x,y_j,t) \left[H_3(w(y_j,t),2) + (-1)^{j-1} H_1(y,x,j) \Delta x \right] \\ &+ \sum_{j=1}^{2} w_{,y}(x,y_j,t) \left[H_3(w_{,y}(y_j,t),2) + (-1)^j H_2(y,j) \Delta x \right] \end{aligned} \tag{B.6}$$

with

$$\begin{aligned} H_1(\gamma,\beta,j) &= \left[F_{w,\gamma} - \frac{\partial F_{w,\gamma\gamma}}{\partial \gamma} - \frac{\partial F_{w,\gamma\beta}}{\partial \beta} \right]_{\gamma=\gamma_j} \\ H_2(\gamma,j) &= F_{w,\gamma\gamma}|_{\gamma=\gamma_j} \\ H_3(\alpha,l) &= F_\alpha^{(C_l)} - \frac{\partial F_{\dot{\alpha}}^{(C_l)}}{\partial t} \end{aligned}$$

Condition B.5 represent the general form of the typical pinned, clamped, hinged or free conditions including already the boundary attachments.

Appendix C

Deformation of linear isotropic elastic solids

C.1 Introduction

An introduction to the topic of linear isotropic elastic deformation is presented here. A complete description on the subject can be found at Sadd [2009], Timoshenko [1951] or Landau et al. [1986].

The strain tensor The deformation of a solid is described through its displacement field, $\mathbf{u}$, defined as the difference between the current or final state of deformation and some reference state, for all *particles*[1] within the solid. In symbolic notation, this is written as

$$\mathbf{u}(\mathbf{X}) = \mathbf{x}(\mathbf{X}) - \mathbf{X} \tag{C.1}$$

where, $\mathbf{x}$ is the current position vector of some particle and X is the position vector of that particle in the reference state. It is emphasized that both the displacement field $\mathbf{u}$ and the current position $\mathbf{x}$ of all particles are smooth and continuous functions of the coordinate of those particles in the reference state. It is shown (see for example Landau et al. [1986]) that the change in length of an infinitesimal element in the reference state is related to its initial length by
which can be further simplified to

$$dx^2 = dX^2 + \sum_{i,k} 2e_{ik} dx_i dx_k \tag{C.2}$$

where dx is the new length of the elements, dX is the initial length of the elements and

$$e_{ik} = \frac{1}{2}\left(\frac{\partial u_i}{\partial x_k} + \frac{\partial u_k}{\partial x_i} + \frac{\partial u_l}{\partial x_i}\frac{\partial u_l}{\partial x_k}\right) \tag{C.3}$$

---

[1] A *particle*, in the sense of continuum mechanics, is an infinitesimal volume compared to the total size of the solid but large enough that many actual *physical* particle are present therein.

is known as the *stain tensor*. In small deformation theory only first order terms of the displacement field are considered and the strain tensor (C.3) is further simplifies to

$$e_{ik} = \frac{1}{2}\left(\frac{\partial u_i}{\partial x_k} + \frac{\partial u_k}{\partial x_i}\right) \tag{C.4}$$

or explicitly

$$\mathbf{e}_{ik} = \begin{bmatrix} e_x & e_{xy} & e_{xz} \\ e_{yx} & e_y & e_{yz} \\ e_{zx} & e_{zy} & e_z \end{bmatrix} \tag{C.5}$$

Note that the strain tensor has a natural symmetric form and only six components are necessary to fully describe the deformation. For large deformations a careful distinction must be made between the *Eulerian* and *Lagrangian* formulation (see for example Chandrasekharaiah and Debnath [1994] or Mase and Mase [2010]). For small deformations however, such distinction can be dropped.

For small deformations the relative elongation the element dX can be computed as

$$\frac{\mathrm{d}x - \mathrm{d}X}{\mathrm{d}X} = \mathbf{N} \cdot \mathbf{e_{ik}} \cdot \mathbf{N} \tag{C.6}$$

where the vector $\mathbf{N}$ is the unitary vector along the direction of $d\mathbf{x}$. In particular, if the element $\mathbf{dx}$ is parallel to one of the frame's axis such that $d\mathbf{x} = dx\mathbf{e}_\alpha$, with $\alpha \in \{1, 2, 3\}$, then equation C.6 simplifies to

$$\frac{dx - dX}{dX} = \mathbf{e}_\alpha \cdot \mathbf{u_{ik}} \cdot \mathbf{e}_\alpha = e_\alpha \tag{C.7}$$

So the relative elongation of an element initially along one of the direction of the frame's axis gives directly the corresponding component of the strain tensor.

The stress tensor When the solid is subjected to an external load it will deform and induce a distribution of internal continuous forces counteracting this external load. If $\mathbf{f}$ represent the force per unit volume acting on the body, the total force acting on it, $\mathbf{F}$, is represented by the integral of $\mathbf{f}$ over the volume of the body, that is,

$$\mathbf{F} = \iiint_V \mathbf{f} dV \tag{C.8}$$

From Newton's third law, the resulting force inside the body must vanish. The total force acting on the body can therefore be described solely by the surrounding forces acting on the boundary of the body. From *Gauss's theorem* the integral of a scalar over a volume can be expressed as an integral over the surface bounding that volume if that scalar can be expressed as the divergence of some vector. This way, the force per unit volume $\mathbf{f}$ must be expressed as the divergence of a second-rank tensor, that is, the components of $\mathbf{f}$ are given by

$$f_i = \sum_k \partial\sigma_{ik}/\partial x_k \tag{C.9}$$

and

$$F_i = \iiint_V f_i dV = \sum_k \iiint_V \partial\sigma_{ik}/\partial x_k dV = \sum_k \oint_S \sigma_{ik} n_k dS \tag{C.10}$$

where $\mathbf{n}$ is the vector normal to the infinitesimal area element dS and σ_{ik} is the *stress tensor*, explicitly

$$\sigma_{ik} = \begin{bmatrix} \sigma_x & \sigma_{xy} & \sigma_{xz} \\ \sigma_{yx} & \sigma_y & \sigma_{yz} \\ \sigma_{zx} & \sigma_{zy} & \sigma_z \end{bmatrix} \tag{C.11}$$

So the force acting on an infinitesimal area element dS is given directly from the stress tensor as $dF_i = \sigma_{ik} n_k dS$. It is shown that the stress tensor also has a natural symmetric form.

Energy of deformation and Hooke's law For linear elastic materials the stress components are given by a linear, unique function of the strain components, usually expressed by a fourth-rank tensor C_{ijkm}, namely

$$\sigma_{ij} = \sum_{k,m} C_{ijkm} e_{km} \tag{C.12}$$

Imposing the symmetric condition on the stress and strain tensors the general form a fourth-rank isotropic tensor is given by

$$C_{ijkm} = \lambda \delta_{ij} \delta_{km} + \mu(\delta_{ik}\delta_{jm} + \delta_{im}\delta_{jk}) \tag{C.13}$$

and equation (C.12) is written as

$$\sigma_{ij} = \lambda \delta_{ij}(e_1 + e_2 + e_3) + 2\mu e_{ij} \tag{C.14}$$

which is known as the *generalized Hooke's law*. The parameters λ and μ are the *Lamé constants*. This relation can also be written using the *Young's modulus* E and the *Poisson ration* ν,

$$\epsilon_{ij} = \frac{1}{E}\left[(1+\nu)\sigma_i j - \nu \delta_{ij} \sigma_{kk}\right] \tag{C.15}$$

where

$$E = \frac{\mu(3\lambda + 2\mu)}{\lambda + \mu} \qquad \text{and} \qquad \nu = \frac{\lambda}{2(\lambda + \mu)} \tag{C.16}$$

Under the above mentioned assumptions the *strain energy* stored in the deformation of a body is given by

$$U_p = \frac{1}{2} \iiint_V \epsilon_{ij} \sigma_{ij} \, dV \tag{C.17}$$

where V is the volume of the solid. The kinetic energy is given directly from classic mechanics as

$$T_\rho = \frac{1}{2} \rho \iiint_V \dot{\mathbf{u}}^2 \, dV \tag{C.18}$$

where it is assumed that the mass density, ρ, is constant throughout the solid.

Appendix D

Thin plates

D.1 Coefficient appearing in equation (3.78)

The matrices appearing in equation (3.78) are organized as follows

$$\begin{bmatrix} C_{1111} & C_{1211} & \cdots & C_{1N11} & C_{2111} & C_{2211} & \cdots & C_{2N11} & \cdots & C_{N111} & C_{N211} & \cdots & C_{NN11} \\ \vdots & \vdots & & & & & & & & & & & \vdots \\ C_{111N} & C_{121N} & & & & & \cdots & & & & & & C_{NN1N} \\ \vdots & \vdots & & & & & & & & & & & \vdots \\ C_{11N1} & C_{12N1} & & & & & \cdots & & & & & & C_{NNN1} \\ \vdots & \vdots & & & & & & & & & & & \vdots \\ C_{11NN} & C_{12NN} & & & & & \cdots & & & & & & C_{NNNN} \end{bmatrix} \begin{Bmatrix} A_{11} \\ \vdots \\ A_{1N} \\ \vdots \\ A_{N1} \\ \vdots \\ A_{NN} \end{Bmatrix} \tag{D.1}$$

Matrix $[B]$ is the organized as matrix $[C]$ but with different values, namely,

$$\begin{aligned} B_{nmlk} =& I_{1nl} I_{2mk} \\ C_{nmlk} =& I_{5nl} I_{2mk} + I_{1nl} I_{6mk} + 2(1-\nu) I_{3nl} I_{4mk} + \nu (I_{7ln} I_{8km} + I_{7nl} I_{8mk}) \end{aligned} \tag{D.2}$$

with

$$\begin{aligned} I_{1np} &= \int_0^1 X_n(\eta) X_p(\eta) d\eta & I_{2mq} &= \int_0^1 Y_m(\xi) Y_q(\xi) d\xi \\ I_{3np} &= \int_0^1 X_n'(\eta) X_p'(\eta) d\eta & I_{4mq} &= \int_0^1 Y_m'(\xi) Y_q'(\xi) d\xi \\ I_{5np} &= \int_0^1 X_n''(\eta) X_p''(\eta) d\eta & I_{6mq} &= \int_0^1 Y_m''(\xi) Y_q''(\xi) d\xi \\ I_{7np} &= \int_0^1 X_n''(\eta) X_p(\eta) d\eta & I_{8mq} &= \int_0^1 Y_m''(\xi) Y_q(\xi) d\xi \end{aligned} \tag{D.3}$$

This page was intentionally left blank.

Bibliography

P. Alpuim, V. Chu, and J. P. Conde. Amorphous and microcrystalline silicon films grown at low temperatures by radio-frequency and hot-wire chemical vapor deposition. *Journal of Applied Physics*, 86(7): 3812–3821, 1999.

F. L. Ayatollahi and B. Y. Majlis. Materials design and analysis of low-power mems microspeaker using magnetic actuation technology. *Adv. Mater. Res.*, 74:243–246, 2009.

M.H. Bao. *Analysis And Design Principles Of Mems Devices*. Elsevier Science Limited, 2005.

Minhang Bao and Heng Yang. Squeeze film air damping in MEMS. *Sensors and Actuators A: Physical*, 136:3–27, 2007.

Minhang Bao, Heng Yang, Yuancheng Sun, and Paddy J. French. Modified reynolds' equation and analytical analysis of squeeze-film air damping of perforated structures. *Journal of Micromechanics and Microengineering*, 13:795–800, 2003.

L.L. Beranek. *Acoustics*. McGraw-Hill, 1954.

J. Bergqvist and F. Rudolf. A silicon condenser microphone using bond and etch-back technology. *Sensors and Actuators A: Physical*, 45:115–124, 1994.

B. Bhushan. *Springer Handbook of Nanotechnology*. Springer, 2004.

J.J. Blech. *On Isothermal Squeeze Films*. Energy Engineering Center, 1982.

Jérémie Bouchaud. Mems microphones make noise in 2012, January 2012. URL `http://www.electroiq.com/articles/stm/2012/01/mems-microphones-make-noise-in-2012.html`.

D.S. Chandrasekharaiah and L. Debnath. *Continuum mechanics*. Academic Press, 1994.

Y. C. Chen and Y. T. Cheng. A low-power milliwatt electromagnetic microspeaker using a PDMS membrane for hearing aids application. In *Micro Electro Mechanical Systems (MEMS), 2011 IEEE 24th International Conference on*, 2011.

M. C. Cheng, W. S. Huang, and S. R. S. Huang. A silicon microspeaker for hearing instruments. *Journal of Micromechanics and Microengineering*, 14(7):859, 2004.

Il-Joo Cho, Seongsoo Jang, and Hyo Jin Nam. A piezoelectrically actuated mems speaker with polyimide membrane and thin film pb(zr,ti)o3(pzt) actuator. *Integrated Ferroelectrics*, 105(105):27–36, 2009.

A.N. Cleland. *Foundations of Nanomechanics: From Solid-State Theory to Device Applications*. Springer, 2003.

A. Dehé. Silicon microphone development and application. *Sensors and Actuators A: Physical*, 133(2): 283–287, 2007.

Dr. Richard Dixon. Mems microphones break design mould, April 2006. URL `http://www.memsjournal.com/2006/04/mems_microphone.html`.

St. J. Dixon-Warren. Overview of mems microphone technologies for consumer applications, March 2011. URL `http://www.memsjournal.com/2011/03/overview-of-mems-microphone-technologies-for-consumer-applications.html`.

Albert Einstein. The Foundation of the General Theory of Relativity. *Annalen Phys.*, 49:769–822, 1916.

S. Franssila. *Introduction to Microfabrication*. Wiley, 2004.

J. Gaspar, V. Chu, and J. P. Conde. Electrostatic actuation of thin-film microelectromechanical structures. *Journal of applied physics*, 93(12):10018–10029, 2003.

J. Gaspar, A. Gualdino, B. Lemke, O. Paul, V. Chu, and J. P. Conde. Mechanical and piezoresistive properties of thin silicon films deposited by plasma-enhanced chemical vapor deposition and hot-wire chemical vapor deposition at low substrate temperatures. *Journal of Applied Physics*, 112:024906, 2012.

M. Goto, Y. Iguchi, K. Ono, A. Ando, F. Takeshi, S. Matsunaga, Y. Yasuno, K. Tanioka, and T. Tajima. High-performance condenser microphone with single-crystalline silicon diaphragm and backplate. *Sensors Journal, IEEE*, 7(1):4 –10, 2007.

D.J. Griffiths. *Introduction to Electrodynamics*. Pearson Education, Limited, 2012.

W. A. Gross, I. A. Matsch, A. Eshell V. Castelli, J. H. Vohr, and M. Wildmann. *Fluid Film Lubrification*. John Wiley & Sons, 1980.

A Gualdino, V Chu, and JP Conde. Pressure effects on the dynamic properties of hydrogenated amorphous silicon disk resonators. *Journal of Micromechanics and Microengineering*, 22:085026, 2012.

Dewey H Hodges. Proper definition of curvature in nonlinear beam kinematics. *AIAA journal*, 22(12): 1825–1827, 1984.

P.-C. Hsu, C.H. Mastrangelo, and K.D. Wise. A high sensitivity polysilicon diaphragm condenser microphone. In *Micro Electro Mechanical Systems, 1998. MEMS 98. Proceedings., The Eleventh Annual International Workshop on*, pages 580 –585, jan. 1998.

C. H. Huang, C. H. Lee, T. M. Hsieh, L. C. Tsao, S. Wu, J. C. Liou, M. Y. Wang, L. C. Chen, M. C. Yip, and W Fang. Implementation of the cmos mems condenser microphone with corrugated metal diaphragm and silicon back-plate. *Sensors*, 11(6):6257–69, 2011.

S. S. Je, F. Rivas, R. E. Diaz, J. Kwon, J. Kim, B. Bakkaloglu, S. Kiaei, and J. Chae. A compact and low-cost MEMS loudspeaker for digital hearing aids. *Biomedical Circuits and Systems, IEEE Transactions on*, 3(5):348–358, 2009.

Sang-Soo Je and Junseok Chae. A compact, low-power, and electromagnetically actuated microspeaker for hearing aids. *Electron Device Letters, IEEE*, 29(8):856 –858, aug. 2008.

H. Kim, A.A. Astle, K. Najafi, L.P. Bernal, P.D. Washabaugh, and F. Cheng. Bi-directional electrostatic microspeaker with two large-deflection flexible membranes actuated by single/dual electrodes. In *Sensors, 2005 IEEE*, page 4 pp., 30 2005-nov. 3 2005.

Hye Jin Kim, Kunmo Koo, Sung Q Lee, Kang-Ho Park, and Jongdae Kim. High performance piezoelectric microspeakers and thin speaker array system. *ETRI Journal*, 31(6):680–687, 2009.

Sangpyeong Kim, Xu Zhang, R. Daugherty, E. Lee, G. Kunnen, D.R. Allee, E. Forsythe, and Junseok Chae. Microelectromechanical systems (mems) based-ultrasonic electrostatic actuators on a flexible substrate. *Electron Device Letters, IEEE*, 33(7):1072 –1074, july 2012.

Sang Choon Ko, Yong Chul Kim, and Seung Seob Lee. Micromachined piezoelectric membrane acoustic device. *Sensors and Actuators A*, 103:1330–134, 2003.

L.L.D. Landau, E.M. Lifshitts, A.M. Kosevitch, and L.P. Pitaevskiĭ. *Theory of Elasticity 7*. Butterworth-Heinemann, 1986.

Seung S. Lee and Richard M. White. Piezoelectric cantilever voltage-to-frequency converter. *Sensors and Actuators A: Physical*, 71:153–157, 1998.

G. Lemarquand, R. Ravaud, I. Shahosseini, V. Lemarquand, J. Moulin, and E. Lefeuvre. Mems electrodynamic loudspeakers for mobile phones. *Applied Acoustics*, 73(4):379 – 385, 2012a.

V. Lemarquand, G. Lemarquand, E. Lefeuvre, I. Shahosseini, R. Ravaud, J. Moulin, M. Woytasik, E. Martinsic, and G. Pillonnet. Electrodynamic MEMS: application to mobile phone loudspeakers. *Magnetics, IEEE Transactions on*, 48(11):3684 –3687, 2012b.

Xinxin Li, Rongming Lin, Huatsoon Kek, Jianmin Miao, and Quanbo Zou. Sensitivity-improved silicon condenser microphone with a novel single deeply corrugated diaphragm. *Sensors and Actuators A: Physical*, 92:257–262, 2001.

Robert John Littrell. *High Performance Piezoelectric MEMS Microphones*. PhD thesis, The University of Michigan, 2010.

M.J. Madou. *Fundamentals of Microfabrication: The Science of Miniaturization*. Taylor & Francis, 2002.

E.B. Magrab. *Vibrations of Elastic Systems: With Applications to MEMS and NEMS*. Springer, 2012.

G.T. Mase and G.E. Mase. *Continuum Mechanics for Engineers*. Taylor & Francis, second edition, 2010.

C.H. Mastrangelo and C.H. Hsu. Mechanical stability and adhesion of microstructures under capillary forces. i. basic theory. *Microelectromechanical Systems, Journal of*, 2(1):33 –43, mar 1993.

Jianmin Miao, Rongming Lin, Longqing Chen, Quanbo Zou, Sin Yee Lim, and Suan Hee Seah. Design considerations in micromachined silicon microphones. *Microelectronics Journal*, 33:21–28, 2002.

Ronald N. MILES. Surface micromachined differential microphone. Patent, 08 2011. URL `http://www.patentlens.net/patentlens/patent/US_7992283/en/`. US 7992283.

P. M. Morse. *Vibration and Sound*, page 333. McGraw-Hill Bokk Company, 2nd edition edition, 1948.

P.M.C. Morse and K.U. Ingard. *Theoretical Acoustics*. McGraw-Hill, 1968.

Ali H. Nayfeh and Mohammad I. Younis. A new approach to the modeling and simulation of flexible microstructures under the effect of squeeze-film damping. *Journal of Micromechanics and Microengineering*, 14:170–81, 2004.

J. J. Neumann and K. J. Gabriel. *CMOS-MEMS Acoustic Devices*, pages 193–224. Wiley-VCH Verlag GmbH, 2008.

JJ Neumann and KJ Gabriel. CMOS-MEMS membrane for audio-frequency acoustic actuation. *Sensors and Actuators A: Physical*, 95:175–182, 2002.

Salvatore Nigro, Leonardo Pagnotta, and Maria F. Pantano. Analytical and numerical modeling of squeeze-film damping in perforated microstructures. *Microfluidics and Nanofluidics*, 12:971–979, 2011.

Rudra Pratap, Suhas Mohite, and Ashok K. Pandey. Squeeze film effects in MEMS devices. *Journal of the Indian Institute of science*, 87(1):75–94, 2007.

P. Rangsten, L. Smith, L. Rosengren, and B. Hök. Electrostatically excited diaphragm driven as a loudspeaker. *Sensors and Actuators*, A(52):211–215, 1996.

Jörg Rehder, Pirmin Rombach, and Ole Hansen. Balanced membrane micromachined loudspeaker for hearing instrument application. *Journal of Micromechanics and Microengineering*, 11:334–338, 2001.

K.K.F. Riley, M.P. Hobson, and S.S.J. Bence. *Mathematical Methods for Physics and Engineering*. Cambridge University Press, 2006.

Robert C. Roberts, Jiangang Du, Andojo Ongkodjojo Ong, Dachao Li, Christian A. Zorman, and Norman C. Tien. Electrostatically driven touch-mode poly-SiC microspeaker. In *Sensors, 2007 IEEE*, 2007.

P. Rombach, M. Müllenborn, U. Klein, and K. Rasmussen. The first low voltage, low noise differential silicon microphone, technology development and measurement results. *Sensors and Actuators A: Physical*, 95(2):196–201, 2002.

T.D. Rossing. *Springer book of Acoustics*. Springer, 2007.

M.H. Sadd. *Elasticity: Theory, Applications, and Numerics*. Elsevier Science, 2009.

P. R. Scheeper, W. Olthuis, and P. Bergveld. Fabrication of a subminiature silicon condenser microphone using the sacrificial layer technique. In *Solid-State Sensors and Actuators, 1991. Digest of Technical Papers, TRANSDUCERS'91., 1991 International Conference on*, page 408–411, 1991.

P. R. Scheeper, A. G. H. van der Donk, W. Olthuis, and P. Bergveld. Fabrication of silicon condenser microphones using single wafer technology. *Journal of Microelectromechanical Systems*, 1(3):147 – 154, 1992.

P.R. Scheeper, A.G.H. Donk van der, W. Olthuis, and P. Bergveld. A review of silicon microphones. *Sensors and Actuators A: Physical*, 44(1):1–11, 1994.

R. Schellin and G. Hess. A silicon subminiature microphone based on piezoresistive polysilicon strain gauges. *Sensors and Actuators A: Physical*, 32(1-3):555 – 559, 1992.

Adel S Sedra and Kenneth Carless Smith. *Microelectronic circuits*. Oxford University Press, 1987.

Joseph I. Seeger and Selden B. Crary. Stabilization of electrostatically actuated mechanical devices. In *Proceedings of the 1997 International Conference on Solid-State Sensors and Actuators*, 1997.

S.D. Senturia. *Microsystem Design*. Springer, 2000.

Iman Shahosseini, Elie Lefeuvre, Johan Moulin, Emile Martincic, Marion Woytasik, and Guy Lemarquand. Optimization and microfabrication of high performance silicon-based MEMS microspeaker. *IEEE Sensors Journal*, 13:273–284, 2013.

C. Shearwood, M. A. Harradine, T. S. Birch, and J. C. Stevens. Applications of polyimide membranes to MEMS technology. *Microelectronic engineering*, 30:547–550, 1996.

Z. Z. Shu, M. L. Ke, G. W. Chen, R. H. Horng, C. C. Chang, J. Y. Tsai, C. C. Lai, and J. L. Chen. Design and fabrication of condenser microphone using wafer transfer and micro-electroplating technique. In *Design, Test, Integration and Packaging of MEMS/MOEMS, 2008. MEMS/MOEMS 2008. Symposium on*, page 386–390, 2008.

P M Sousa, V Chu, and J P Conde. Reliability and stability of thin-film amorphous silicon mems resonators. *Journal of Micromechanics and Microengineering*, 22(6):065030, 2012.

S. Timoshenko. *Theory Of Elasticity 3E*. McGraw-Hill Education (India) Pvt Limited, 1951.

S. Timoshenko and S. Woinowsky-Krieger. *Theory of plates and shells*. McGraw-Hill, 1959.

E. Ventsel and T. Krauthammer. *Thin Plates and Shells: Theory: Analysis, and Applications*. Taylor & Francis, 2001.

Lin Xiao, Zhuo Chen, Chen Feng, Liang Liu, Zai-Qiao Bai, Yang Wang, Li Qian, Yuying Zhang, Qunqing Li, Kaili Jiang, and Shoushan Fan. Flexible, stretchable, transparent carbon nanotube thin film loudspeakers. *Nano Letters*, 8:4539–4545, 2008.

Zhao Yapu. Stiction and anti-stiction in mems and nems. *Acta Mechanica Sinica*, 19:1–10, 2003.

Seung Hwan Yi and Eun Sok Kim. Micromachined piezoelectric microspeaker. *Jpn. J. Appl. Phys.*, 44: 3836–3841, 2005.

Young D. Vibration of rectangular plates by the ritz method. *ASME J Appl Mech*, 17:448–453, 1950.